

210  
6-23-71

REV # 1176

# HTGR SAFETY EVALUATION DIVISION

QUARTERLY REPORT  
JULY - SEPTEMBER 1976

Date Published - March 1977

DEPARTMENT OF APPLIED SCIENCE  
BROOKHAVEN NATIONAL LABORATORY  
ASSOCIATED UNIVERSITIES, INC.  
UPTON, NEW YORK 11973

PREPARED FOR THE UNITED STATES NUCLEAR REGULATORY COMMISSION  
OFFICE OF NUCLEAR REGULATORY RESEARCH  
UNDER CONTRACT NO. EY-76-C-02-0016

MASTER

## **DISCLAIMER**

**This report was prepared as an account of work sponsored by an agency of the United States Government. Neither the United States Government nor any agency Thereof, nor any of their employees, makes any warranty, express or implied, or assumes any legal liability or responsibility for the accuracy, completeness, or usefulness of any information, apparatus, product, or process disclosed, or represents that its use would not infringe privately owned rights. Reference herein to any specific commercial product, process, or service by trade name, trademark, manufacturer, or otherwise does not necessarily constitute or imply its endorsement, recommendation, or favoring by the United States Government or any agency thereof. The views and opinions of authors expressed herein do not necessarily state or reflect those of the United States Government or any agency thereof.**

## **DISCLAIMER**

**Portions of this document may be illegible in electronic image products. Images are produced from the best available original document.**

# HTGR SAFETY EVALUATION DIVISION

QUARTERLY REPORT  
JULY - SEPTEMBER 1976

DONALD G. SCHWEITZER, Head  
HTGR Safety Evaluation Division

Manuscript Completed - February 1977  
Date Published - March 1977

The High Temperature Gas Cooled Reactor (HTGR) Safety Evaluation Division provides research and analytical support to the Nuclear Regulatory Commission (NRC), Office of Nuclear Regulatory Research (RSR), on all aspects of HTGR's regarding public safety. In addition to BNL personnel, the HTGR Safety Evaluation Division uses a wide national and international base of consulting expertise for RSR by close collaboration with consultants and subcontractors at universities and scientific establishments.

DEPARTMENT OF APPLIED SCIENCE  
BROOKHAVEN NATIONAL LABORATORY  
ASSOCIATED UNIVERSITIES, INC.  
UPTON, NEW YORK 11973

**NOTICE**  
This report was prepared as an account of work sponsored by the United States Government. Neither the United States nor the United States Energy Research and Development Administration, nor any of their employees, nor any of their contractors, subcontractors, or their employees, makes any warranty, express or implied, or assumes any legal liability or responsibility for the accuracy, completeness or usefulness of any information, apparatus, product or process disclosed, or represents that its use would not infringe privately owned rights.

PREPARED FOR THE UNITED STATES NUCLEAR REGULATORY COMMISSION  
OFFICE OF NUCLEAR REGULATORY RESEARCH  
UNDER CONTRACT NO. EY-76-C-02-0016

MASTER *EB*

DISTRIBUTION OF THIS DOCUMENT IS UNLIMITED



## NOTICE

This report was prepared as an account of work sponsored by the United States Government. Neither the United States nor the United States Nuclear Regulatory Commission, nor any of their employees, nor any of their contractors, subcontractors, or their employees, makes any warranty, express or implied, or assumes any legal liability or responsibility for the accuracy, completeness or usefulness of any information, apparatus, product or process disclosed, or represents that its use would not infringe privately owned rights.

Printed in the United States of America  
Available from  
National Technical Information Service  
U.S. Department of Commerce  
5285 Port Royal Road  
Springfield, VA 22161

Price: Printed Copy \$6.00; Microfiche \$3.00

April 1977

400 copies




TABLE OF CONTENTS

	<u>Page</u>
Summary	1
1. Task Area I - Fission Product Release and Transport	7
1.1 Adsorption of Metallic Fission Products (Brooklyn College)	7
1.2 The Permeability and Retentivity of Stressed Concrete Relative to Fission Product Iodine (North Carolina State University)	10
1.3 CsI Interaction with Materials (S. Nicolosi)	14
2. Task Area II - Primary Coolant Impurities	18
2.1 Helium Impurities Loop	18
2.1.1 Impurity Monitoring (S. Nicolosi)	18
2.2 Materials Test Loop (L.G. Epel, S. Nicolosi A. Romano)	19
2.2.1 Circulating Pump	20
2.2.2 Impurity Measuring System	23
2.2.3 Purification System	23
2.2.4 Impurity Injection System	27
2.2.5 Data Acquisition and Recording System	28
3. Task Area III - Rapid Graphite Oxidation	32
3.1 Analysis of Impurities in Graphite (J. Skalyo)	32
3.2 Catalytic Oxidation of Graphite (H. S. Isaacs)	36
3.3 Iron Species in Graphite (D. Chandra, J. Skalyo, Jr.)	55
3.4 Graphite Leaching (S. Nicolosi)	61
4. Task Area IV - Structural Evaluation (M. Reich, P. Bezler, B. Koplik, J. R. Curreri, T. Y. Chang, L. Lasker, H. Goradia, F. Kautz)	66
4.1 Core Seismic Response	66
5. Task Area V - Materials	76
5.1 Mechanical Properties of Materials (J. Chow, P. Soo)	76
5.1.1 Fatigue Testing of Incoloy-800H	78
5.2 Microstructure and Fracture of HTGR Graphite (The Aerospace Corporation)	90

TABLE OF CONTENTS - Cont'd.

	<u>Page</u>
5.3 Effect of Oxidation on Strength of Graphite	97
5.3.1 Effect of Impurities on Graphite Oxidation (A. Romano)	97
5.3.2 Mechanical Property Measurements (A. Romano, J. Chow)	106
5.3.3 Density Profile Measurements	110
5.3.4 Discussion	113
6. Task Area VI - Safety Instrumentation and Control Systems	117
6.1 Monitoring for the Impurities in the Primary Coolant at Fort St. Vrain (S. Nicolosi)	117
7. Task Area VII - Accident Delineation (C. Sastre)	118
8. Task Area VIII - Phenomena Modeling and System Analysis	119
8.1 HTGR Safety Code Library (J. Beerman, J. Colman)	119
8.2 Simplified Inventory of Radioactive Nuclides for Use in HTGR Calculations (J. M. Dickey)	120
8.3 Combustion Hazard Analysis (I. Omata, H. Takahashi)	132
8.4 STREC-3: A Digital Computer Model to Predict Fatigue Lifetime of Plates Subjected to Acoustic Noise (University of California, Santa Barbara)	136

## Summary

Several experiments on the release of cesium from H451 graphite in vacuo and in flowing helium have been completed. Reproducible release data were obtained for runs done in vacuo. In helium flow, loss of cesium during preheating at 500-600°C was inordinately great. The experimental system is, therefore, being revised so that all sample preheating will be performed in vacuo.

The second sorption experiment, for the adsorption of iodine by concrete has been completed. In this experiment the iodine partial pressure was  $3.14 \times 10^{-4}$  atm. Future experiments are planned at lower pressures.

The first permeability of iodine through concrete experiment has begun. The sample is a three inch cube with a three inch crack approximately one centimeter in depth.

As part of the investigation of cesium iodide interactions with materials, cesium iodide was heated with  $\text{Cr}_2\text{O}_3$ , a common surface oxide on stainless steels. The sample was heated to 700°C with no apparent reaction. Cesium iodide was also heated in air although reaction products may be attributable to impurities.

The HIL operation was discontinued during this quarter enabling modifications to be made in the loop instrumentation and also allowing construction to begin on the MTL.

The final design of the Materials Testing Loop (MTL) has been completed. All of the major components for the helium circulation, impurity



injection, and data acquisition and recording systems have been specified and ordered from various manufacturers. Construction of the loop began late in this reporting period, utilizing those hardware items that have been received from vendors to date.

X-ray emission spectroscopy utilizing an X-ray tube generator source and a Si(Li) detector is shown to be appropriate for determining impurities in graphite samples. The method is particularly advantageous when a non-destructive method is needed; thus samples can be characterized prior to their introduction into an experimental program. An analysis for impurity components with  $Z > 13$  is easily obtained.

Marked variations in composition with depth from the surface of a PGX graphite log have been found. The concentrations of iron increased from 16 to 1600 ppm with depth and gave a hundred fold increase in the rate of oxidation with saturated helium containing 8.5% hydrogen.

Iron impregnated graphites were oxidized in helium containing variable amounts of hydrogen and water. The oxygen activity of the gas was monitored with an oxygen activity meter. At oxygen activities where iron oxide would be present the oxidation rates at 700 and 750°C were below detection. When the oxygen activity was decreased and only metallic iron would be present the rate of oxidation increased. The rate of oxidation increased approximately with the square of the  $H_2/H_2O$  ratio or with the inverse of the oxygen activity to the fourth power.

A new Mossbauer spectrometer has been purchased and is undergoing tests. It is a diagnostic instrument that will aid in identifying the effect of iron and its compounds on graphite oxidation. Some of the compound species present in as received PGX graphite are being identified and catalogued. One observation is that the metallic-like iron peaks measured on PGX graphite samples are much broader than the widths of peaks measured on a metallic iron foil. The peak widths of iron and its compounds as measured on iron impregnated H451 graphite are nearly the same as found in the pure iron species.

Graphite leaching experiments have indicated that the impregnation of macroscopic graphite cubes, with a water solution, does not result in a sample entirely representative of that being imitated.

The Simear code was found to produce unacceptable results. An iterative version of the code was developed and tested. The version was found to function properly.

The studies of a cubic oscillator excited by multiple sine waves were continued. Results for the effect of damping and the magnitude of the cubic term on the critical lock-on ratio of the input wave amplitudes were developed.

New control consoles and activator units have been installed in three of the MTS fatigue units, and calibration has been completed. The data on Incoloy-800H for both low- and high-cycle testing have been used to develop a constitutive equation which will predict the

fatigue life as a function of strain range and temperature .  
Precipitation was shown to be an important factor in the fatigue strength of Incoloy-800H. Based on the cyclic work hardening data it was demonstrated that maximum precipitation strengthening was present at about 1100<sup>o</sup>F.

Polished specimens of ATJ, PGX and Stackpole 2020 graphite have been oxidized in flowing helium in the HIL loop. The exposure temperature was 1000<sup>o</sup>F and the moisture level was 1000 ppm. Scanning electron microscope evaluations indicate that there is no surface relief which can be attributed to oxidation for the levels of burn off achieved.

The Helium Impurities Loop (HIL) was used to expose several graphites to He containing nominal amounts of moisture and other impurities. The graphites exposed were H451, ATJ, 2020 and PGX. The types of specimens exposed were tensile, compression and metallographic. After up to 1974 hours of exposure to He containing ~100 ppmv H<sub>2</sub>O, PGX graphite continued to show high weight losses and a strong temperature dependence. The mean burnoff measured for PGX at 750<sup>o</sup>C was about 8%.

A number of the oxidized tensile specimens were tested. The results indicate an exponential relationship between loss of strength and burnoff similar to that in the literature for other graphites. A strong dependence on grain orientation of the PGX specimen tested was also observed.

The mass spectrometer which is planned for use at Fort St. Vrain is still under construction by the vendor.

Computer codes TAP (from General Atomic Corporation), MOSBDA, ORIGEN (from Radiation Shielding Information Center), and HAZARD, have been made operational and are now in the HTGR Code Library. The computer codes INREM and EXREM (from Radiation Shielding Information Center) are undergoing conversion to the CDC 7600.

Lists have been produced ranking in order of importance the radioactive by-products of an HTGR at times of one day and one week after a reactor scram. The differences in biological impact are taken into account by using dose commitment factors based on recommendations of the International Commission on Radiological Protection.

The code HTGRF4 which calculates the He gas layering in the containment vessel following depressurization of an HTGR was extended to the case of He, H<sub>2</sub>, and CO gas ingestion. The flammability in the containment gas was also studied. The report on this study and the manual for the new code HAZARD was written.

Based on the above studies, the estimation of the pressure rise due to energy release by the combustion was carried out by the simple calculation and it showed the good agreement with the value obtained from the experimental formula.

The computer code STREC-3 predicts the acoustic fatigue lifetime of plates subjected to a given acoustic noise spectrum. The choice

of three different models: the narrow band model, broad band model and quasistationary model; has been incorporated. The program has also the capability of predicting lifetime with different damping ratios for a single noise source or several noise sources in one run. The CPU time in IBM 360/70 is 66.35 secs for a sample run having three noise sources with four damping ratios for each source. In addition to the lifetimes, the output of the program includes the displacement spectrum, and the maximum stress spectrum. The natural frequencies and the damped frequencies are printed along with the variance of the stress spectrum at 1/50 of each of the octave bands used in the program.

1. Task Area I - Fission Product Release and Transport

1.1 Adsorption of Metallic Fission Products (S. Aronson,  
J. Mittelman, Brooklyn College)

Two experiments on the release of cesium from H451 graphite in vacuo were performed to check the reproducibility of data obtained on samples prepared in an identical manner. Samples of graphite were doped with  $\text{CsNO}_3$  and heated in stages to  $935^\circ\text{C}$ . The data obtained in these experiments are shown in Table 1-1 and Figure 1-1. Upon heating the samples, no loss of cesium occurred until the temperature rose above  $500^\circ\text{C}$ . After two hours at  $600^\circ\text{C}$  and an additional heating period of 20 minutes to raise the temperature from  $600^\circ\text{C}$  to  $740^\circ\text{C}$ , the samples had lost 13% and 27% of their cesium in Runs 1 and 2, respectively. The reason for this difference in cesium release is not apparent.

A measure of the reproducibility of the data can be obtained by comparing the two runs in terms of the fraction of the original cesium content lost in the same time period at each temperature. For this purpose, we have designated the initial cesium content at  $740^\circ\text{C}$  as the original cesium content. It is observed in Table 1-1 that the fractional losses on the samples are comparable at each temperature. We conclude that reasonably reproducible data can be obtained in vacuo.

Several runs were made in an atmosphere of flowing helium. Run 3 is shown in Figure 1-2. The initial cesium content was

Table 1-1

Data on Cesium Loss Rates in Vacuo

	Cesium Content $\mu\text{g Cs/g C}$	Initial Count Rate Counts/sec	Background Counts/sec	Fractional Loss		
				740°C	836°C	935°C
Run 1	153	85	6.5	0.26	0.31	0.11
Run 2	148	84	6.5	0.29	0.25	0.11

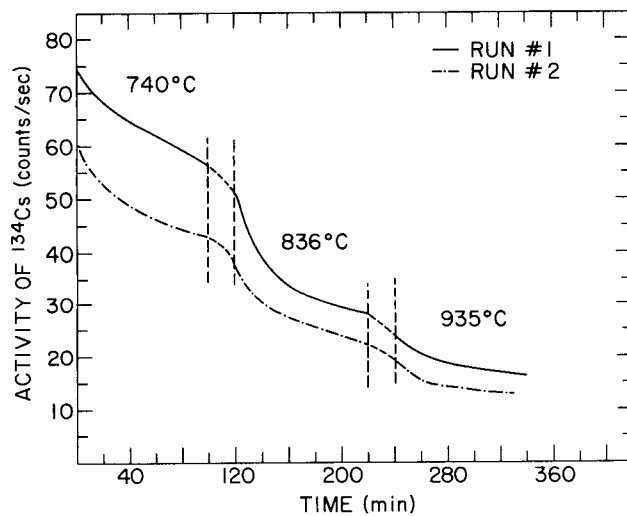


Figure 1-1.

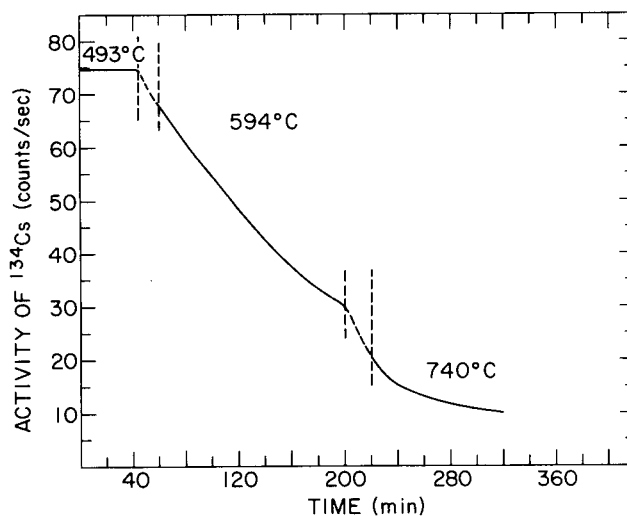


Figure 1-2.

140  $\mu\text{g}$  Cs/g C. The initial count-rate was 75 counts/sec with a background of 3 counts/sec. A flowrate of 40 cc (STP) per minute of a mixture of 1 mole percent hydrogen in helium was maintained throughout the experiment. No loss of cesium occurred below 500°C as in the case of the runs in vacuo. At 594°C, however, the loss of cesium was rapid and continuous. At the time the sample temperature reached 740°C, 75% of the cesium had been released. This behavior is quite different from the behavior in vacuo described above. In several additional runs made in helium, unmixed with hydrogen, the losses of cesium were comparably large.

An important aspect of our experimental program is a comparison of release data obtained in vacuo with release data obtained in a helium flow. This is important because most basic data on transport of metallic fission products through and from graphite have been obtained in vacuo whereas the reactor operates in a helium atmosphere. We are, therefore, revising our experimental system so that, whether cesium release is studied in vacuum or helium flow, preheating of the samples to temperatures above 700°C will be performed in vacuo under identical conditions.



1.2 The Permeability and Retentivity of Stressed Concrete Relative to Fission Product Iodine (L. R. Zumwalt, J. F. Mirza - North Carolina State University)

The second sorption experiment has been completed. Problems have developed with the control of the source temperature when the power was at a temperature (160.0°C) corresponding to  $P_{I_2} = 3.16 \times 10^{-5}$  atm. Saturation was approximately reached and the estimated concentration for saturation with  $P_{I_2} = 3.14 \times 10^{-4}$  atm and the sample at 25°C is  $C_{I_2} = 704 \mu\text{g } I_2/\text{g concrete}$ . In this case the ratio of saturation partial pressure ( $P_{I_2}$ ) to the partial pressure of iodine in equilibrium with solid elemental iodine ( $P_{I_2}^0$ ) is  $P/P^0 = .8$ . In the first run with  $P_{I_2} = 3.95 \times 10^{-5}$  atm at saturation,  $C_{I_2} = 489 \mu\text{g/g}$ . This corresponded to a  $P/P^0 = 0.1$ . These data show  $C_{I_2}$  not to be proportional to  $P_{I_2}$  and it is to be expected that the concrete at the higher  $P/P_0$  is approaching its capacity to hold iodine. We note, however, that this is a very large holding capacity when one compares the quantity of iodine isotopes that might be released in an accident, compared to the amount of concrete surface and mass in a prestressed concrete reactor pressure vessel or in a concrete reactor containment structure.

Our next objective is to obtain sorption data at lower pressure (i.e., at  $P_{I_2} < 4 \times 10^{-5}$  atm, where  $P/P_0 < 0.1$ ) which is pertinent to the low concentrations of iodine isotopes that will be encountered in possible accident conditions. However, the time

required to reach saturation will make it impractical to go to very low  $P_{I_2}$ .

Figure 1-3 (plot of  $C_{I_2}$  versus time) gives the initial kinetic behavior of the second sorption run. We note that the iodine concentration ( $\mu\text{g } I_2 \text{ sorbed/g concrete}$ ) increases linearly with time. Tentatively we interpret this to indicate the rate of sorption by interior surfaces and small pores is the rate limiting step rather than diffusion into the concrete via the larger inter-connecting pores which penetrate the concrete.

In the latter part of the second sorption run, the source vapor pressure was held at  $P_{I_2} = 3.96 \times 10^{-5} \text{ atm}$ . The flow of carrier gas (and iodine) was continued until no further desorption appeared to occur (i.e., until a plateau in the  $C_{I_2}$  versus  $t$  curve was reached). Then the temperature of the concrete sample was raised and a new equilibrium point (plateau) obtained.

The concentration of iodine in the concrete for different temperatures of the concrete are shown in Figure 1-4. As was reported earlier, temperature has only a small effect on the concentration. The concentration of iodine in concrete at  $25^\circ\text{C}$  was found to be  $170.2 \mu\text{g } I_2/\text{g concrete}$ . This is in good agreement with the earlier value obtained. The small effect of temperature may be related to the fact that there is a hysteresis effect. This effect has been observed by Mikhail and Selim.<sup>1</sup>

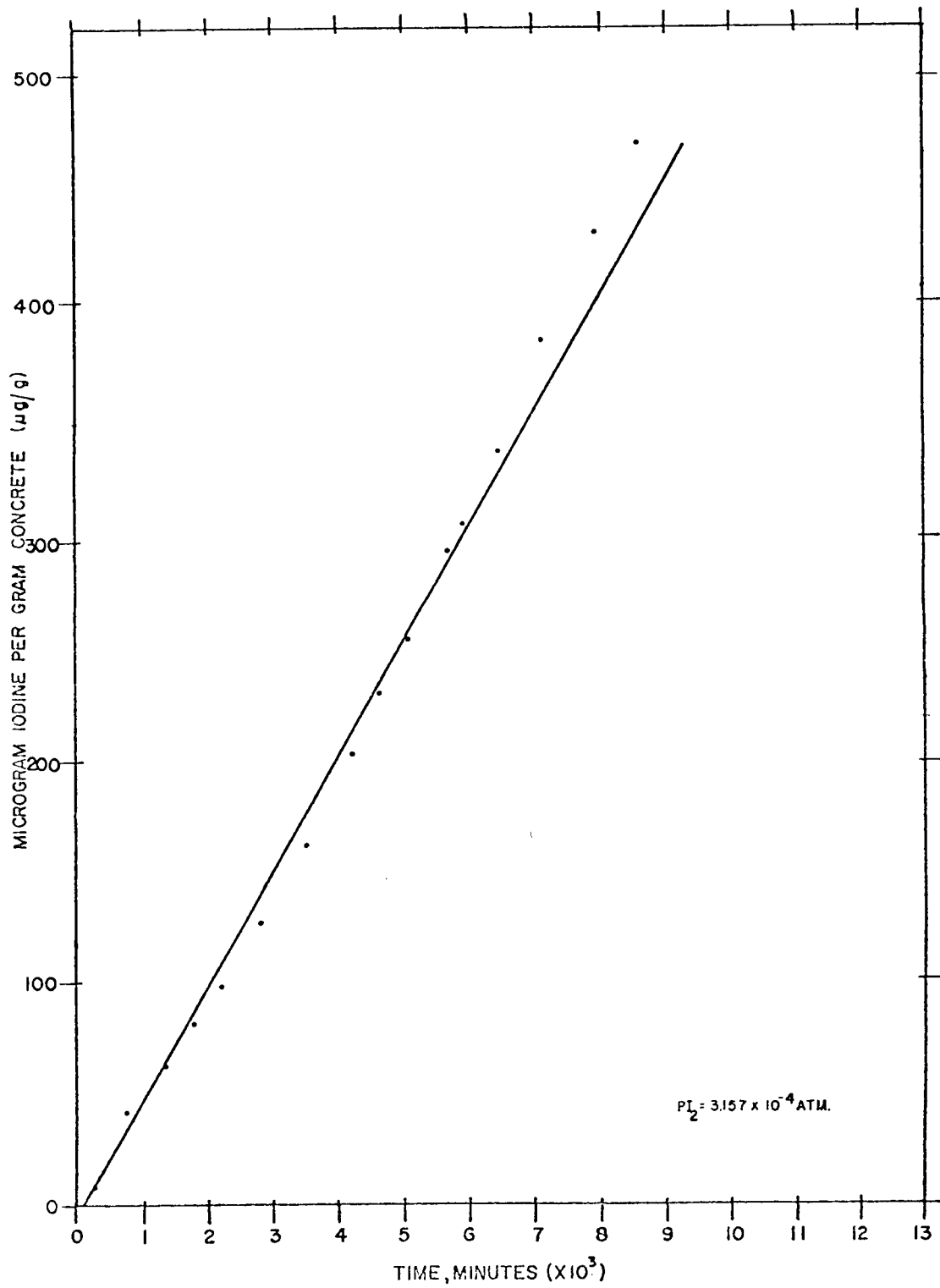


Figure 1-3. Plot of sorption of iodine by concrete at 25°C as a function of time.

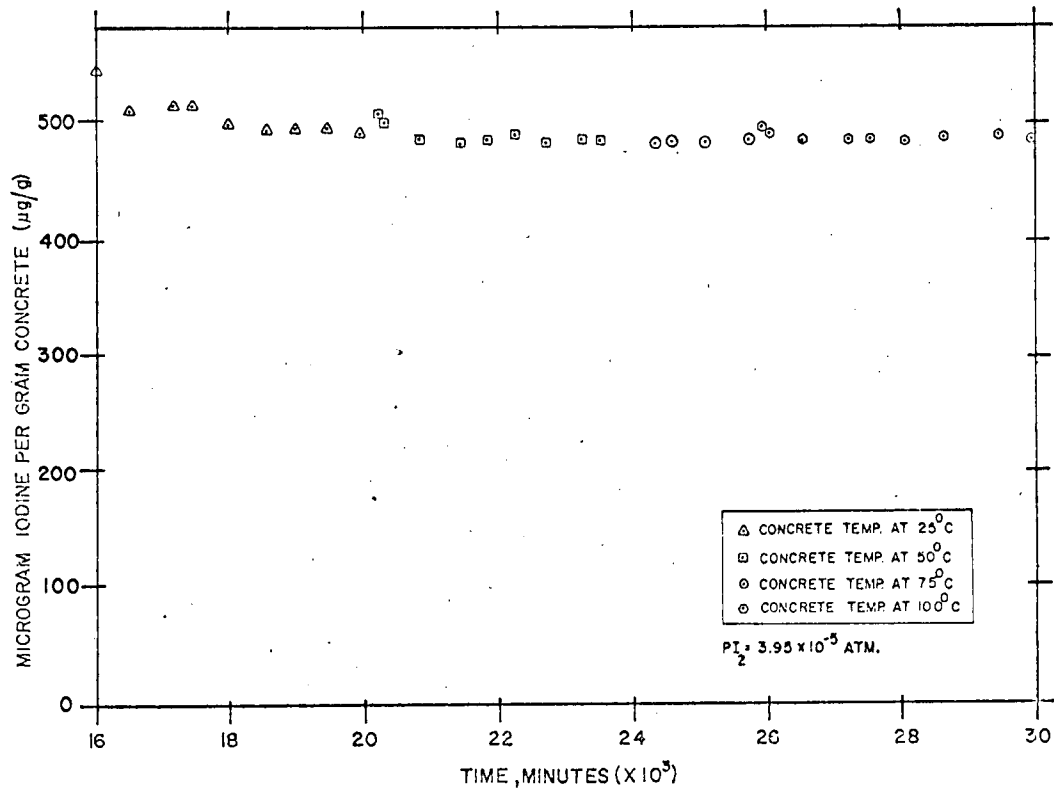


Figure 1-4. Concentration of iodine in concrete at different temperatures.

The first permeability experiment has begun, with a 3-inch cube that has a 3-inch long crack with a cracked region about one cm thick. The experiment is in a transient situation. The tagged iodine was detected in the charcoal trap on the down-stream side of the concrete within a few hours after start-up. A forced flow is induced by causing all helium (transporting the tagged iodine) to flow through the cracked concrete and then to charcoal trap. An added flow of helium is added to the down-stream side of the concrete sample to facilitate transport to the trap.

A preliminary study of permeability of the concrete with respect to helium and argon has been started. A system is being designed to vary the average pressure in the concrete so that we may obtain permeability as a function of average gas pressure. From preliminary data obtained for helium permeation with the concrete specimen at atmospheric pressure, the flow of helium through the 3-inch concrete specimen was found to be 5.31 ml/min over  $10^{-2}$  atm of pressure differential across the concrete. Plans are to continue these studies in the month of October, along with the above experiments.

### 1.3 CsI Interaction with Materials (S. Nicolosi)

When cesium and iodine vapor mix, stable cesium iodide is expected to form. Molecular beam experiments have indicated a large reaction cross-section ( $\sigma \gtrsim 100 \text{ \AA}^2$ )<sup>2</sup> indicating a reaction rate greater than the expected bimolecular collision rate based upon kinetic theory

using the mean sum of atomic diameters as the collision cross section. Such a high rate was implied experimentally by the work of D. Chandra.<sup>3</sup> Factors may be present which inhibit the formation of cesium iodide or which lead to the further reaction of cesium iodide. The purpose of this work is to investigate the release of cesium or iodine from cesium iodide as a result of chemical reactions that may occur during its migration. Interest is directed to cesium or iodine released in molecular or compound form with a significant mobility or volatility. Theoretical difficulties have been encountered due to the scarcity of relevant thermodynamic and experimental data. However, even for reactions that are thermodynamically promising, experimental investigation is necessary since the kinetics are not determined by the thermodynamic analysis. Although the thermodynamic driving force was not known, preliminary experiments were initiated on some CsI systems.

The reaction of CsI with  $\text{Cr}_2\text{O}_3$  was investigated since  $\text{Cr}_2\text{O}_3$  is a common surface oxide on stainless steels. A 66 weight percent mixture of CsI in  $\text{Cr}_2\text{O}_3$  was homogenized and compacted into a pellet under a pressure of  $\sim 2000$  psi. This pellet was heated in an evacuated quartz glass ampule ( $\sim 10''$  long) at a temperature of  $440^\circ\text{C}$  for two hours resulting in no visible change. The sample was then heated for approximately 10 hours at  $600^\circ\text{C}$  resulting in no visible change. Finally the system was heated for approximately 19 hours at  $700^\circ\text{C}$ . The CsI appeared to have distilled out of the pellet and

deposited on the cooler part of the ampule with no observable reaction. This experiment was repeated with a similar result.

CsI was heated in air in both open and closed systems. In the closed system experiment, CsI powder (~ .77 gms) was sealed with air in a quartz glass ampule. The sample was heated to 300°C for ~ 24 hours resulting in a yellow discoloration of the powder and small amounts of iodine crystals on the wall of the ampule and very small amounts of reddish-brown granules on the surface of the powder. The CsI was heated in air in open systems. Iodine was observed to be released (without apparent attack on the glass container), however, two different sources of CsI demonstrated different iodine releases. A preliminary x-ray diffraction analysis of each source indicated only the presence of CsI. The purity of the CsI is being investigated and the presence of higher iodides of cesium is suspected. Analysis is also continuing on reaction products.

References

1. Mikhail and Selim, "Adsorption of Organic Vapors in Relation to the Pore Structure of Hardened Portland Cement Pastes", Special Report 30, Publication 1389 (1966), Highway Research Board, NAS-NAE, Washington, D. C.
2. J.C.P. (1964) 41 1154.
3. HTGR Safety Evaluation Division: Quarterly Report: July - September 1976, to be published.



## 2. Task Area II - Primary Coolant Impurities

### 2.1 Helium Impurities Loop (S. Nicolosi)

Operation of the HIL has been discontinued due to the construction of the MTL and to the modifications that are being made in the HIL instrumentation. Some small design changes are also being considered.

#### 2.1.1 Impurity Monitoring (S. Nicolosi)

The Varian gas chromatograph, which has been used up until now in the HIL, is currently at the Varian factory undergoing modifications. These will result in the capability to perform automatic sampling of the MTL gas stream and analyze for H<sub>2</sub> exclusively. These modifications should be completed by November 1976.

It has been recognized that the H<sub>2</sub> concentration in a gas stream can be measured continuously by employing laser Raman spectroscopy. Such continuous monitoring of H<sub>2</sub> may be desirable in the loop kinetics experiments planned for the HIL or in other chemical kinetics experiments where the response time of the gas chromatograph is too slow.

An EG&G optical dew point analyzer for measuring the dew point of water in helium has been ordered. The instrument will be used for the calibration of the moisture monitors used in both the HIL and the MTL and elsewhere in the experimental program. It may also be used as a continuous on-line moisture monitor. The instrument should be capable of measuring dew points in the range of -73°C to +50°C and of operation in either the continuous or automatic balance mode.

2.2 Materials Test Loop (L.G. Epel, S. Nicolosi, A. Romano)

The design of the circulating helium loop, which will be dedicated to supplying hot helium containing specified amounts of gaseous impurities to mechanical testing machines, has been completed. All of the major components of the system have been specified and ordered, and construction at BNL has begun.

The design is such that the loop should be capable of operating for long time periods without the need to shut down for maintenance and operation of the loop should be as automatic as practicable. Thus, for example, there is a duplicate for every tank containing chemical reactant in the purification system so that as one tank becomes depleted the other can easily be switched on-line. All of the measuring instruments have been automated as much as possible and they all transmit data to a programmable data acquisition system.

The Materials Test Loop consists of five subsystems exclusive of the testing machines or the aging retorts to which it will be connected:

- . Gas Circulating System
- . Impurity Measuring System
- . Gas Purification System
- . Impurity Injection System
- . Data Acquisition & Recording System

A schematic drawing of the MTL is shown in Figure 2-1 which illustrates the first four of these subsystems. The figure also indicates that the helium will supply four separate banks, each bank consisting of retorts as follows:

- . 3 retorts for fatigue testing
- . 3 retorts for creep testing
- . 4 retorts for creep testing
- . 5 retorts for aging materials

The total number of retorts, for all purposes, is thus seen to be 15.

A description of the five major subsystems is given in this section.

#### 2.2.1 Circulating Pump

The helium circulating pump is a stainless steel bellows device driven by a  $\frac{1}{2}$  hp, 115/230 V, 3450 rpm, single phase induction motor and manufactured by the Metal Bellows Corporation. This special design, MB-602 HT, can operate in the vacuum mode or compressor mode and withstand temperatures up to 450<sup>o</sup>F. The helium will be in contact only with the stainless steel bellows and teflon gaskets thus assuring contaminant-free gas. The pump has two inlet and two outlet ports and hence can operate with the bellows in series or in parallel. Figure 2-2 gives the flow vs head characteristics of this pump for both modes of operation. In order to facilitate various flow rates as may be desired, parallel porting will be used.

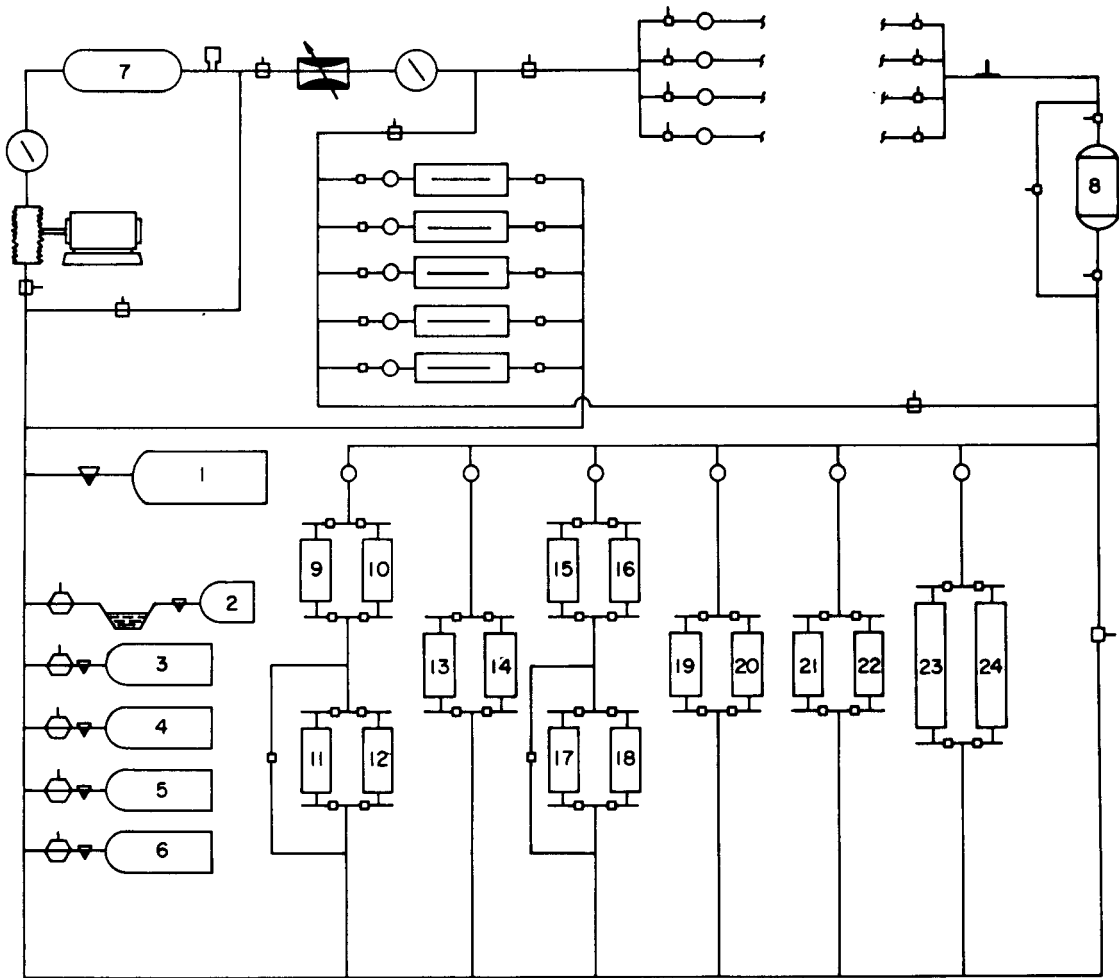


Figure 2-1.

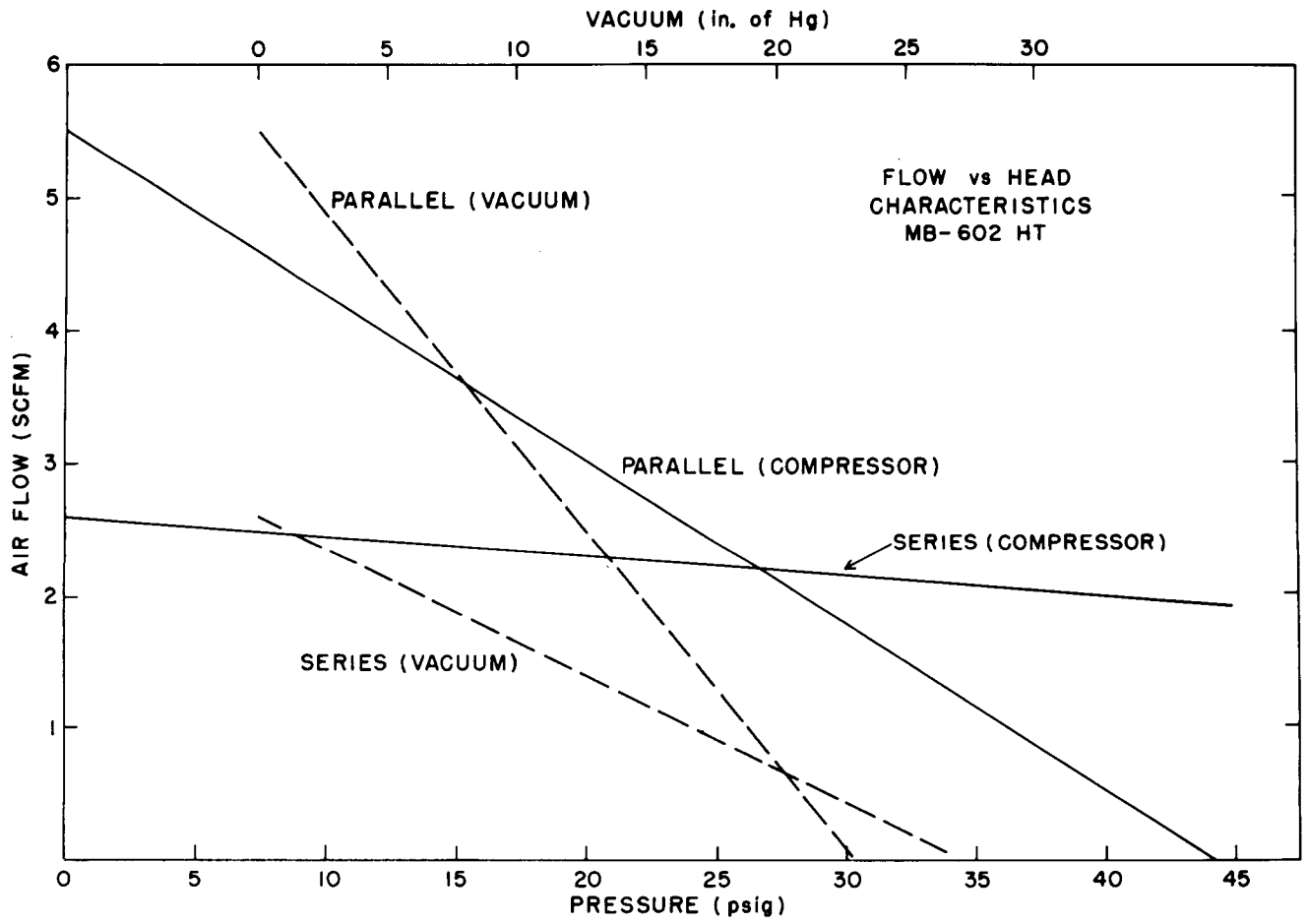


Figure 2-2. Flow vs head characteristics MB-602 HT.

### 2.2.2 Impurity Measuring System

The impurity measuring system will be capable of periodically determining the concentrations of  $H_2O$ ,  $H_2$ ,  $CO$ ,  $CO_2$ , and  $CH_4$ . The water vapor level in selected locations in the loop will be determined by a Panametrics moisture monitor employing an  $Al_2O_3$  type sensor. The sensor is a capacitor<sup>1</sup> with an  $Al_2O_3$  dielectric between a gold plate and an aluminum plate. As water is adsorbed by the dielectric the electrical capacitance of the probe changes. Since the amount of water adsorbed (at a given temperature) is dependent upon the water vapor partial pressure, the capacitance of the probe is related to the partial pressure of water in the gas stream.

The  $H_2$  concentration will be measured automatically by a Varian gas chromatograph which will sample the gas stream at set intervals and print a record of the  $H_2$  concentration.  $CO$ ,  $CO_2$ , and  $CH_4$  will be measured continuously by three separate Beckman Model 865 nondispersive infrared analyzers in which the attenuation of an infrared beam is determined by the number density of the absorbing sample species. The continuous output signal from the Panametrics hygrometer and the infrared analyzers will be recorded by a Doric Digitrend 220 data acquisition system (see section 2.2.5).

### 2.2.3 Purification System

As shown on Figure 2-1, the purification system consists of a total of 16 tanks distributed among 6 separate legs with appropriate valving to control the helium flow. All tanks and piping are constructed

of 304 stainless steel; valves are 316 stainless steel. The side-by-side arrangement of the tanks is simply to allow for continuous operation of the loop without the need to shut down for maintenance or recharging of the chemicals.

The design of the purification system is based on the desire to control each of the impurities in the helium stream on an individual basis without affecting the other impurities. This seems to be practicable except for methane removal. There is no simple method of removing methane without perturbing the concentrations of the other impurities. Table 2-1 indicates the maximum impurity levels desired in the MTL at one atmosphere (at higher pressures these values would be proportionately lower). It is clear from this table that  $\text{CO}_2$ ,  $\text{CH}_4$  and  $\text{H}_2\text{O}$  will be kept at relatively low concentrations while  $\text{CO}$  and  $\text{H}_2$  will generally be present in greater quantity.

Table 2-1  
Maximum Concentrations of Various Impurities in the MTL

Carbon Dioxide	20 ppmv
Carbon Monoxide	4500
Hydrogen	15000
Methane	500
Water Vapor	500

The left-most leg in the purification system shown in Figure 2-1 is devoted to controlling hydrogen. Tanks 9 and 10 contain

CuO at elevated temperatures (300 F and above) to oxidize the hydrogen. Tests have been conducted at BNL to ascertain how efficiently this reaction proceeds for various hydrogen concentrations, temperatures, and flow rates. A typical example is shown in Figure 2-3 which is for 52 ppm hydrogen in helium. The flow rate of 0.01 SCFH corresponds to a residence time in the CuO bed of approximately 150 seconds; the other flow rates correspond to proportionately shorter times. The S-shaped curves shown in Figure 2-3 are typical and indicate how the removal of impurities can be effected by temperature and/or flow control. Tanks 11 and 12 contain anhydrous magnesium perchlorate, sold commercially as Anhydrone, to remove the water generated in the CuO beds through the formation of hydrates.\* These two tanks can be bypassed if desired.

The adjacent leg, consisting of tanks 13 and 14, removes carbon dioxide. These two tanks contain sodium hydrate asbestos absorbent known commercially as Ascarite. The hydroxide removes CO<sub>2</sub> by forming sodium carbonate; conveniently this occurs at room temperature.

The next leg is dedicated to removing carbon monoxide. In a fashion similar to what occurs in the first leg, the impurity is oxidized over a CuO bed at temperatures of 300 F (or higher) in tanks 15 and 16. The resulting carbon dioxide is then removed with Ascarite in tanks 17 and 18. These two tanks can, of course, be bypassed when necessary.

\*Alternatively, molecular sieves, such as Linde molecular sieve 3A, could be used to remove the water vapor.



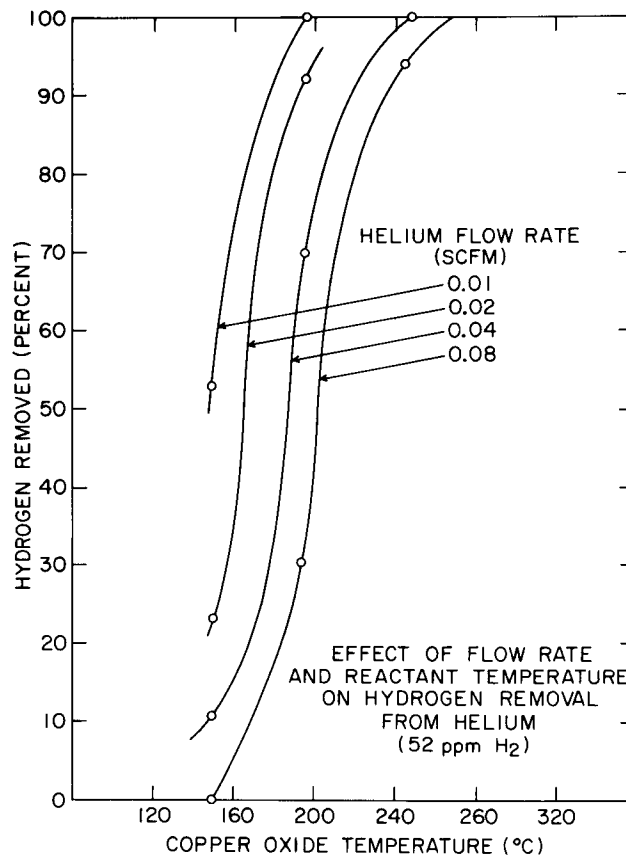


Figure 2-3. Effect of flow rate and reactant temperature on hydrogen removal from helium (52 ppm H<sub>2</sub>).



pressure reducing valve to a tube which is immersed in a temperature-controlled bath. The tube contains a mixture of 90 percent oxalic acid dihydrate and 10 percent anhydrous oxalic acid. The water vapor pressure over this mixture is sensitive to temperature as shown in Figure 2-4. Thus the amount of water injected into the MTL can be controlled very closely by adjusting the bath temperature.<sup>2</sup>

#### 2.2.5 Data Acquisition and Recording System

The heart of the data acquisition system is the Digitrend 220, manufactured by Doric Scientific. The present configuration allows for:

- . 100 individual data points
- . 4 alarm points per data point
- . hard copy output of all data points included in scans of data
- . automatic scanning of signals sequentially or randomly under external control.

The Digitrend will accept analog input signals for 100 separate channels such as thermocouples, current transmitters, pressure and/or flow transducers or other devices generating voltage signals. The voltage sensors have various ranges from 1 microvolt to 11 volts and can be autoranging, if desired. Cold junction compensation is built in for J, K, and S type thermocouples. For non-linear transducers, special programmable read only memories (PROM) were manufactured according to calibration curves supplied by BNL to the manufacturer. The

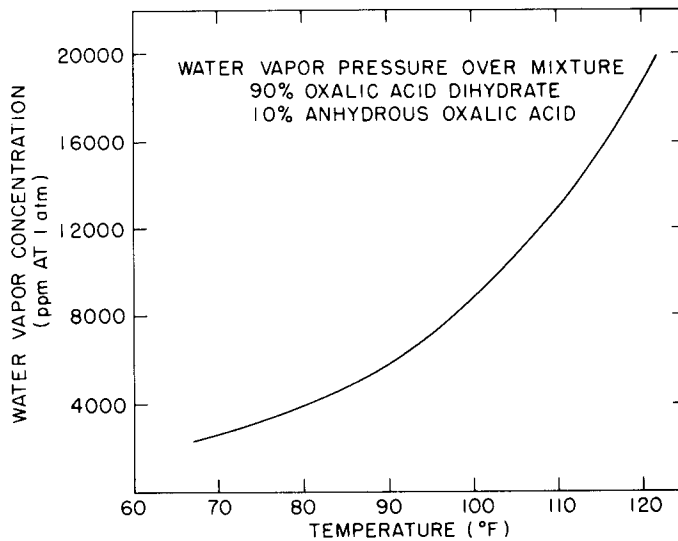


Figure 2-4. Water vapor pressure over mixture 90% oxalic acid dihydrate 10% anhydrous oxalic acid.

Digitrend digitizes all signals and logs them on printed paper tape, or optional computer compatible media such as magnetic tape, punched tape, modem, teleprinters, etc.

The data acquisition system offers good flexibility in the manner in which data is scanned and recorded automatically. Besides utilizing the front panel buttons and thumbwheels, the system can be programmed via the teletype terminal which enters instructions into the random access memory (RAM) directly. Among the choices that can be programmed are:

- . single scans of points or groups of points
- . timed scans, with intervals between scans anywhere between 1 second and 24 hours
- . continuous scanning
- . continuous scanning on alarm levels only
- . skipping points or groups of points
- . delaying alarms on points or groups of points for a specified number of scans.

Since the MTL is designed for long term operation, with little day to day maintenance or operator interfacing, a versatile and reliable data logging and alarm system is mandatory. The use of continuous-reading instrumentation throughout the loop, together with automatic data recording and an alarm system, should minimize the amount of loop-operator interaction.

References

1. Model 2000 Hygrometer: Operating and Service Manual,  
September, 1975, Panametrics, p. 34.
2. J. B. Bookey and N. C. Tombs, Oxalic Acid Dihydrate as a Source  
of Low Water-Vapour Partial Pressure, J. of the Iron and Steel  
Inst., September 1952, p. 86.

### 3. Task Area III - Rapid Graphite Oxidation

#### 3.1 Analysis of Impurities in Graphite (J. Skalyo, Jr.)

The application of X-ray emission spectroscopy<sup>1</sup> as a technique for measuring impurities in graphite has been investigated in a vendor-aided test. The method appears ideal since the test is non-destructive and the results can be obtained quickly with a minimum chance of misinterpretation.

In general, sample preparation in this analytical technique can involve diluting the sample in a low Z material; i.e., some mineralogical samples can be fused with a borate forming a sample glass bead.<sup>2</sup> The intensity of the observed characteristic X-ray line of an element is then almost linearly related to its concentration; the proportionality constant is Z dependent and highly variable. Sizable systematic errors in the observed intensities due to inter-element effects are not present since the characteristic X-ray coming from an element is due almost solely to its excitation by a source X-ray and not due to its excitation by a characteristic X-ray coming from an excited atom in the sample. The present problem is therefore one of an already suitably prepared sample wherein the impurity atoms are diluted in a graphite matrix.

Four different samples were analyzed with interest concentrating on impurities with  $Z < 40$ . The graphite types analyzed were H451, PGX, and two samples of ATJ. A first attempt was made to observe the spectra emitted when the sample was bombarded with a

$^{109}\text{Cd}$  radioactive source (emits 88 keV nuclear gamma ray and 22 keV Ag X-ray). The relative sensitivity of exciting impurity elements in the graphite is therefore a maximum for  $Z \approx 40$ . The observed signals were almost totally due to background except for the distinct observation in the PGX and the ATJ samples of sub ppm levels of strontium (14.1 keV). The H451 gave no discernable signal due to strontium. The low  $Z$  sensitivity could perhaps have been increased by using a  $^{55}\text{Fe}$  radioactive source but it is felt that useful results can only be obtained with a powerful X-ray tube source.

An X-ray tube source was used to analyze the samples with incident radiation coming from Ag (22keV), Ge (9.9 keV), and Ti (4.5 keV) secondary targets giving peak sensitivities for impurities near those elements. The results obtained with the Ag secondary gave information similar to that already obtained with the  $^{109}\text{Cd}$  source.

The results obtained with the Ge secondary radiation give the iron and calcium impurity content of the samples and are illustrated in Figure 3-1. This choice of secondary gives spectra which easily show the variability of these impurities ( $20 < Z < 26$ ) in the various graphite types. The variability of the observed Fe concentration in the two ATJ samples is typical.<sup>3</sup>

The very difficult low  $Z$  impurity content was observed with a Ti secondary. In the region  $Z < 20$ , the main difference appears in the K concentration. The results are shown in Figure 3-2. The Al



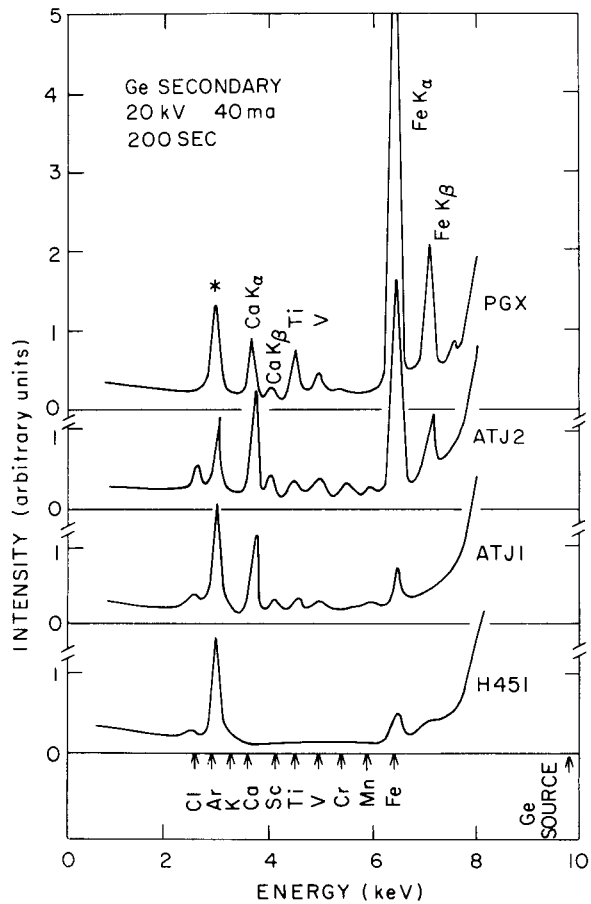


Fig. 3.1 Smoothed X-ray spectra observed with Ge secondary. The expected peak positions for the characteristic  $K_{\alpha}$  X-ray of various elements are shown at the bottom. The \* indicates a peak that is due to argon in the air contained in the test cell. The  $K_{\beta}$  peaks for Ca and Fe are also indicated ( $CaK_{\beta}$  is expected to be observed at  $\approx 10\%$  the level of the  $CaK_{\alpha}$  intensity; the former superimposes the Sc position).

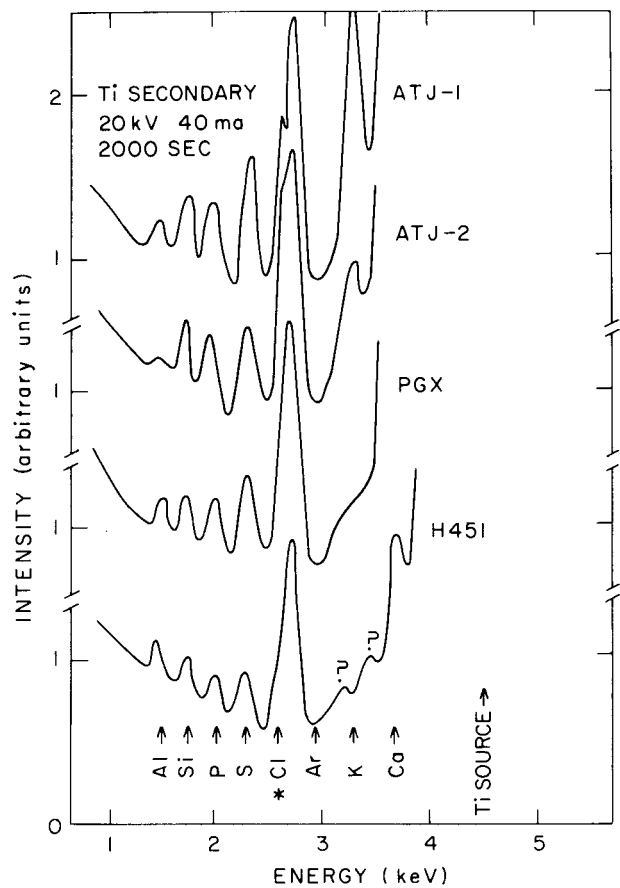


Fig. 3.2 Smoothed X-ray spectra observed with Ti secondary taken in an evacuated test cell. The expected peak positions for the characteristic  $K_{\alpha}$  X-ray of various elements are shown. The \* indicates the vicinity of the Cl peak obscured by a Ti escape peak. The two peaks observed in the H451 sample near the location for K were marginally visible and are not understood. K is observed in the ATJ samples and Ca is off scale in ATJ and PGX.

signal is weak and could be improved by better statistics.

The results of this survey indicate acceptable results on impurity content can be obtained non-destructively in graphite samples by X-ray emission spectroscopy. Difficulties of sample heterogeneity remain to be determined; however, a sample surface  $1-4 \text{ cm}^2$  can be illuminated by the incident X-ray beam in order to promote a measure of homogeneity in the results,

### 3.2 Catalytic Oxidation of Graphite (H. S. Isaacs)

#### (a) Effect of Impurity Distribution in PGX on its Oxidation Rate:

The oxidation characteristics of the PGX graphite was found to be highly variable and it appeared that the location from which samples were taken was a possible cause for the variations. The section of the log from which the samples were prepared was purchased by BNL from Union Carbide as representative of PGX graphite. It was 13cm thick and cut from the circular face of a cylindrical log, perpendicular to its axis.

A plate was taken from this section parallel to the axis of the log. It, in turn was cut into samples with adjacent pieces, equidistant from the face, being taken for oxidation and chemical analysis.

Oxidation of the specimens were conducted in the apparatus described in the previous Progress Report. The flow rate of the gas, saturated with water at room temperature was 2.5cc/sec.

All the samples were exposed to saturated helium with 8.5% hydrogen and two were again oxidized in saturated helium without hydrogen for periods of 20 hours at 750°C.

The results of the chemical analysis and the oxidation rates are shown in Figs. 3-3 and 3-4. The chemical analysis clearly shows marked variation in the level of impurities with position. The concentrations of iron and aluminum increase rapidly with depth by two orders of magnitude. Nickel and vanadium concentrations also increase with depth showing differences of about a factor of 5 from the surface down to 13cm. The calcium concentration was approximately constant at 200-300 ppm.

The marked changes in the oxidation rates of the graphite were observed as seen in Fig. 3-4, where the rate increased with distance from the surface by about two orders of magnitude when tested in saturated helium with 8.5% hydrogen. When tested in saturated helium without hydrogen, the rates were lower and indicated a less rapid change with distance. The decrease in rate when tested in saturated helium is in agreement with what has been observed with iron-doped H451 graphite. It can, therefore, be concluded that the change in the iron concentration is responsible for the major changes in oxidation rates with distance from the face of the log.

These results showed marked compositional change within the PGX and a relation between the purity and oxidation rates. This investigation should be followed with further compositional determina-

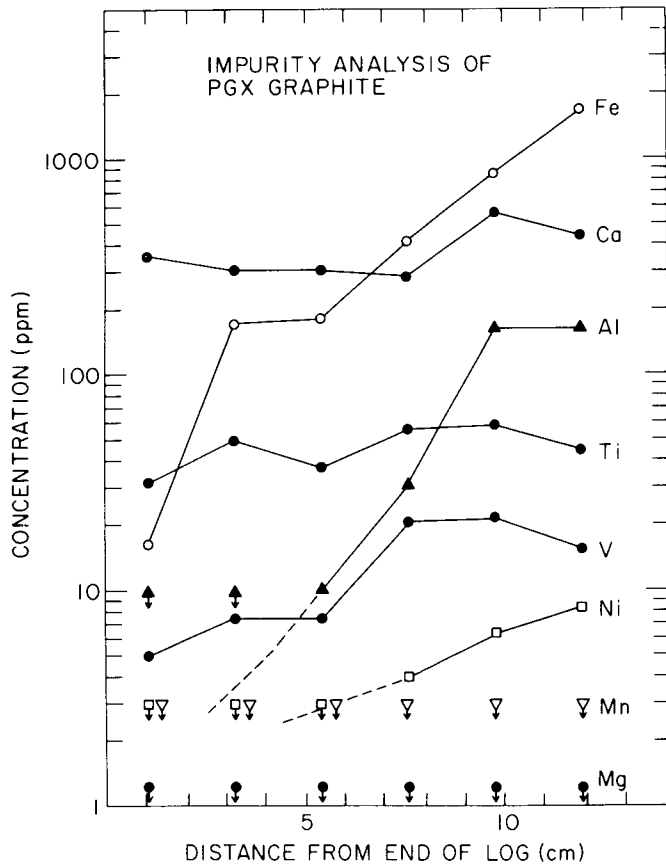


Figure 3-3. Variation of composition of PGX graphite with distance from the end of the log.

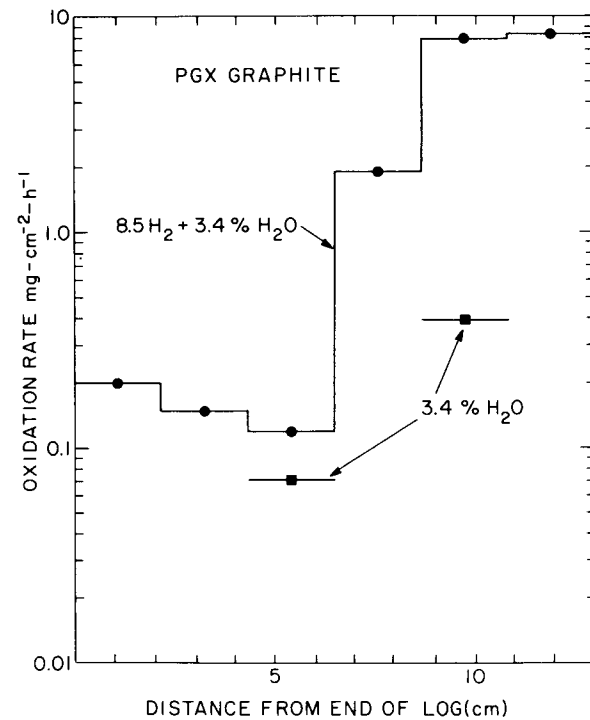


Figure 3-4. Variation in the rate of oxidation of PGX graphite with distance from the end of the log. Test carried out in saturated helium with and without 8.5% hydrogen.

tion at greater distances from the end of the log as the present results do not indicate any definitive leveling off of the iron concentration or the rates of oxidation.

(b) Oxidation Rates of Iron Containing Graphite as a Function of Oxygen Potential:

The rate of oxidation of graphite when pure, has been studied in sufficient detail so that the Langmuir-Hinshelwood, a general rate equation, can be used for calculations of graphite burn-off under a wide range of conditions and geometries.<sup>4</sup> When fission product impurities as for example strontium and barium oxide are present, the oxidation rates increase but the characteristics do not complicate the behavior and a similar rate equation can be used. With other impurities, notably iron, the oxidation characteristics can be complex and insufficient information was available for predicting oxidation rates of impure graphite over a range of exposure conditions. It appears from the literature that many factors influence the oxidation rates which include "minor experimental differences in temperature, pressure, catalyst concentration, catalyst state and distribution, etc."<sup>5</sup> and a more detailed investigation of these factors is required.

The distribution of oxidation in graphites, which are porous, will vary with depth. When high purity graphites are oxidized in helium with water impurities, the reaction products act as inhibitors and the reaction rate decreases with depth because of the

decrease in the reactant as well as the buildup of inhibiting products. When graphites contain iron impurities the behavior can be markedly different. It has been observed<sup>6</sup> that marked changes occurred in depth with an outer shell having undergone little or no reaction when exposed to CO<sub>2</sub>. A similar behavior could be expected with these impure graphites exposed to water. The differences in the burnoff with depth arises from the catalytic behavior of iron and its compounds. When iron is present in the metallic form it appears to act as an efficient catalyst, whereas the oxide is a poor catalyst. When the gaseous environment is sufficiently oxidizing to convert the iron to the oxide the iron near the surface will oxidize. In depth the reaction products build up decreasing the oxygen potential of the gas and leading to the reduction of any iron oxide. A marked increase in reaction product buildup decreases the oxygen potential of the gas and leads to the reduction of any iron oxide. A marked increase in reaction rate can then take place catalyzed by the metallic iron and resulting in a high burnoff in depth. At present, however, no data is available which relates the rate of oxidation for iron containing graphite to the oxygen potential of gas, that could be used for computation of graphite oxidation below the surface. The technique described here offers a possible method for determining this relationship.

### Apparatus and Sample Preparation

A schematic of the apparatus is shown in Figure 3-5. It consists of two compressed gas cylinders, one containing high purity helium or in one experiment 1% CO<sub>2</sub>, the other helium with 8.5% hydrogen. The gas lines leading from the cylinders were connected so that one or both gases could be used in two parallel lines. Each line led to a water-bubbler with a bypass and then to a flow meter. The gases were mixed after the flow meters, fed into the furnace and from the furnace to an electrochemical oxygen activity meter held at 650°C. A graphite specimen was suspended in the quartz tube furnace from a Cahn RH electrobalance. A two pen recorder was used to plot the potential from a Keithley 616 electrometer monitoring the voltage of the oxygen meter and the readout from the Cahn electronics which monitored the weight of the graphite.

The graphite specimens were 2 x 15 x 50mm in size. The H451 graphite was impregnated with an aqueous solution of Fe(NO<sub>3</sub>)<sub>3</sub>·9H<sub>2</sub>O containing 20% of salt by weight. The sample was held in a vacuum for 15 minutes, after which time the solution was added. When the specimen was completely immersed the system was brought to atmospheric pressure. The sample was left for an additional 15 minutes to allow the solution to penetrate the pores. The specimen was then wiped well with tissue paper and dried at 100°C prior to storage. The PGX graphite was taken from a position 13cm from the edge where the iron concentration was about 1600 ppm. During heatup of the



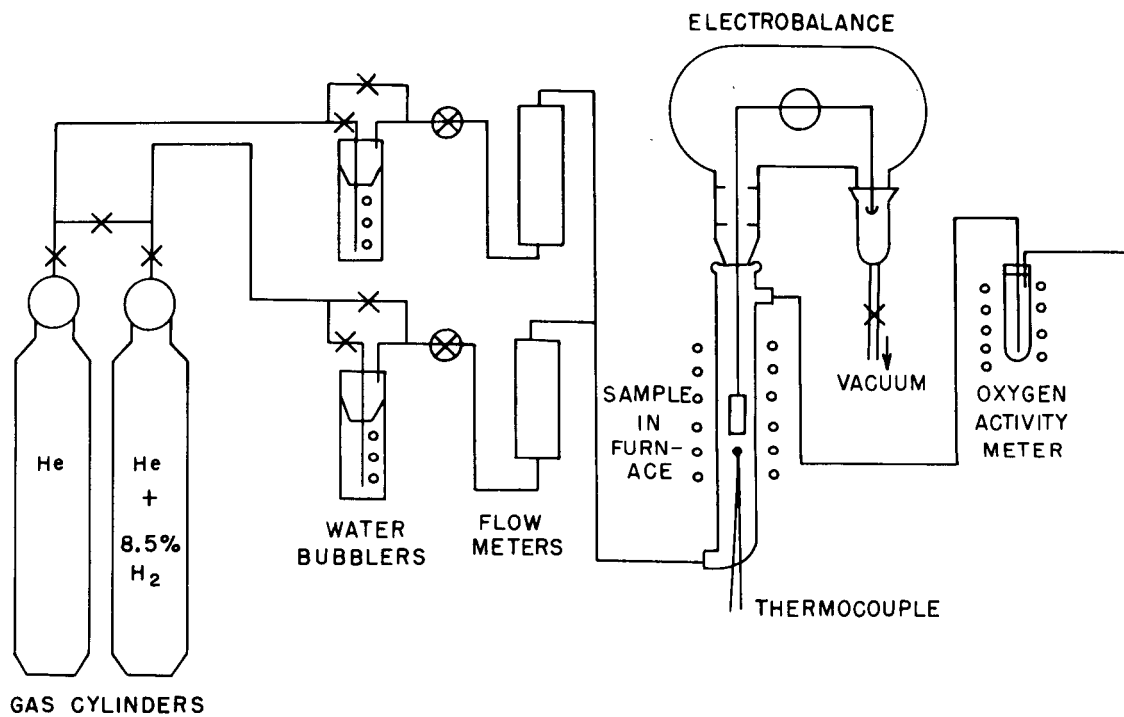


Figure 3-5. Schematic of apparatus for measuring oxidation of graphite and monitoring the oxygen activity of impure helium.

specimens to 700°C no account was taken of weight losses resulting from nitrate decomposition and off gassing of the graphite.

### Results

The chemical compounds of iron present during graphite oxidation will depend on the oxygen activity of the impurities in the helium. This activity depends on the ratio of the concentration of hydrogen to water ( $H_2/H_2O$ ) or carbon monoxide to carbon dioxide decreasing as their ratios are increased. The electrochemical oxygen activity meter relates the measured potential to these quantities.

Potential variations following changes in the  $H_2/H_2O$  ratio are shown in Figs. 3-6 to 3-9, for a series of tests where the oxidation of iron-impregnated graphite was studied. As can be seen from these results increasing the ratio of  $H_2/H_2O$  decreases the potential or it becomes more negative. In all cases the potential is, by convention, negative. Figs. 3-6 and 3-7 show the  $H_2/H_2O$  ratios adjacent to the potentials recorded during their addition to the helium. Once the gas composition was changed it took about 4 minutes for the measured potential to again reach a steady value. This response time was not related to changes in oxidation of graphite since it was observed when no graphite oxidation took place. The delay was a result of mixing of the gas present in the system prior to and after the change. The effect of graphite oxidation was to decrease the oxygen activity and the potential as water was consumed and

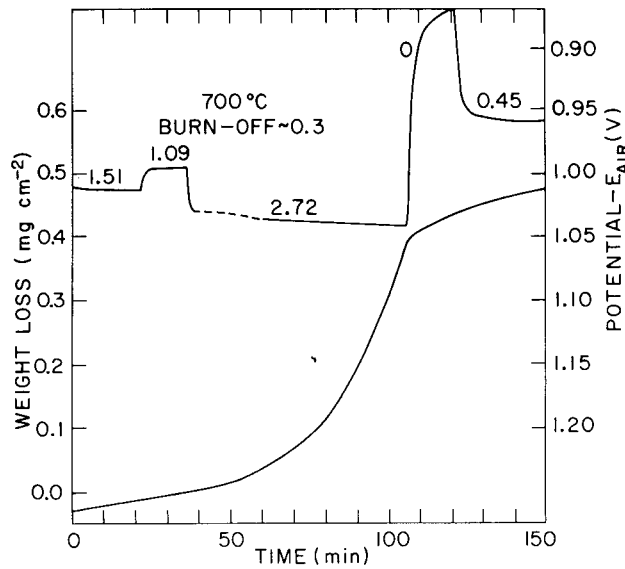


Figure 3-6. Influence of changes in the  $H_2/H_2O$  ratio on the potential and weight losses for an iron impregnated H451 graphite after  $\sim 0.3\%$  burnoff at  $700^\circ C$ . The ratio added to the cell is shown adjacent to the potential-time curve.

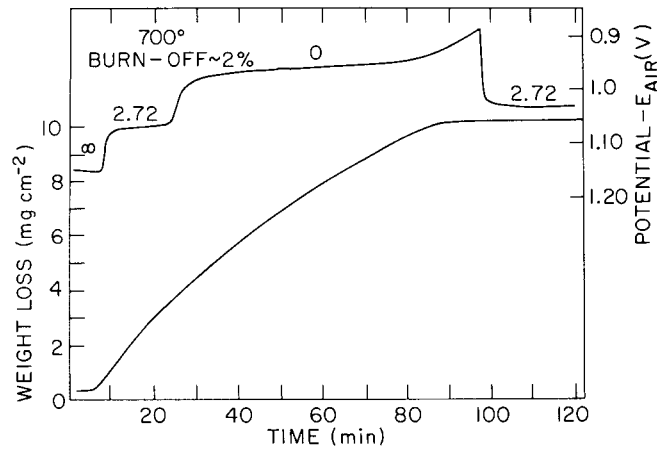


Figure 3-7. Influence of changes in the  $H_2/H_2O$  ratio on the potential and weight losses for an iron impregnated H451 graphite after  $\sim 2\%$  burnoff at  $700^\circ C$ . The ratios added to the cell are shown adjacent to the potential-time curve.

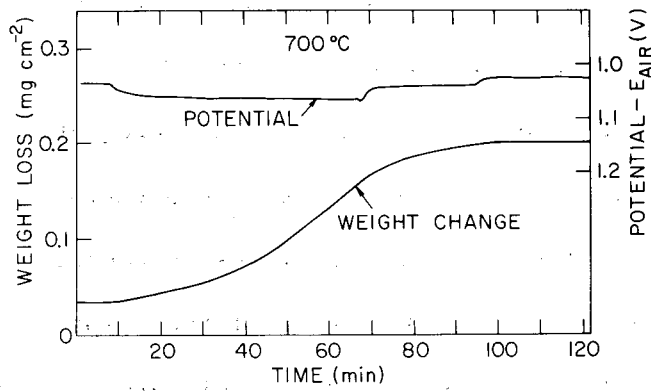


Figure 3-8. Variations in the potential and weight losses for an iron impregnated H451 graphite after ~15% burnoff at 700°C.

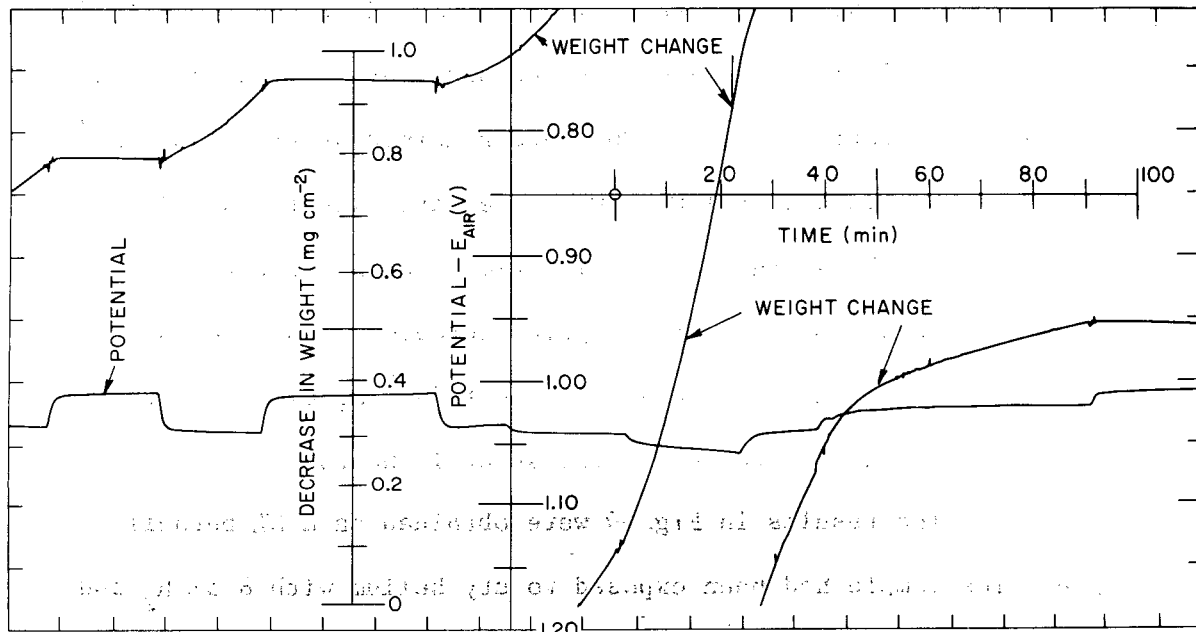


Figure 3-9. Variations in potential and weight losses for an iron impregnated graphite after ~15% burnoff at 750°C.

hydrogen and CO were produced. The response time for these changes were much greater and were related to changes in the rate of oxidation as may be seen in Figs. 3-6, 3-7, and 3-9.

The rate of oxidation of iron impregnated graphite was shown to depend on two variables: the  $H_2/H_2O$  ratio and the burnoff of the graphite. At low burnoff the rates responded slowly to changes in the  $H_2/H_2O$  ratio while at high burnoff the response was rapid. Examples of the slow response at low burnoff are in Figs. 6 and 7. Prior to the results in Fig.3-6 the sample with approximately 0.3% burnoff had been exposed to saturated helium (i.e. a  $H_2/H_2O$  ratio = 0) for 2 h. During this period the oxidation rate decreased from  $10^{-2}$  to  $8 \times 10^{-4}$   $mg\ cm^{-2}\ min$ . Fig.3-6 shows the behavior after hydrogen was added to give a ratio of 1.51. The rate remained at  $8 \times 10^{-4}$   $mg\ cm^{-2}\ min^{-1}$  at this ratio and at 1.09. When the ratio was further increased to 2.72 the rate began increasing with time. When the ratio was reduced to zero and 0.45 the rate again decreased. The decrease continued with time until a rate of below  $5 \times 10^{-5}$   $mg\ cm^{-2}\ min$  (the limit of detection) was reached after about 12 hours.

The results in Fig.3-7 were obtained on a 2% burnoff sample. The sample had been exposed to dry helium with 8.5%  $H_2$  and then saturated helium with  $H_2/H_2O$  ratios of 2.72, 0 and 2.72. When the saturated helium was added the rate was initially high but decreased with time to a value below detection after 65 minutes. This was a significantly shorter period than for the  $\sim 0.3\%$  burnoff sample

discussed above, which took about 12 hours. The period continued to decrease with increased burnoff. With high burnoff samples the period had decreased to the order of minutes. For example, in Fig. 3-8, where the small  $H_2/H_2O$  ratio changes are indicated by the potential changes, increased ratios gave significant decreases in rate of weight loss within minutes.

At  $750^{\circ}C$  the response with burnoff was essentially the same as those exposed at  $700^{\circ}C$ . At low burnoff the response period was of the order of hours and of the order of minutes after 15% burnoff as shown in Fig. 3-9. When the potential was increased the sample no longer lost weight. When the potential was again decreased as shown on the left of Fig. 3-9 the sample again oxidized and lost weight. The breaks in the weight change curve in Fig. 9 were a consequence of the necessity to rezero the recorder after it had spanned the chart and have no other significance.

The presence of a critical potential can readily be seen from the results in Fig. 3-9. When the potential was -1.01 volts negligible weight changes were observed at  $750^{\circ}C$  but whenever the potential was more negative than  $-1.019 \pm 0.001$  volts the specimen lost weight. The results in Fig. 3-8 reflect a similar dependence on a critical potential at  $700^{\circ}C$ . At this temperature the critical potential was found to be  $-1.037 \pm 0.002$  volt.

The rate of oxidation of the graphite increased rapidly with decreased potential or increased  $H_2/H_2O$  ratio at potentials

more negative than the critical potential. For example, near the middle of Fig. 3-9 the potential changed from about -1.04 to -1.05 and the rate increased by a factor of 2. The increased rates with increased  $H_2/H_2O$  ratio also lead to autocatalytic reactions where the graphite oxidation leads to an increased  $H_2/H_2O$  ratio, which, in turn, gave a higher oxidation rate. Experiments were run where the water concentration was decreased to increase the  $H_2/H_2O$  ratio. The same dependence on the ratio on the potential was found. The rate increased with decreased water concentration until it became mass transfer limited at which stage the rate of oxidation would decrease with decreased water concentration. The results obtained for the rate of oxidation as a function of potential are shown in Fig. 3-10. The results at the higher oxidation rates at  $700^\circ C$  were equal to those calculated for the rates of mass transfer of water through the apparatus under conditions of measurement and were obviously mass transfer limited.

Similar experiments were conducted on PGX graphite, at 700, 725 and  $750^\circ C$ . At  $700^\circ C$  the rates of oxidation were very low and were not studied in detail. At  $725^\circ$  and  $750^\circ C$  the rates were also found to increase with the  $H_2/H_2O$  ratio. A marked increase occurred between -1.012 and -1.035 at  $750^\circ C$ , but at the less negative potentials the rates remained relatively high. The rate changes and potential dependence were not clearly defined, even at high burnoff as was observed with the impregnated samples. When the potential

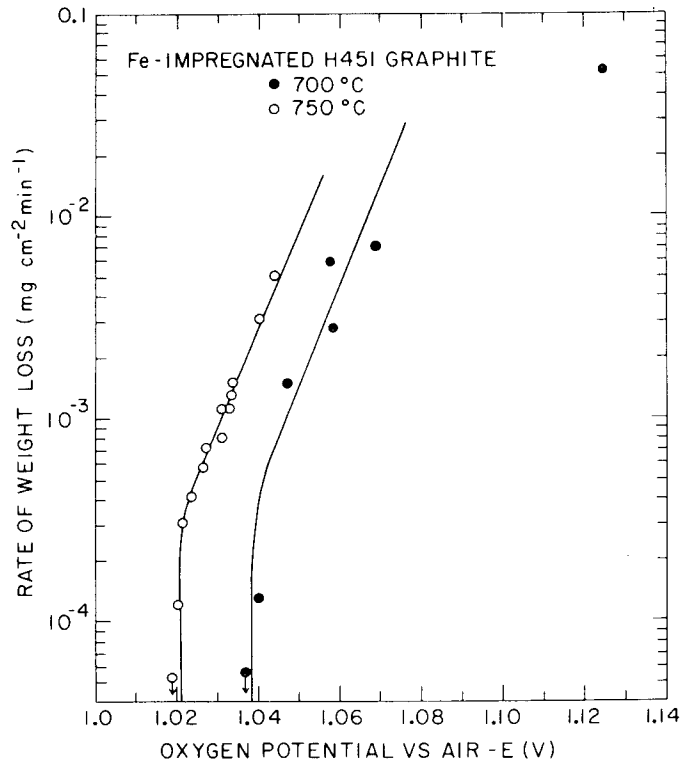


Figure 3-10. The rates of oxidation as a function of potential for iron impregnated graphite samples at 700° and 750°C.



was changed from more negative than -1.02 to less negative than -1.01 volts the weight of the sample increased by about 0.1 to 0.15 mg over a period of about 25 minutes. The magnitude of the weight gain would be approximately a tenth of the weight change expected if all the iron in the PGX graphite assumed as metal was oxidized to FeO. The weight gain then gave way to weight losses at a constant rate that did not decrease with time. This contrasted with the impregnated samples even at low burnoff which eventually showed no weight changes. A similar weight gain of much smaller magnitude was also observed with the impregnated graphite which contained about one fifth the amount of iron, but this gain was not followed by any weight loss.

The  $H_2/H_2O$  ratio (the oxygen activity or the potential, which are different ways of expressing changes in the oxidizing or reducing nature of the helium) has been found to be a major factor determining the oxidation rate of iron containing graphites. With high  $H_2/H_2O$  ratios the rate was always high. With lower ratios the rates were generally lower. In other words the rates of oxidation increased with increased hydrogen concentrations. This contrasts with the Langmuir-Henschelwood equation which predicts a decreased rate with increased hydrogen.<sup>4</sup> This equation has been found to apply to the oxidation rates of high purity graphite as well as graphites with various impurities not including iron nickel or cobalt.<sup>(4,6)</sup>

The oxidation rate of these graphites have been found to depend on many factors including temperature, burnoff, mass transfer of gaseous impurities, oxidant concentrations and graphite structure. 4-6

At low burnoff the rates of oxidation of the iron impregnated graphite changed with the  $H_2/H_2O$  ratio. This can be seen in Fig.3-6 where increased  $H_2/H_2O$  ratio led to a high oxidation rate and a decreased ratio reduced the rate. However the dependence was not well defined. In Fig.3-7 the same ratio of 2.72 gave markedly different rates. Extended periods of time were also required before the rates reached a steady state. For example at an 0.3% burnoff 12 hours was required for the oxidation to stop at  $700^\circ C$  while after 2% burnoff it took 70 minutes. At a high burnoff of 15% at  $700^\circ C$  it took only the order of minutes before the oxidation stopped as shown in Fig. 3-8. At  $750^\circ C$  the response was more rapid as shown in Fig.3-9 for high burnoff.

The effect of burnoff and prior exposure are due to the porosity of the graphite. Unoxidized or low burnoff graphites have fine pores which prevents rapid exchange between the gasses within the graphite and those flowing past it. The water entering the pores reacts with the graphite and leads to a more reducing environment. The reducing nature within the pores in turn leads to an increased rate but the rate of entry of oxidants into the graphite would also be hampered. In general it would be expected that the gases within

the graphite, but because of the predominant reducing environment the reaction rate would not be expected to stop except after a long period even at very low  $H_2/H_2O$  ratios.

With increasing burnoff and increased pore size the rates of exchange of gasses internal and external to the graphite would also increase. If any dependence on the composition of the gas added to the furnace did exist it would become more defined. Hence the results at the high burnoff would represent the kinetic dependence and be less influenced by mass transfer limitations and complications. Nevertheless, even at 15% burnoff mass transfer could become an important variable. With the high reaction rates the  $H_2/H_2O$  ratio would increase rapidly and in turn lead to a still higher rate of reaction because of limited gas mixing.

The results in Figs. 3-8 and 3-9 show that at high burnoff the rates of oxidation were sensitive to changes in the  $H_2/H_2O$  ratios or the potential. A critical potential was also obvious above which the oxidation stopped and below which it took place. As the potential decreased below this critical value the rates of oxidation increased. The change of the oxidation rate with potential is shown in Fig. 3-10. At the higher rates for both  $700^\circ$  and  $750^\circ C$  the rates increased exponentially with potential. These results are related to the reaction kinetics and were not controlled by mass transfer except for the largest value at  $700^\circ C$  discussed in the results section. These results, hence, show the dependence of reaction rate

on the potential which is, in turn, related to the oxygen activity ( $P_{O_2}$ ) or the  $H_2/H_2O$  ratio. These concentrations are related to the potential E by the Nernst equations

$$E = E_1 + \alpha \log (P_{O_2}) \quad \text{and}$$

$$E = E_2 - \beta \log (H_2/H_2O)$$

where  $E_n$ ,  $\alpha$  and  $\beta$  are constants. The results for the linear parts of the curves in Fig. 3-10 can be expressed as

$$E = E_3 - \gamma \log (R)$$

where  $E_3$  and  $\gamma$  are again constants and R is the rate of oxidation. For a given change in potential  $\Delta E$  for the three equations above

$$\Delta E = \log (P_{O_2}) = \beta \log (H_2/H_2O) = - \gamma \log (R)$$

or

$$R = (P_{O_2})^{-\alpha/\gamma} = (H_2/H_2O)^{\beta/\gamma}$$

The values of  $\alpha$  and  $\beta$  are respectively 98 and 49 mV. From Fig.3-10 the value of  $\gamma$  was found to be 22mV. These results indicate that the rate of graphite oxidation increases approximately with the square of the  $H_2/H_2O$  ratio or with the inverse of the oxygen activity to the fourth power.

The critical potentials at which the rate increased rapidly are close to those oxygen activities where Fe and FeO are in equilibrium. These potentials at which this equilibrium exist were calculated from

thermodynamic data but the limits of experimental error were  $\sim 2$  Kcal/g mole or 20mV. The results of  $750^{\circ}\text{C}$  for the critical potential in Fig. 3-10 were within limits of uncertainty the same potential at which iron and wustite ( $\text{FeO}_{1-x}$ ) were in equilibrium. The results of the critical potential at  $700^{\circ}\text{C}$ , however, could not unambiguously be equated with this equilibrium as the potential fell below that at which wustite would exist as derived from available thermodynamic data.

A probable explanation is given for the behavior of the oxidation rates around the critical potentials is related to the chemical composition of the iron. At potentials more positive than the critical potential, wustite is present which does not, within the limits of sensitivity of the techniques employed in this work, catalyze the oxidation of graphite as has been suggested for  $\text{CO}_2$  reactions with graphite.<sup>3</sup> At potentials where iron is stable the reaction of water with the graphite is catalysed and the rate increases with the square of the  $\text{H}_2/\text{H}_2\text{O}$  ratio. This rate decreases with decreasing  $\text{H}_2/\text{H}_2\text{O}$  ratio until the ratio is such that the iron oxidized to wustite. About this potential the reaction rate decreases rapidly to zero.

The behavior of the low burnoff iron-impregnated graphite is complicated by the presence of hydrogen which prevents the iron deep in the graphite from oxidizing and the graphite oxidation continues even though the environment passing over the graphite would

oxidize any available iron to wustite.

The results with PGX graphite even at high burnoff resemble those of the iron impregnated pure graphite at low burnoff. This behavior is a consequence of the presence of impurities other than iron which catalyze the reactions. The presence of about 400ppm calcium and lower concentrations of titanium (50ppm) and vanadium (20ppm) would catalyze the oxidation, independent of the catalytic effects of iron. Hence, at the low  $H_2/H_2O$  ratios these impurities gave rise to graphite oxidation and to an increased  $H_2/H_2O$  ratio. This tended to mask a clear-cut potential at which the rate increased or decreased markedly with these changes in the ratio. Nevertheless, a change in rate around those critical potentials observed with the iron-impregnated/H451 graphite did take place indicating that the role of iron in the PGX graphite was similar for the two graphites tested.

### 3.3 Iron Species in Graphite (D. Chandra and J. Skalyo, Jr.)

The sensitivity of determining iron in its compound form in graphite was greatly enhanced by the acquisition of a Mossbauer system with a  $67mCi$   $^{57}Co$  source. The instrument is undergoing acceptance tests and several graphite samples have been measured as a start towards determining a catalogue of relevant iron compounds encountered in graphite. Both PGX and iron impregnated H451 have been studied.

Large variation in the type and amount of iron species was found in various locations of as received PGX. Figure 3-11 shows 3 spectra which were obtained within  $1\frac{1}{2}$  inches of one another. For comparison, a spectrum obtained for an iron foil is also shown.

The peaks observed in PGX are broadened in comparison with those obtained from the iron foil. Since the lifetime of the nuclear energy level (which relates to the breadth of a peak) is negligibly affected by the chemical environment of the atom, such broadened peaks are due to the observation of an envelope of superposed peaks. The resulting distribution in the position of the  $^{57}\text{Fe}$  nuclear energy level is believed to be due to the different chemical, magnetic microenvironments of the Fe nuclei which are present in impurity clusters.

Line broadening due to resonance absorption in the source or in the absorber and instrumental broadening are not important (note the narrow line width of the iron foil). It is noted that locations 2 and 3 show no  $\text{Fe}_2\text{O}_3$ ; perhaps location 1 was originally near an exposed surface.

A program has been developed to fit Lorentzians to the spectral peaks. This provides a means of determining the amount of different iron species in the graphite. One of the spectra shown in Figure 3-11 is illustrated in Figure 3-12 with the analytical fit to the data. The spectrum shows no  $\text{Fe}_3\text{O}_4$  and has about 3 to 4 times more metallic iron than  $\text{Fe}_2\text{O}_3$ . The peaks are numbered and their specie

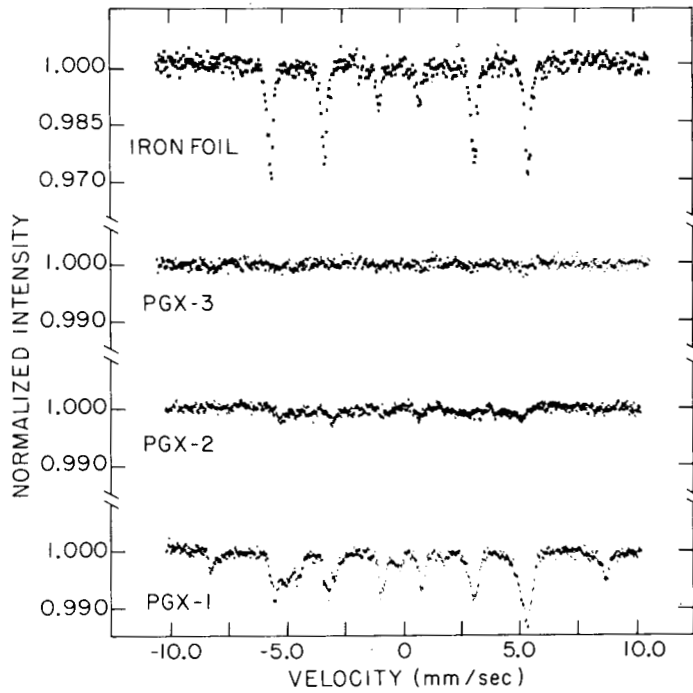


Figure 3-11. Mossbauer spectra of as received PGX. Samples were taken within 1½ inches of one another. Data at the top is of a standard iron foil.

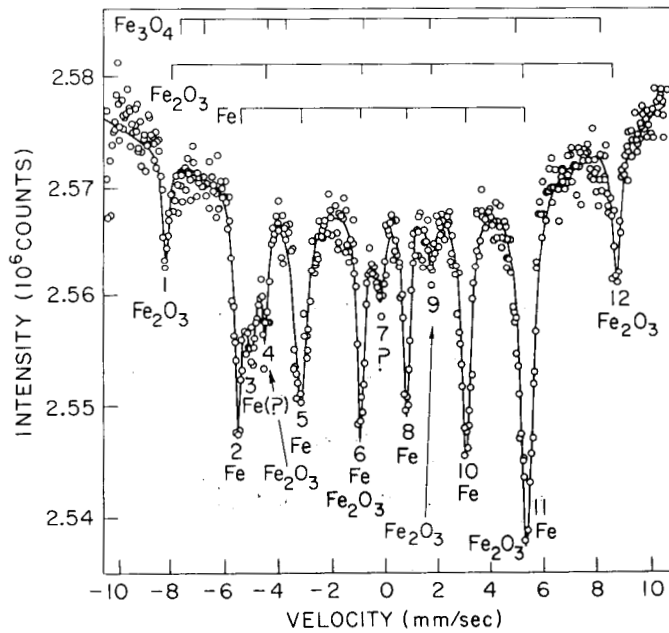


Figure 3-12. Detailed view and analysis of sample PGX-1 shown in Figure 3-11. Positions of  $\text{Fe}_3\text{O}_4$ ,  $\text{Fe}_2\text{O}_3$ , and Fe are shown at the top. No  $\text{Fe}_3\text{O}_4$  is found in this sample.



origin is also indicated. Table 3-1 gives the integrated intensity, full width at half maximum, and location of the peaks.

Peaks 2, 5, 8 and 10 are identified as due only to metallic iron; the remaining two metallic iron peaks occur too close to  $\text{Fe}_2\text{O}_3$  peaks to be resolved. The theoretical intensity relationship for the four clear peaks is in error and it appears that the intensity of peak 3 must be included with that of peak 2 to get satisfactory agreement. The significance of this split peak is not understood at this time; a difference with respect to the sharp peaks coming from the iron foil illustrated in Figure 3-11 is clear. The other peaks related to metallic iron are also due to the observation of an envelope of Lorentzians and their split character, evidenced by peaks 2 and 3, may not be observable with the present instrumental resolution.

Peaks 1 and 12 are due to  $\text{Fe}_2\text{O}_3$  and should have the same intensity. This disparity is believed due to a non linearity of the Mossbauer drive occurring at the most negative velocities. Future experiments have been done in the extended range  $-15\text{mm}/\text{sec} < V < +15\text{mm}/\text{sec}$  to alleviate this difficulty and to also provide a precise background baseline (necessary for determining the absolute impurity levels of the iron compounds).

Finally, peak 7 is an unknown iron species (perhaps austenite). It is a single line peak and, hence, due to a non-magnetic

TABLE 3-1

Peak Number	Integrated and Normalized Intensity ( $\times 10^{-3}$ )	FWHM (mm/sec)	Position (mm/sec)
1	$1.7 \pm 0.2$	$0.28 \pm 0.05$	$-8.24 \pm 0.02$
2	$3.7 \pm 0.5$	$0.32 \pm 0.04$	$-5.51 \pm 0.01$
3	$4.8 \pm 0.8$	$0.61 \pm 0.10$	$-5.01 \pm 0.02$
4	$1.4 \pm 0.5$	$0.23 \pm 0.08$	$-4.49 \pm 0.02$
5	$6.6 \pm 0.4$	$0.57 \pm 0.04$	$-3.16 \pm 0.01$
6	$4.1 \pm 0.3$	$0.32 \pm 0.03$	$-0.90 \pm 0.01$
7	$1.9 \pm 0.3$	$0.40 \pm 0.09$	$-0.18 \pm 0.03$
8	$3.4 \pm 0.3$	$0.29 \pm 0.03$	$+0.82 \pm 0.01$
9	$1.0 \pm 0.3$	$0.30 \pm 0.10$	$+1.75 \pm 0.03$
10	$6.5 \pm 0.3$	$0.45 \pm 0.03$	$+3.06 \pm 0.01$
11	$12.0 \pm 0.4$	$0.58 \pm 0.02$	$+5.31 \pm 0.01$
12	$3.2 \pm 0.3$	$0.41 \pm 0.05$	$+8.72 \pm 0.02$

iron compound. Several candidates for the origin of this line are expected and precise identification will depend on its significance in the oxidation of graphite.

The aforesaid measurements were done on as received PGX and are informative with respect to giving a baseline for further measurements which will be done after some oxidation experiment. It is noted that a previous large group of as received PGX samples showed evidence of containing only metallic iron, this group also evidenced iron peaks that were broader than that obtained with a metallic iron foil standard.

The impregnation of H451 with an iron compound and the reduction of the impregnant were followed step by step using Mossbauer spectroscopy. A characteristic two line spectra is obtained immediately following impregnation at room temperature. This agrees with the ferric nitrate spectra reported in the literature. This compound is reduced before the oxidation experiments were performed. In general, the application of Mossbauer spectroscopy confirmed directly the existence of pure metallic iron (in a few cases  $\text{Fe}_2\text{O}_3$ ) prior to oxidation treatments. Unlike the species observed in PGX, no complex very broad envelopes or unidentifiable peaks were observed.

Following oxidation, the spectra corresponded almost exactly to either metallic iron or  $\text{Fe}_3\text{O}_4$  depending on the oxidation potential of the gas mixture emerging from the reaction chamber. The spectra obtained are consistent with those discussed in the previous

Quarterly Report.<sup>3</sup> Figure 3-13 shows a sample spectrum obtained from an impregnated H451 sample oxidized in water saturated helium without hydrogen. A spectrum obtained from a standard  $\text{Fe}_3\text{O}_4$  sample is also shown in this figure for comparison. The spectra are virtually identical to each other.

It is observed that both impregnated H451 and as received PGX contain iron in finite sized clusters since the spectra give magnetically split peaks. The broadened peaks observed in PGX indicate a more heterogeneous environment for the iron than is found in impregnated H451; whether this environmental difference affects the catalytic behavior of the iron in the two graphites is not immediately evident.

#### 3.4 Graphite Leaching (S. Nicolosi)

PGX graphite was leached with a 1:1 mixture of  $\text{HCl}:\text{HNO}_3$ . The leaching procedure entailed the evacuation of the sample prior to the first acid leach. For each leach, 25 ml of the concentrated acid solution was added and every four hours the solution was changed. The results, shown in Figure 3-14 are not significantly different from those obtained previously from a procedure in which the sample was not preevacuated. To compliment this work a sample of H-451 was impregnated with a  $9 \times 10^{-4}$  molar solution of  $\text{Fe}(\text{NO}_3)_3$  using the method previously employed in the Brookhaven graphite oxidation program. This sample was then leached in the same manner as that previously

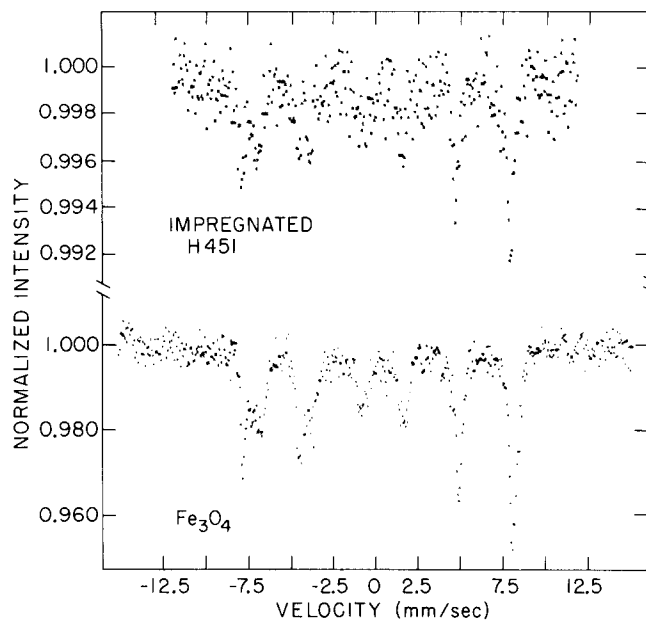


Figure 3-13. Mössbauer spectra of iron impregnated into H451 after conversion to Fe<sub>3</sub>O<sub>4</sub>. An Fe<sub>3</sub>O<sub>4</sub> standard is shown at the bottom.

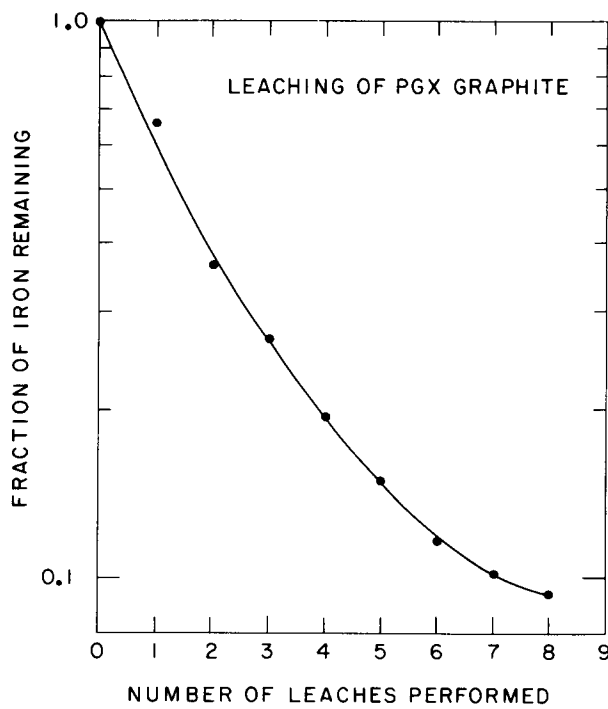


Figure 3-14. Leaching of PGX graphite.

described for the PGX sample shown in Figure 3-14. The leaching results of the impregnated H-451 are shown in Figure 3-15.

Comparison of the results of the leached PGX and the impregnated H-451 indicates that the impregnation process artificially creates an impure sample of graphite with an impurity distribution that is more accessible than the impurity distribution in the graphite that is being imitated. Thus, the impregnation process is to be considered as another variable in the graphite oxidation program.

PGX graphite was also leached with pyridine hydrogen chloride. However, the results were inconclusive due to an unusually pure sample of PGX.

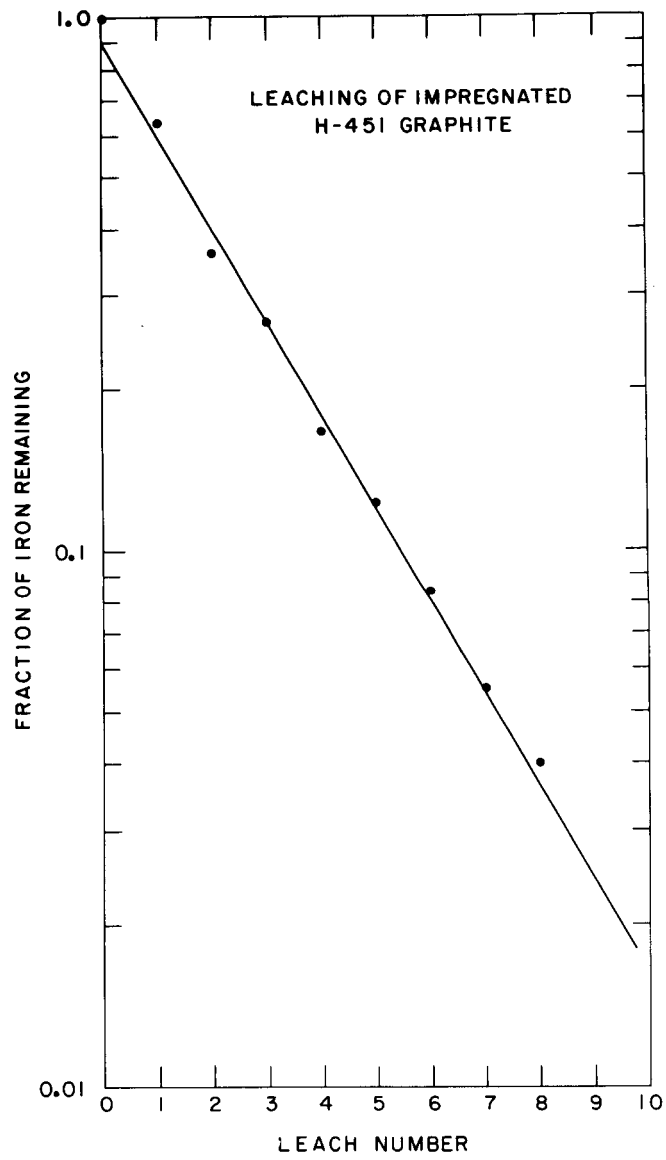


Figure 3-15. Leaching of impregnated H-451 graphite.

## References

1. R. Woldseth, X-ray Energy Spectrometry, Kevex Corporation, Burlingame, California (1973).
2. W. K. deJongh, Norelco Reporter, 23, 32 (1976).
3. HTGR Safety Evaluation Division Quarterly Report, April-June 1976, BNL-NUREG-50599.
4. Ref. OXIDE 3.
5. M. R. Everett, D. V. Kinsey and E. Romberg, "Carbon Transport Studies for Helium Cooled High-Temperature Nuclear Reactors" Chemistry and Physics of Carbon Ed P. L. Walker Jr., Vol. 3 1968, p. 289.
6. P. L. Walker Jr., M. Shelf and R. A. Anderson "Catalysis of Carbon Gasification", *ibid* Vol. 4, 1968, p.



4. Task Area IV - Structural Evaluation (M. Reich, P. Bezler, B. Koplik, J. R. Curreri, T. Y. Chang, L. Lasker, H. Goradia, F. Kautz)

4.1 Core Seismic Response

It was reported in the last quarterly that a number of available seismic computer codes were received and implemented on the BNL system. Of these the SIMEAR code, designed to generate a stimulated earthquake with prescribed spectral properties, was found to produce unacceptable results. Specifically, the code is supposed to produce an earthquake time history with spectra characteristics that match and/or envelope the spectra input to the code. It was found that the spectra for the generated time histories only crudely matched the input spectra and infact did not necessarily envelope that spectra over the whole frequency range. As this code is of prime importance in the seismic investigations contemplated, a corrected version of it was developed.

SIMEAR in its original form employed the concept of random phase angles to generate the simulated earthquake. This procedure is adequate and in accord with the recommendations by Scanlon.<sup>1</sup> The failing in the original code was that the coefficients developed after one iteration of this procedure were accepted as adequate. The spectra of the generated time history was neither computed nor compared to the input spectra. In the revised version the procedure is applied iteratively. With each iteration the spectra are computed, compared to the input spectra and suitable corrections made to the developed coefficients. When the developed spectra closely match the input spectra, the generated time history is accepted.

An example of this procedure is depicted in Figures 4-1 - 4-3. Figure 4-1 shows the input "target" acceleration spectra. It is desired to develop a time history which has the spectral properties depicted in this figure. With one iteration of the SIMEAR code, i.e., the original format, the pseudo relative velocity spectra delineated by the numeral 1 on Figure 4-2 is produced. On this computer generated figure the \* symbol delineates the target pseudo relative velocity spectra. As can be seen, there is a great mismatch with the generated spectra (1) falling below the target spectra (\*) over a large range of periods. In Figure 4-3 the two spectra coincide, only the target spectra symbol is shown. As can be seen, the match is very good except in the range of high periods (low frequency range). The mismatch in this region is of no significance since the frequencies are below the seismic range.

The development of the multi-column vertical array computer code is near completion. The code is designed to predict the response of a multi-column array of blocks when subjected to the simultaneous action of horizontal and vertical forcing functions. Each block element has the three degrees of freedom associated with motions in a plane; horizontal, vertical and rotational. Non-linear gaped springs, Coulomb-friction and viscous damping between elements, and dowel pin interaction effects are included.

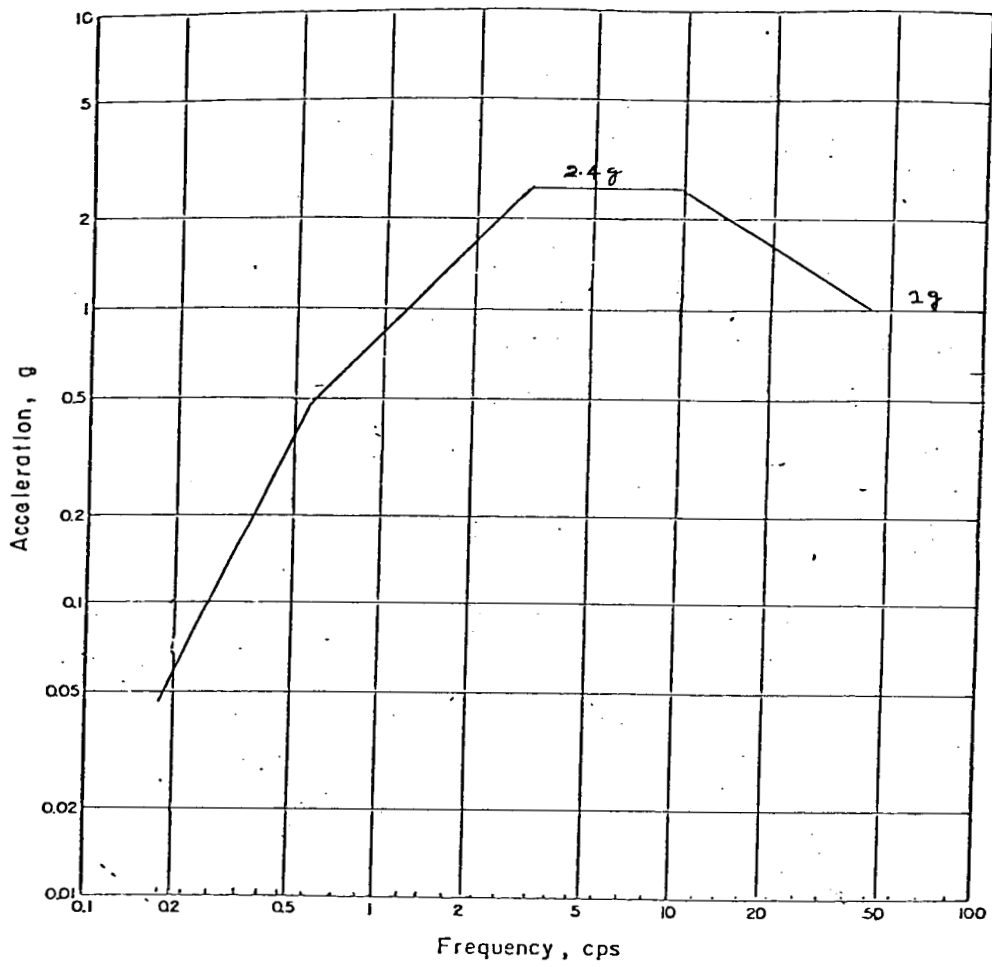


Figure 4-1. Recommended "design" spectra, 7% damping.

TIME HISTORY FOR ISET=991

PSEUDO-RELATIVE VELOCITY (FT/SEC)

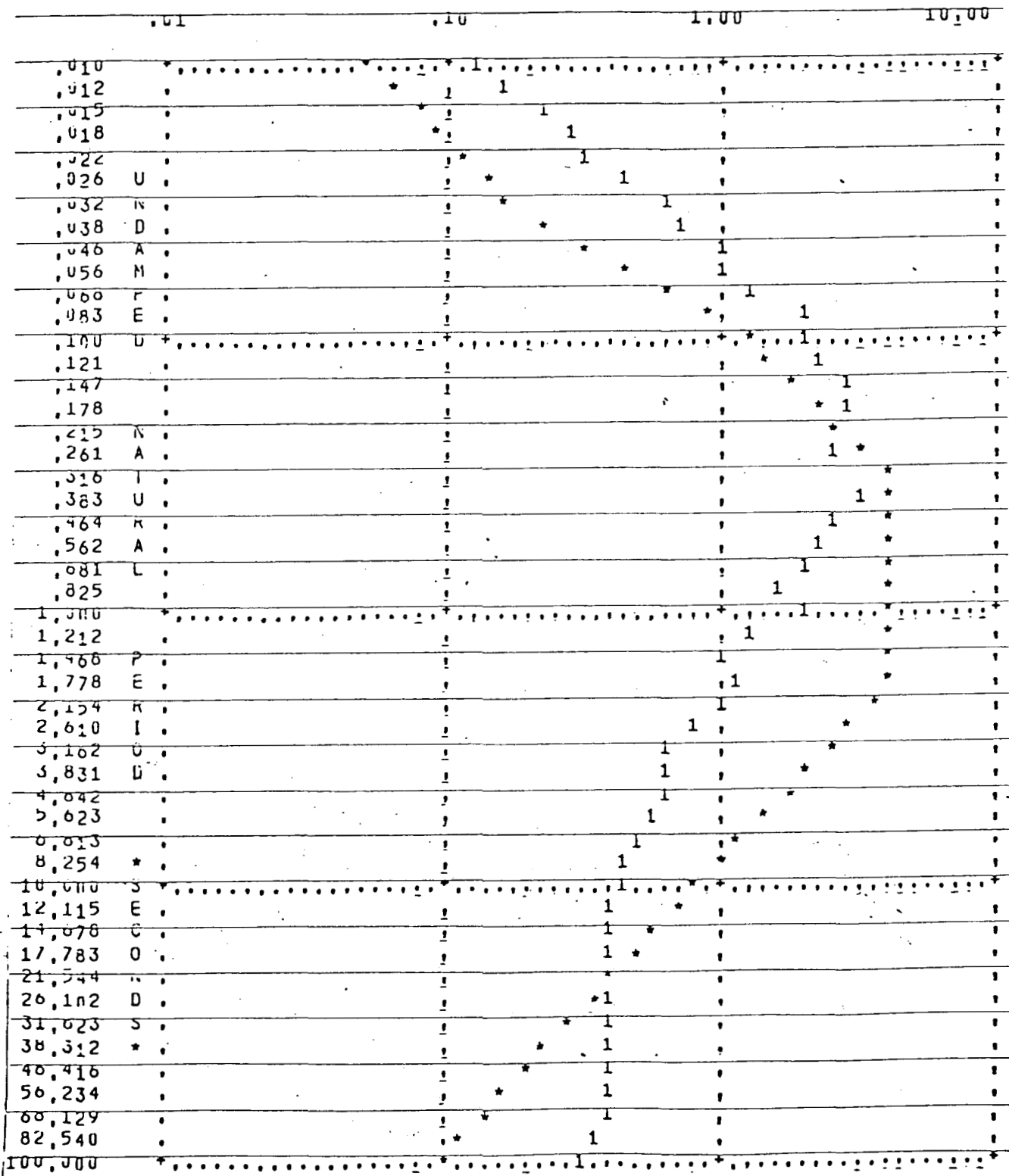
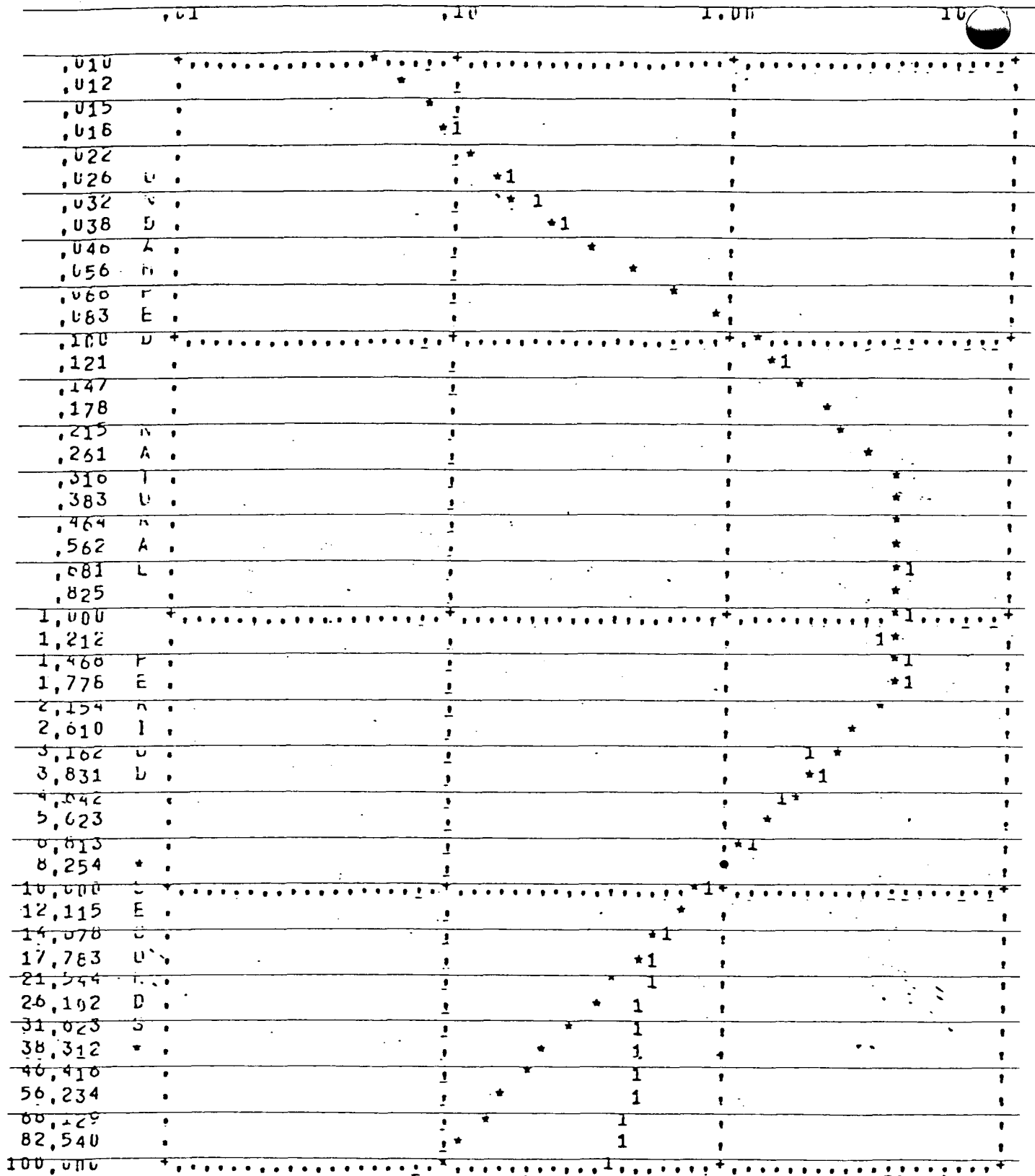


Figure 4-2.

TIME HISTORY FOR ISET=991

PSEUDO-RELATIVE VELOCITY (FT/SEC)



LAST ITERATION WITH NEW CORV

Figure 4-3.

At this stage the compilation of the code is complete and a few simple test runs have been made. To facilitate the interpretation of output, a graphics option is being added. It is anticipated that in the near future the code will be applied to more sophisticated test problems culminating with collaborative runs with the vertical array shake test rig.

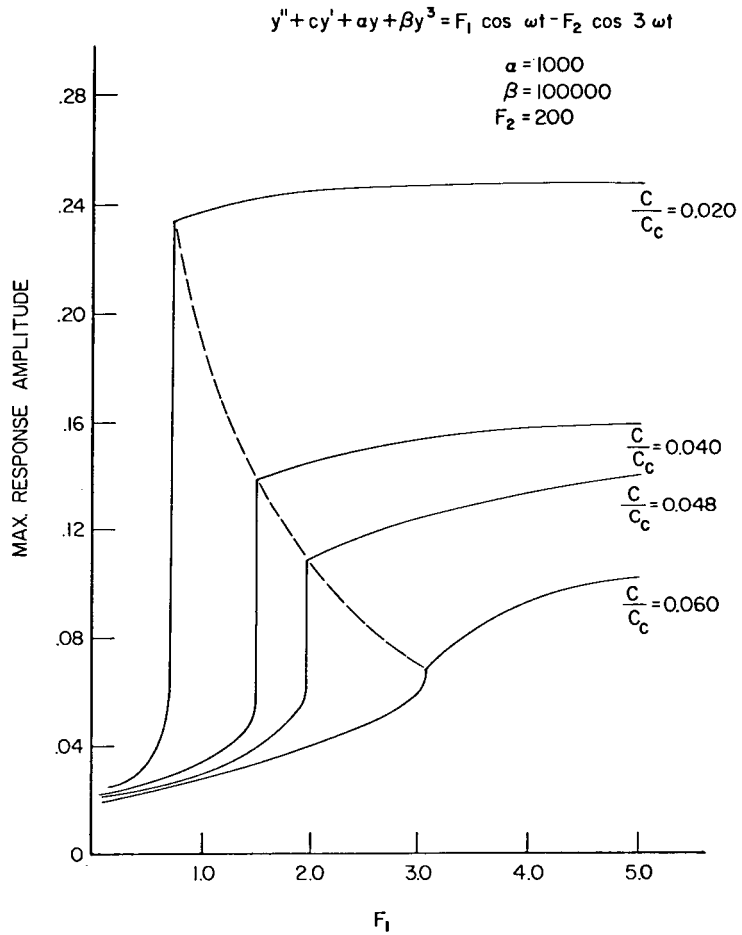
The fabrication and assembly of the vertical array shake test rig have been completed. Testing will commence shortly.

In the last quarterly some aspects of the response for a cubic non-linear system excited by two sine waves acting simultaneously was reported. It was noted that a critical "lock-on" value of the ratio of  $F_1/F_2$  exists for the equation

$$\ddot{y} + c\dot{y} + \alpha y + By^3 = F_1 \cos(\omega_1 t + \phi_1) + F_2 \cos(\omega_2 t + \phi_2).$$

This results in a discontinuity in the response. A small change in  $F_1$ , at the critical value, produces a substantial change in the response. As the coefficient  $F_2$  is decreased, the magnitude of the response discontinuity is reduced accordingly. To get a better qualitative understanding of this phenomena a limited parametric study was undertaken.

Figure 4-4 shows the effect of varying the coefficient of the cubic term as it affects the critical magnitude of  $F_1$ . Increasing the coefficient from 100,000 to 200,000 reduces the magnitude of  $A$  that is required to produce the discontinuity. This means that a



EFFECT OF DAMPING ON MAXIMUM RESPONSE

Figure 4-4. Effect of damping on maximum response.

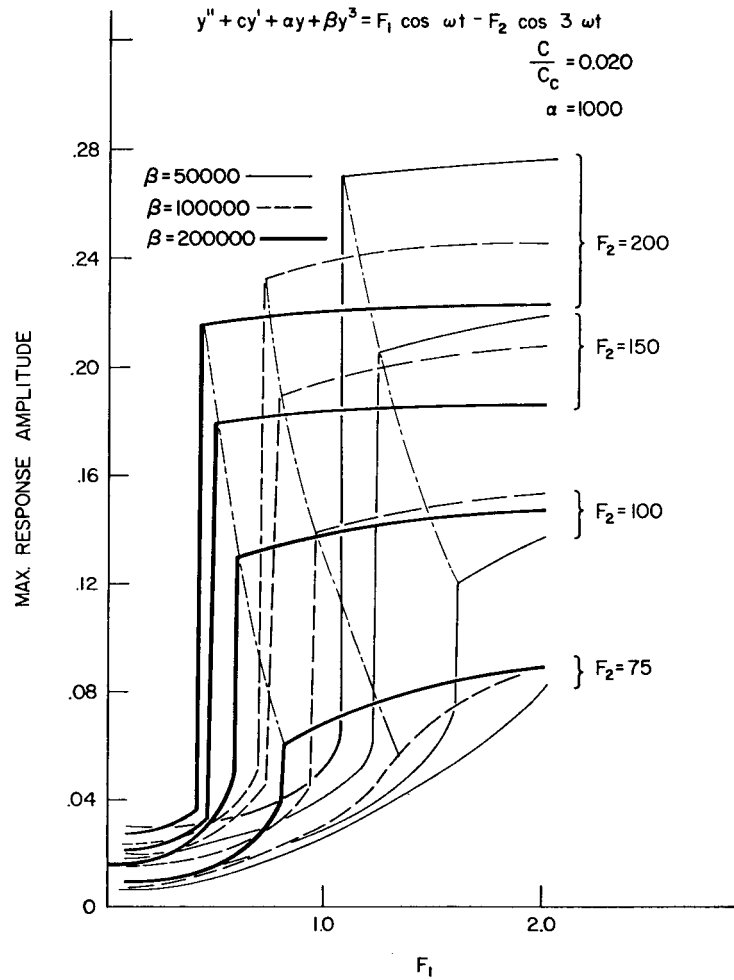
a smaller ratio of  $F_1/F_2$  is needed to produce a discontinuous response. However, the magnitude of the displacement jump is smaller for the stiffer system. Conversely, reducing the cubic coefficient to 50,000 increases the "lock-on" ratio but results in a greater displacement jump at the critical value.

Figure 4-5 shows the effect of damping on the magnitude of the critical value of  $F_1$ . For 2% of critical damping, there is a very large discontinuity in the displacement response. Additionally, the critical "lock-on" ratio is low. As the damping is increased, a larger magnitude of the coefficient  $F_1$  is required and a smaller discontinuity in the response curve results. Increasing the damping to 6% just about eliminates the discontinuity in the response. In this sense increased damping has an effect similar to a reduction in the cubic coefficient  $F_2$ .

This type of response develops because of the influence of the subharmonic excitation. The large magnitudes develop because of a coincidence between the third harmonic component of the forcing function and the third harmonic component of the motion. If each of the magnitudes  $F_1$  and  $F_2$  were introduced separately, the large subharmonic response effect could not occur.

It is normally expected that reduced damping would tend to increase the response. However, in this case, the increase is also accompanied by a sharp discontinuity in the response.





EFFECT OF MAGNITUDE OF  $F_1$  AND  $\beta$  ON MAXIMUM RESPONSE

Figure 4-5. Effect of magnitude of  $F_1$  and  $\beta$  on maximum response.

References

1. R. H. Scanlon, K. Sachs, Earthquake Time Histories and Response Spectra, Journal of the Engineering Mechanics Division, ASCE, August, 1974.

5. Task Area V - Materials

The scope of this effort covers four main categories of materials: (1) metallic materials, (2) graphites, (3) PCRV and (4) other materials, which include control rod and thermal barrier insulation. The objectives are to critically review available materials data pertinent to HTGR safety, identify areas where information is sparse or unavailable, and to design and initiate experiments to yield data which will permit accurate assessments to be made of materials-related safety problems.

The conceptual design has been completed for the Materials Test Loop (MTL), which will, when completed, be used to supply prototypic flowing helium to selected creep and fatigue machines.

Subcontracted work at the Aerospace Corporation is centered on developing an analytical model which will predict the fracture strength and fracture mechanisms of oxidized graphites.

5.1 Mechanical Properties of Materials (J. Chow, P. Soo)

New control consoles and actuator units have been received for three of the MTS closed-loop, electro-hydraulic fatigue machines and installation and calibration have been recently completed. Each machine is currently being used to test a new heat of Incoloy-800H (Heat HH7427A; 0.05% C, 0.39% Al, 0.43% Ti) at room temperature, using a new specimen design shown in Figure 5-1. These tests are being conducted to evaluate any differences from the previous specimen design,

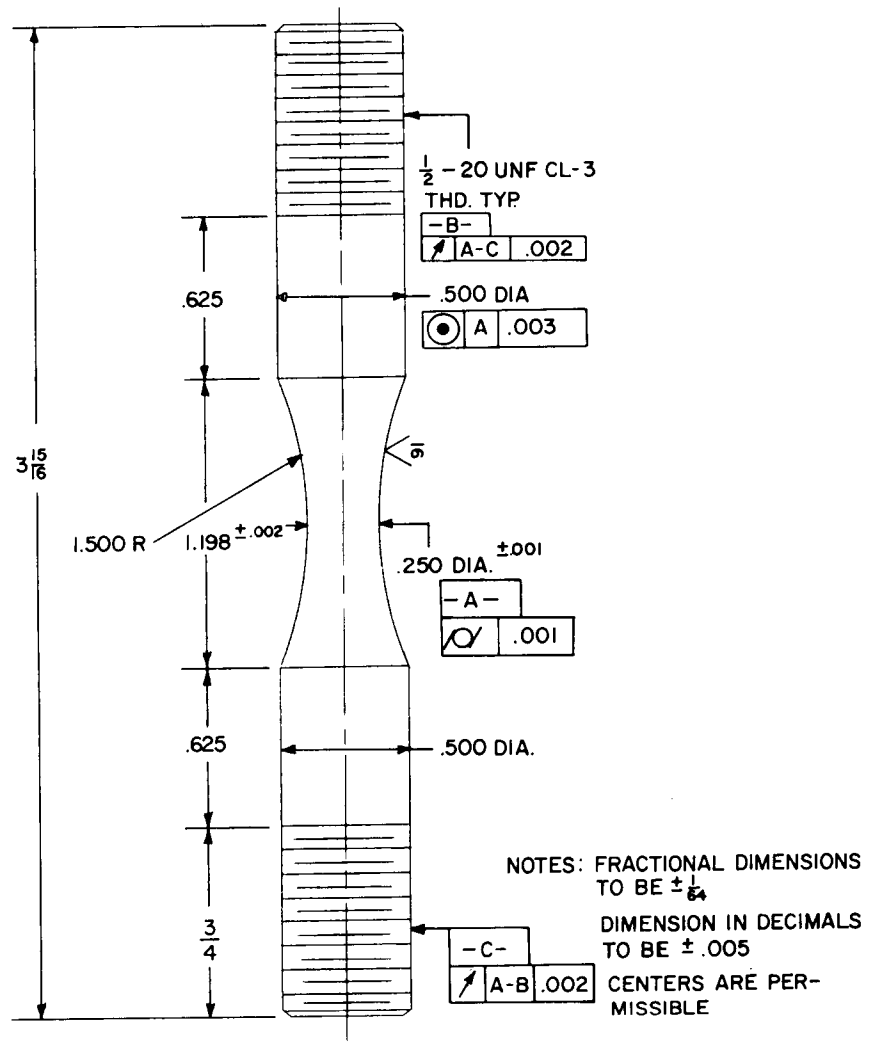


Figure 5-1. Standard BNL low and high cycle fatigue specimen.

which had a 1/8" cross-sectional diameter, and also to verify the integrity of the specimen grips. Four MTS fatigue machines are currently operational in the mechanical test laboratory. An additional 55,000-lb capacity unit equipped with a 22,000-lb load cell and actuator system has just been delivered.

Seven creep machines have been received from Applied Test Systems, Inc., and are currently being assembled and installed. They will not be operable, however, until the temperature controllers and strain measuring equipment is received.

#### 5.1.1 Fatigue Testing of Incoloy-800H

In the previous quarterly report it was shown that high cycle fatigue data generated under load-controlled conditions were correlatable with available strain-control, low-cycle information from the literature<sup>5-1,2,3</sup> provided that stress-to-strain conversions were made with the aid of cyclic stress-strain curves. Conversions using Young's moduli data are not valid since plasticity effects are not taken into consideration.

For both low- and high-cycle data, it was also shown that for a given test temperature, there was a good correlation between the total plastic strain energy per unit volume ( $W_p$ ) imparted to a specimen and the cycles-to-failure ( $N_f$ ), viz.:

$$W_p N_f^n = K \quad (1)$$

were  $n$  and  $K$  are material constants. However, a more complete and

straightforward analysis may be made of the data using an approach developed by Manson which correlates the elastic and plastic strain ranges ( $\Delta\epsilon_e$ ,  $\Delta\epsilon_p$ ) with  $N_f^{5-4}$ . The basis of this approach is shown in Figure 5-2. From an analysis of 29 different materials Manson demonstrated that the total strain range  $\Delta\epsilon_t$  ( $= \Delta\epsilon_e + \Delta\epsilon_p$ ) could be given by:

$$\Delta\epsilon_t = 3.5 \sigma_u E^{-1} N_f^{-0.12} + D^{0.6} N_f^{-0.6} \quad (2)$$

where the first term on the right-hand side is the elastic strain range and the second is the plastic strain range;  $\sigma_u$  is the ultimate tensile strength,  $E$  is Young's modulus, and  $D$  is a ductility term given by  $\ln(1 - RA)$  in which  $RA$  is the fractional reduction in cross-sectional area. From equation (2) it may be seen that at  $N_f = 1$ , the elastic and plastic strain ranges are given respectively by  $3.5 \sigma_u E^{-1}$  and  $D^{0.6}$ . By drawing lines of gradients  $-0.12$  and  $-0.6$  through each of these points the relationships between  $\Delta\epsilon_e$  and  $\Delta\epsilon_p$  and  $N_f$  are established, which then leads directly to the calculated  $\Delta\epsilon_t - N_f$  relationship, which is given by the broken line in Figure 5-2.

In the current analysis of the Incoloy-800H data it was decided not to assume that the gradients of the elastic and plastic lines were  $-0.12$  and  $-0.6$  but to actually determine the temperature dependences from available low- and high-cycle data. This may be achieved by rewriting equation (2) in the following form:

$$\Delta\epsilon_t = \Delta\epsilon_e + \Delta\epsilon_p = \alpha N_f^{-e} + \beta N_f^{-p} \quad (3)$$

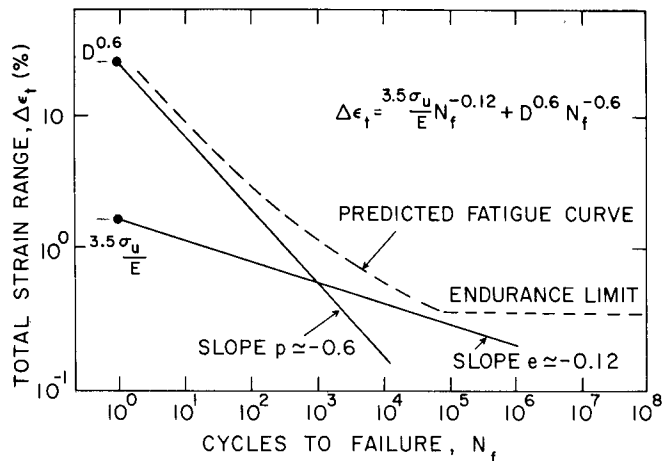


Figure 5-2. Model for fatigue life predictions.

where  $\alpha$ ,  $\beta$ ,  $e$  and  $p$  are temperature dependent terms. The values of  $e$  and  $p$  are obtained by plotting a series of  $\log \Delta\epsilon_e - \log N_f$  and  $\log \Delta\epsilon_p - \log N_f$  lines as shown in Figures 5-3 and 5-4. Values of  $\alpha$  and  $\beta$  are obtained from the expressions

$$\alpha = \Delta\epsilon_e N_f^e \quad (4)$$

and

$$\beta = \Delta\epsilon_p N_f^p \quad (5)$$

Figure 5-5 and 5-6 show the data obtained. Clearly, the average values of  $e$  and  $p$  determined by Manson are only applicable at high temperatures for Incoloy-800H.

To a reasonable approximation all of the data may be fitted to cubic equations as shown in Figures 5-5 and 5-6. Since there are no data for temperatures between room temperature and 800<sup>0</sup>F the calculated values may be in considerable error.

With the aid of equation (3), and the equations given in Figures 5-5 and 5-6, the fatigue curves for any temperature may be calculated. Figures 5-7 through 5-13 show a comparison between experimental and calculated values. The calculated curve was terminated at 10<sup>6</sup> cycles since, for some temperatures, an endurance limit is achieved and the correlation becomes invalid. The agreement between calculated and experimental fatigue lines is usually excellent, but there is some underestimation of the fatigue life at 1200 and 1300<sup>0</sup>F and some overestimation at 1100<sup>0</sup>F. Nevertheless, for  $N_f$  values up to



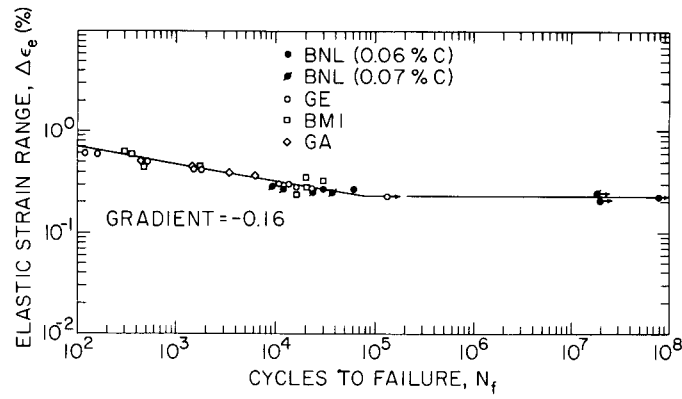


Figure 5-3. Correlation of elastic strain range and fatigue life for Incoloy-800H at 1200°F.

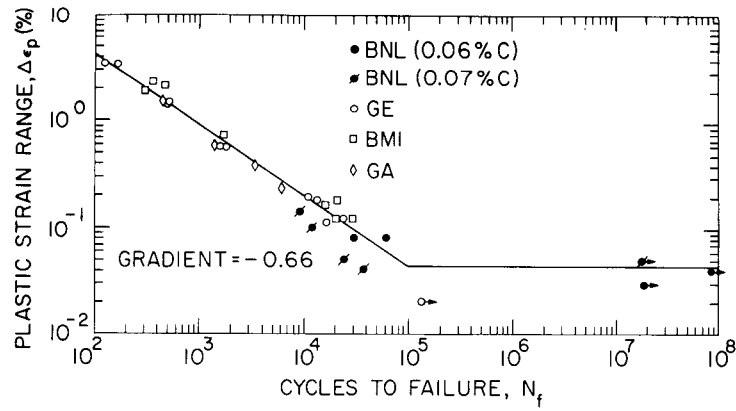


Figure 5-4. Correlation of plastic strain range and fatigue life for Incoloy-800H at 1200°F.

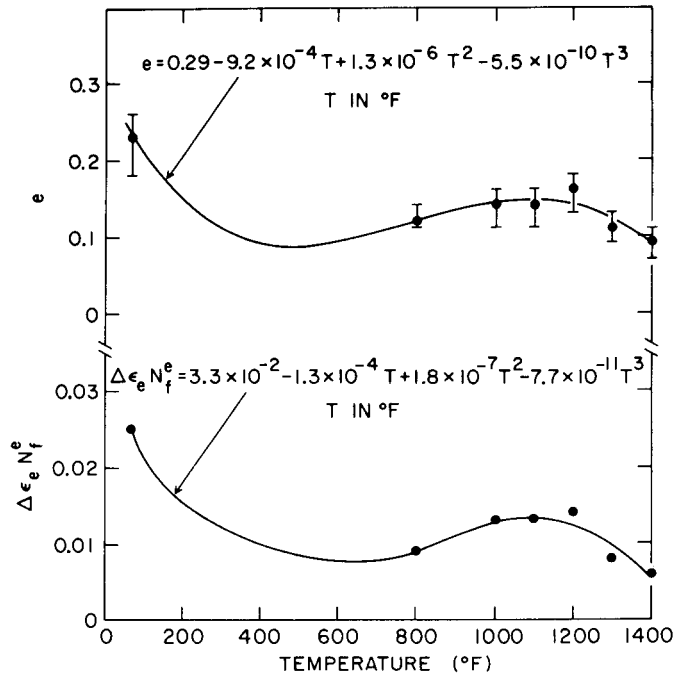


Figure 5-5. Temperature dependencies of  $e$  and  $\Delta \epsilon_e N_f^e$  for Incoloy-800H.

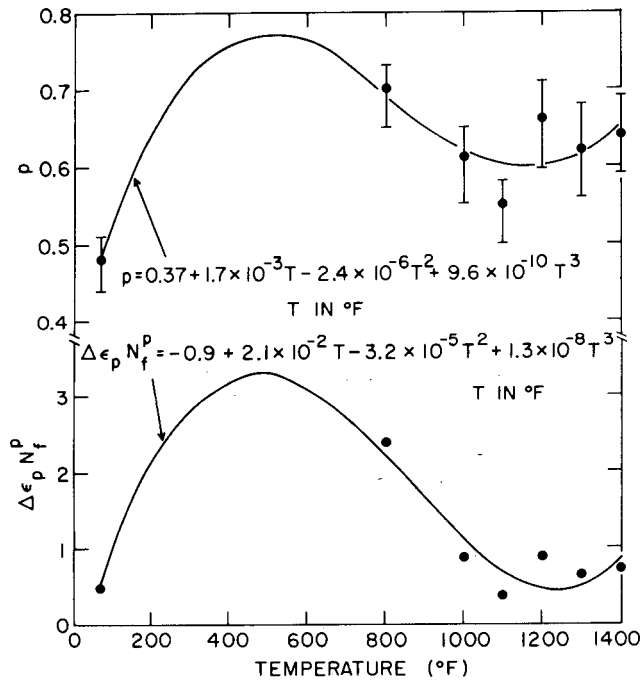


Figure 5-6. Temperature dependencies of  $p$  and  $\Delta \epsilon_p N_f^p$  for Incoloy-800H.

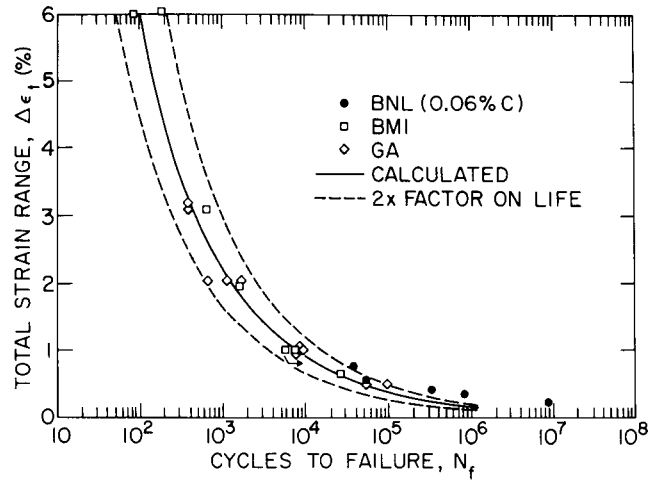


Figure 5-7. Comparison between calculated and measured fatigue lives for Incoloy-800H at 70°F.

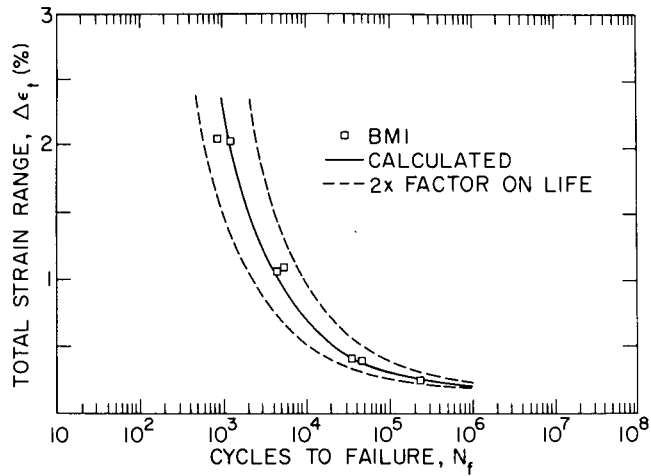


Figure 5-8. Comparison between calculated and measured fatigue lives for Incoloy-800H at 800°F.

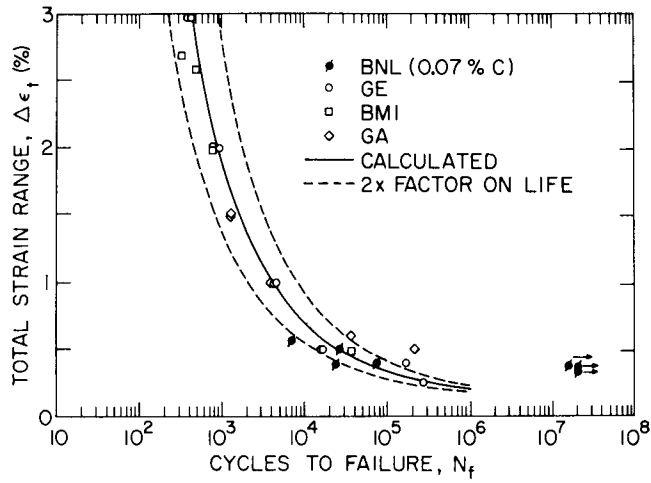


Figure 5-9. Comparison between calculated and measured fatigue lives for Incoloy-800H at 1000°F.

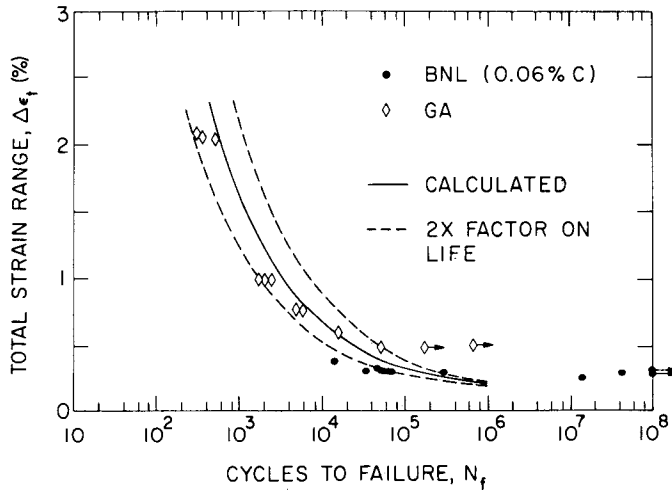


Figure 5-10. Comparison between calculated and measured fatigue lives of Incoloy-800H at 1100°F.

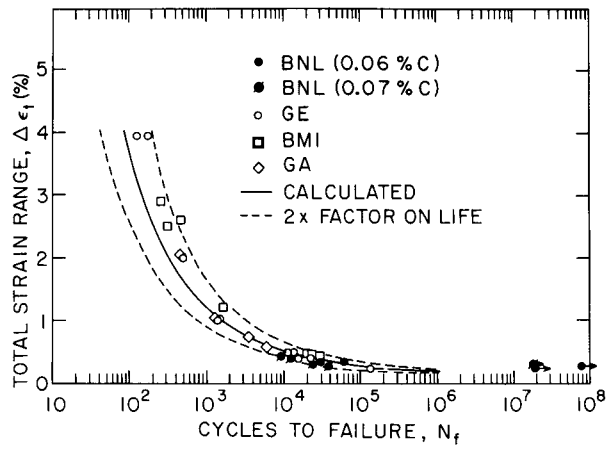


Figure 5-11. Comparison of calculated and measured fatigue lives for Incoloy-800H at 1200°F.

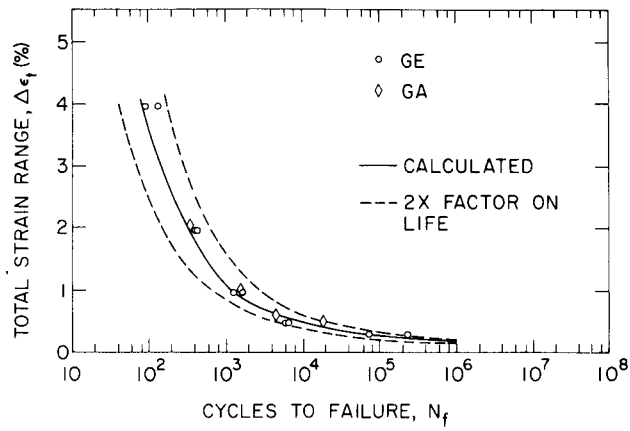


Figure 5-12. Comparison of calculated and measured fatigue lives for Incoloy-800H at 1300°F.

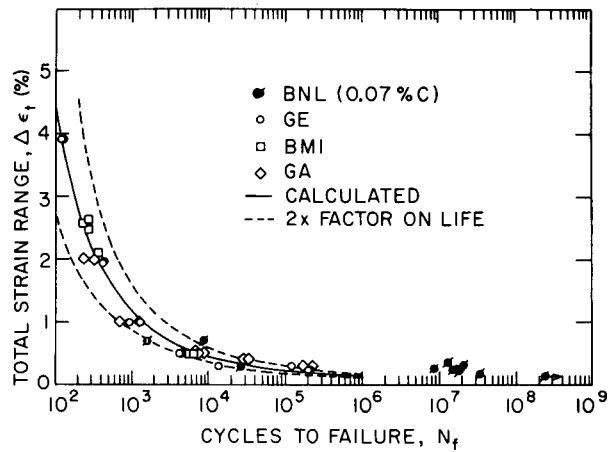


Figure 5-13. Comparison of calculated and measured fatigue lives for Incoloy-800H at 1400°F.

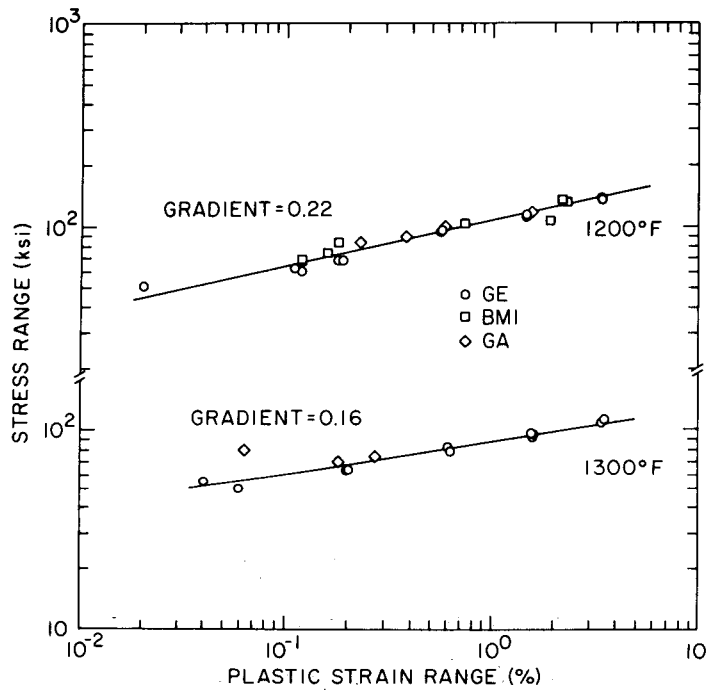


Figure 5-14. Stress range-plastic strain range relationships for Incoloy-800H at 1200 and 1300°F.

up to approximately  $10^5$ , the calculated values are almost always within a factor of 2 of the experimental ones. For  $N_f$  values greater than  $10^5$  the calculated values underestimate the fatigue life because of the tendency to reach the endurance limit. However, the calculated values may still be used to conservatively estimate fatigue behavior in this range.

Incoloy-800H is strengthened by the precipitation of the  $\gamma'$  phase,  $Ni_3(Al, Ti)$ , at high temperatures. Because of this, significant changes may be anticipated for longer-term tests where precipitation occurs. The nature of precipitation strengthening may be investigated by considering the rate of work hardening for cyclic straining. From data in references 5-1 through 5-3 it may be shown that the cyclic plastic work hardening rate,  $m$ , for Incoloy-800H at a given temperature is described by the relationship:

$$\Delta\sigma = A \Delta\epsilon_p^m \quad (6)$$

Where  $\Delta\sigma$  is the stable stress range and  $A$  is a material constant. Figure 5-14 gives typical data for 1200 and 1300°F. The overall temperature dependence of  $m$  is shown in Figure 5-15. It appears that maximum precipitation effects and fatigue strengthening are likely at about 1100°F. Below 800°F precipitation probably is absent and a different strengthening mechanism is controlling fatigue.

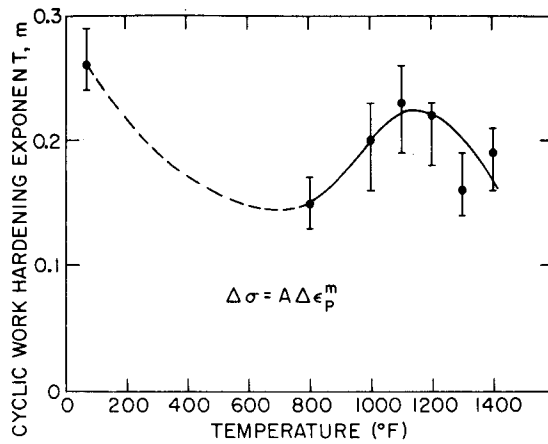


Figure 5-15. Temperature dependence of the cyclic work hardening exponent for Incoloy-800H.

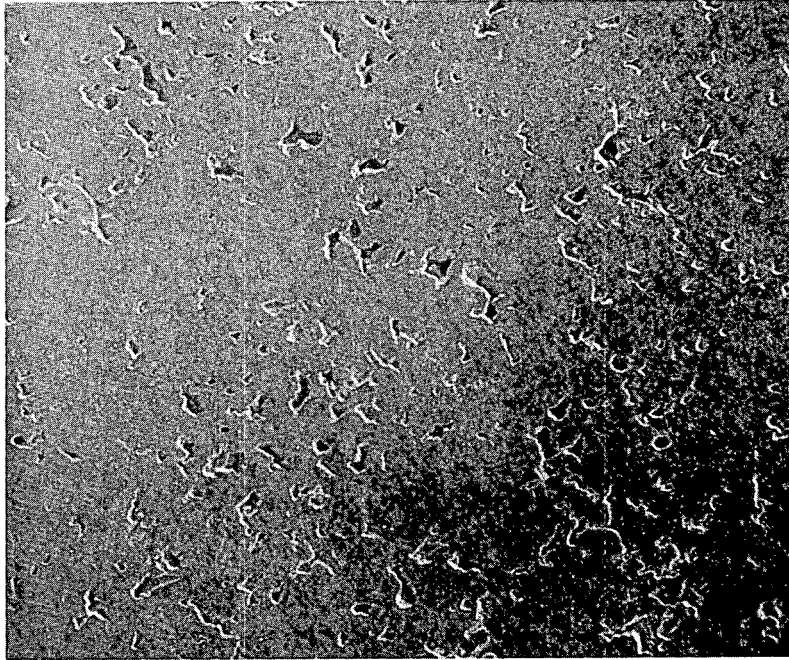
Table 5-I Weight Loss of Graphite Specimens  
Oxidized in HIL

No.	Graphite	Weight Loss, Percent	Temperature, °C
A1	PGX	0.902	800
A2	PGX	0.165	740
A3	PGX	0.516	800
A4	PGX	0.202	740
A5	ATJ	0.109	800
A6	ATJ	0.096	740
A7	2020	0.089	800
A8	2020	0.085	740

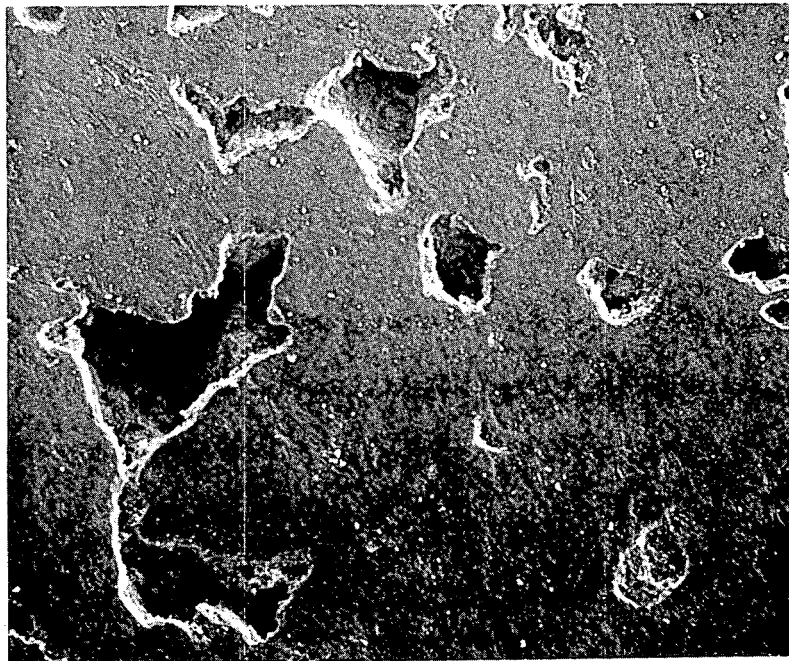


5.2 Microstructure and Fracture of HTGR Graphite (J. E. Zimmer -  
The Aerospace Corporation)

Polished specimens of three graphites were oxidized in the BNL Helium Impurities Loop (HIL). This low-level oxidation, compared to oxidation in air, is more representative of that which might occur in an HTGR. Specimens of ATJ, PGX and Stackpole 2020 graphite were oxidized in the HIL under the planned conditions of 1000 ppm H<sub>2</sub>O at 750C. The weight loss for each specimen was measured at BNL prior to the SEM analysis at Aerospace. The HIL oxidation run did not achieve the overall burnoffs that were originally desired. The weight loss for each of the eight graphite specimens is given in Table 5-1. All the weight losses were less than one percent. Scanning electron micrographs of the oxidized surface at ATJ graphite (Figure 5-16) show no evidence of oxidation. This is in contrast to the micrographs of the surface of ATJ graphite oxidized in air to a much higher burnoff of 5.0 w/o (Figure 5-17). In this case, enough material has been removed to produce surface relief that corresponds to the preferential oxidation of the edges of the graphitic basal planes. However, for the HIL oxidized specimens, no surface relief was produced and only the fine scratches of the initial surface polishing are still evident. Other micrographs (Figure 5-18) show this same lack of surface relief due to the oxidation.

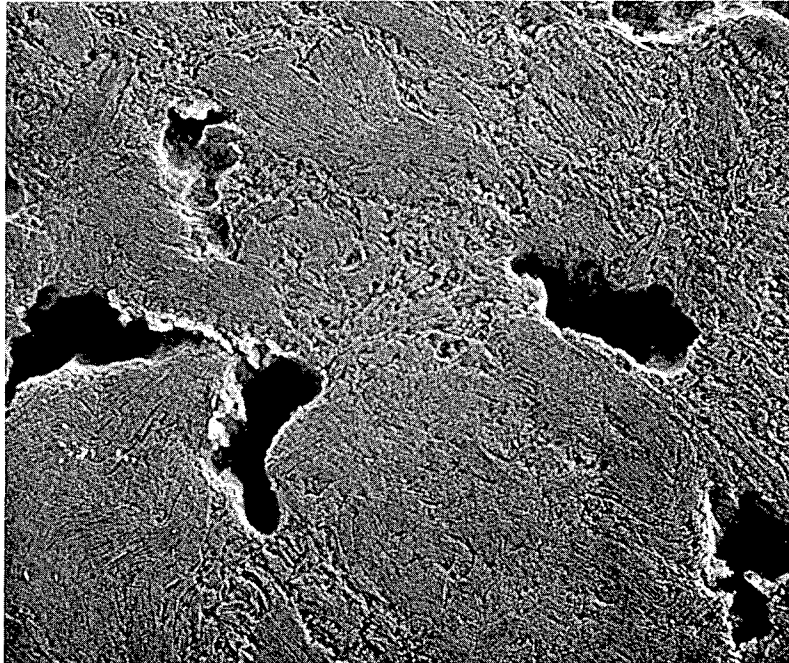


100X



600X

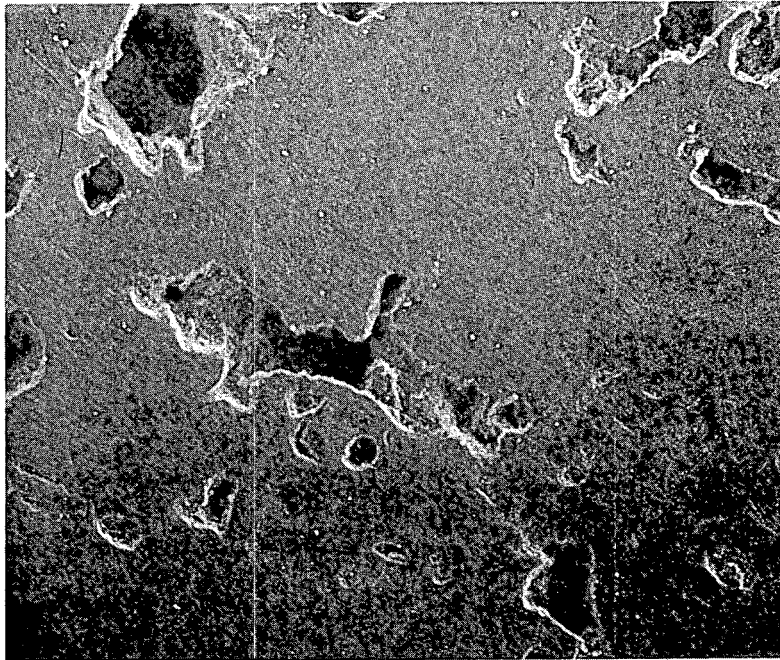
Figure 5-16. Scanning electron micrographs of HIL oxidized surface of ATJ graphite; 0.109 w/o burnoff.



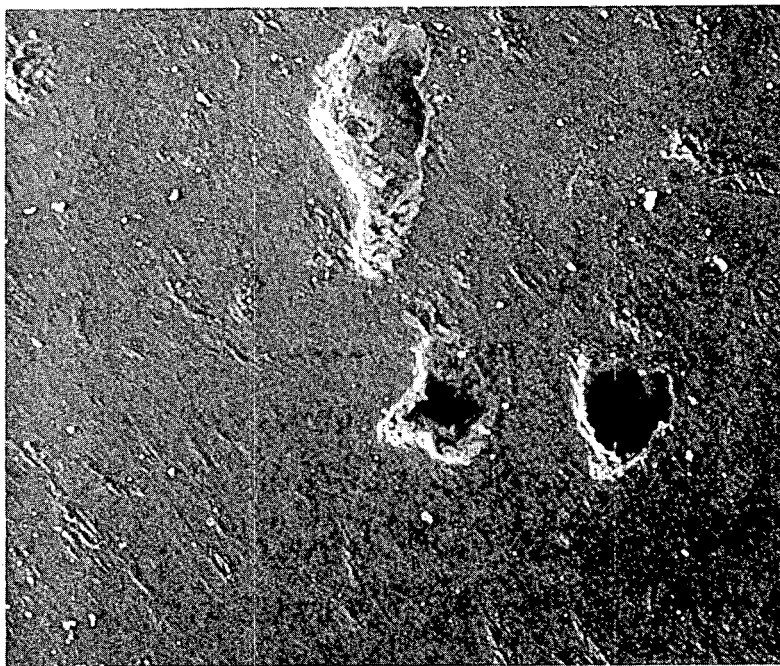
1000 X

Figure 5-17. Scanning electron micrograph of air oxidized surface of ATJ graphite; 5.0 w/o burnoff.

✓



600x



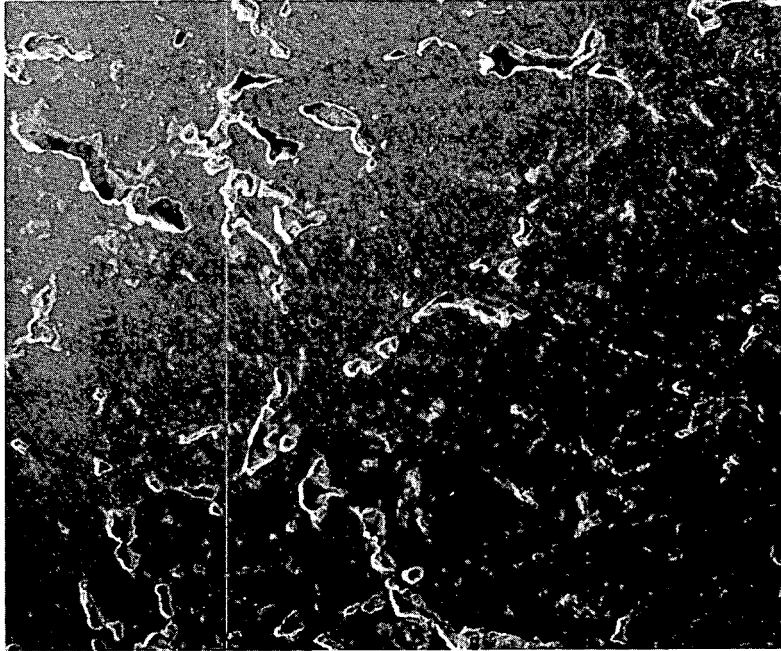
1200x

Figure 5-18. Scanning electron micrographs of HIL oxidized surface of ATJ graphite; 0.109 w/o burnoff.

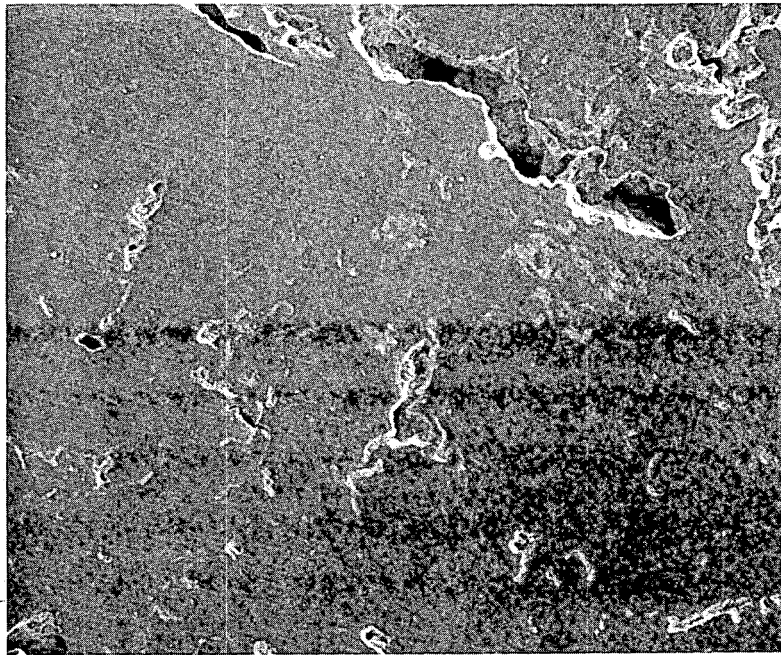
The PGX graphite specimens similarly showed no evidence of this low-level oxidation, as did the Stackpole 2020 graphite specimens. Scanning electron micrographs of the surface of the PGX graphite specimen are shown in Figure 5-19.

Stackpole 2020 graphite is currently the leading candidate material for the support posts in the HTGR, replacing ATJ graphite. To gain a better understanding of this graphite, optical micrographs were taken of polished cross sections. These micrographs (Figure 5-20) show that Stackpole 2020 is a very fine grain graphite comprised of filler grains generally less than 30  $\mu\text{m}$  in size. Some grain agglomeration is present and the pore structure consists of rather small pores outlining the agglomerates. The microstructure of Stackpole 2020 is somewhat different to that of the ATJ graphite.

In the future the oxidation of the polished surfaces of the HTGR graphites in the Helium Impurities Loop and the subsequent scanning electron micrography of the oxidized specimens should be repeated. At higher levels of oxidation, the relation between oxidation and the graphite microstructure could be determined. To gain an understanding of the relation between mechanical properties and weight loss due to oxidation, fracture test specimens should be analyzed micrographically. This study could relate the mode of fracture in tension and compression to the changes in the graphite microstructure that result from oxidation.



100X



200X

Figure 5-19. Scanning electron micrographs of HIL oxidized surface of PGX graphite; 0.902 w/o burnoff.



100 x



500 x

Figure 5-20. Optical micrographs of Stackpole 2020 graphite.

### 5.3 Effect of Oxidation on Strength of Graphite

#### 5.3.1 Effect of Impurities on Graphite Oxidation (A. Romano)

The Helium Impurities Loop (HIL) has been used to expose several graphites to He containing nominal amounts of moisture and other concomitant impurities, i.e.  $H_2$ , CO,  $CO_2$  and  $CH_4$ . The graphites have been exposed in the form of tensile specimens, compression specimens and metallographic specimens. The types of graphites exposed were H451 (core graphite), ATJ and 2020 (core support post) and PGX (support block).

The impurity concentrations in the loop were governed primarily by the mode of operation, ie water was injected continuously to a steady state level with  $H_2$ , CO,  $CO_2$ , and  $CH_4$  produced but not controlled. A recent modification of the water injection and control system has resulted in a more uniform water concentration in the loop. Since the other impurities were not controlled, they gradually increased in concentration during a test run until complete purification of the gas was performed.

The results of three exposure runs will be reported. These runs are: (1) tensile specimens of H451, ATJ, 2020 and PGX graphites at a nominal  $H_2O$  concentration of 100 ppmv, (2) compression specimens of PGX graphite at a nominal  $H_2O$  concentration of 1000 ppmv, and (3) metallographic specimens of ATJ, 2020 and PGX graphites (for Aerospace Corporation subcontract) at a nominal level of 1000 ppmv  $H_2O$ . The HIL has been operated for a total of nearly 3000 hours which included



the following exposures of graphite specimens:

<u>Specimen Type</u>	<u>Exposure time, 18 hrs.</u>	<u>H<sub>2</sub>O, ppmv</u>	<u>Max. Temp. °C</u>
Tensile	up to 1974	100	750
Compression	453	1000	775
Metallographic	299	1000	800

After 1974 hours of exposure at the conditions shown in Table 5-2, all of the graphite tensile specimens were removed and post-exposure examination was started. Examination of these samples consists of oxidation rate measurements (weight changes), tensile strength measurements, density profile determinations and chemical analysis (metal impurities).

A schematic representation of one of three test retorts is given in Figure 5-21. The drawing indicates the relative positioning of samples and the specimen identification numbers.

A summary of the graphite tensile specimens in HIL and the duration of exposure in each case is shown in Table 5-3. Of the graphites tested, only the PGX specimens showed significant changes since the last weighing (reported in the previous progress report). Therefore the results for H451, ATJ and 2020 will not be plotted at this time, but reported as mean oxidation rates are as follows:

Table 5-2

Summary of Operation of Helium Impurities Loop

Main Flow Circuit

Maximum Gas Circulating Pump Flow = 1350 std.  $\ell$ /min  
 Mean Loop Pressure = 1.19 atmosphere

Test Retort Circuit

Maximum Flow per Retort = 240  $\ell$ /min  
 Mean Temperature Gradient = 600 to 750°C  
 Average Velocity in Retort = 292 cm/sec (9.6 ft/sec)

Impurity Monitoring

Water Concentration, mean: 100 ppmv

CO<sub>2</sub> Concentration, mean: 250 ppmv

Ratios of Impurities:  $\frac{H_2}{H_2O}$  = 20 mean

$\frac{H_2}{H_2O}$  = 1000 max.

$\frac{CO}{CO_2}$  = 10 mean

$\frac{CO}{CO_2}$  = 500 max.

Methane Concentration, mean: 100 ppmv

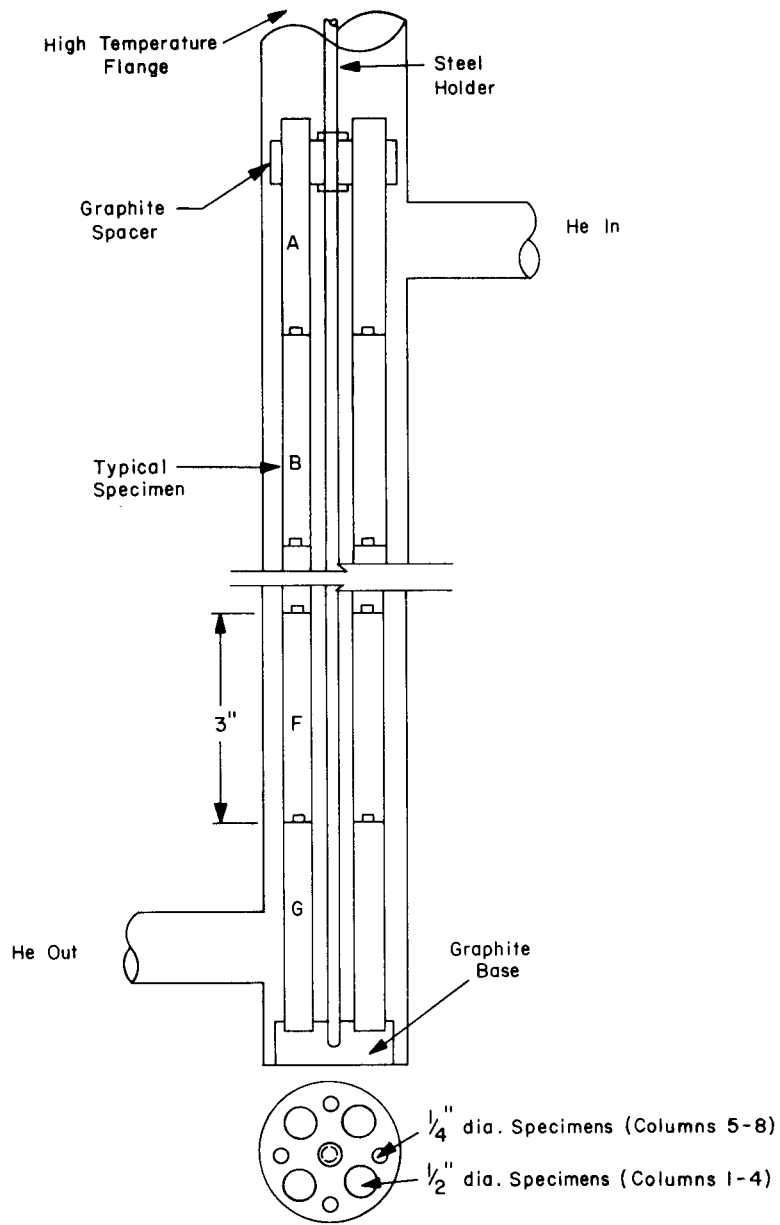


Figure 5-21. Graphite tensile specimen test section.

Table 5-3

## Summary of Tensile Specimens Exposed in Helium Impurities Loop

<u>Type of Graphite</u>	<u>Grain Orientation(1)</u>	<u>Diameter of Specimen, in.(2)</u>	<u>Number of Specimens</u>	<u>Duration of Test, hrs</u>
H451	WG	1/2	5	661
	AG	1/2	2	661
	WG	1/2	5	1305
	AG	1/2	2	1305
	WG	1/2	5	1974
	AG	1/2	2	1974
	WG	1/4	5	1305
	AG	1/4	2	1305
	WG	1/4	20	1974
	AG	1/4	8	1974
ATJ	WG	1/2	18	1974
	AG	1/2	12	1974
	WG	1/4	37	1974
	AG	1/4	12	1974
2020	AG	1/2	7	669
PGX	WG	1/2	7	669
	WG	1/2	21	1974
	AG	1/2	12	1974

(1) WG - with grain, AG - against grain.

(2) All specimens are 3 inches long.

<u>Type of Graphite</u>	<u>Number of Specimens</u>	<u>Diameter</u>	<u>Mean Oxidation Rate mg/g-h</u>
H451	21	$\frac{1}{2}$	$1.27 \times 10^{-4}$
H451	35	$\frac{1}{4}$	$1.93 \times 10^{-4}$
ATJ	30	$\frac{1}{2}$	$2.96 \times 10^{-4}$
ATJ	49	$\frac{1}{4}$	$9.64 \times 10^{-4}$
2020	7	$\frac{1}{2}$	$2.17 \times 10^{-4}$

The mean temperature associated with this exposure calculated from temperature profile measurements was 675°C. Detailed temperature profiles and the relationship of weight loss vs. temperature were shown in the previous report.

The PGX samples showed a significant weight loss since the last weighing. The total weight change for the PGX graphite specimens are plotted as mg/gr-h vs. reciprocal absolute temperature in Figure 5-22. Included in the data are weight change measurements from samples recently put into the test retorts (669 hour exposure). The temperature dependence is about equal to that observed after 1136 hours. Considerable scatter continues to exist in the results and it is expected that the scatter can be explained by sample to sample metallic impurity variations. Chemical Analysis of several specimens is presently underway. The highest single sample burnoff was about 13% for sample 1-3D and the mean burnoff obtained from the data at 750°C was about 8%.

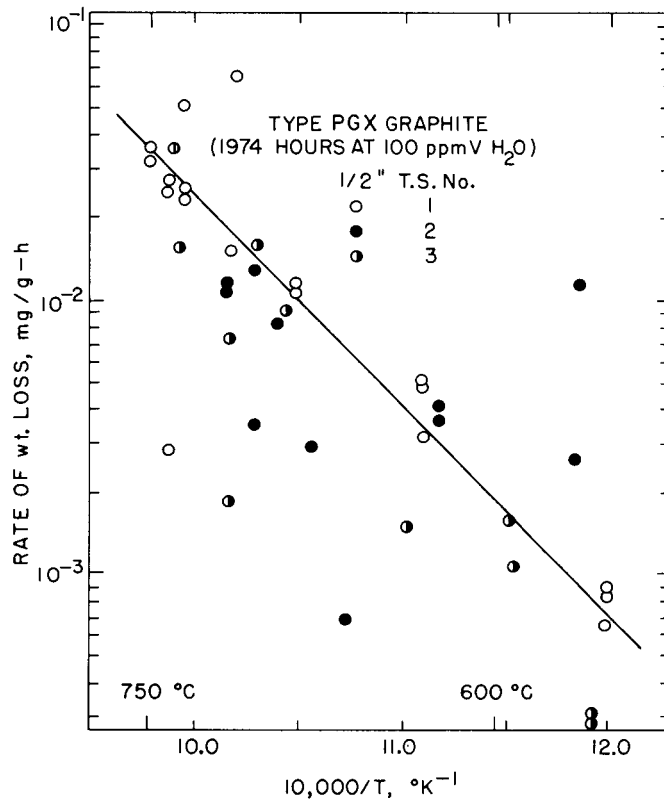


Figure 5-22.

Several PGX compression type samples (1" diameter x 2" long) were exposed in HIL at accelerated conditions (temperature and moisture concentration, 775°C maximum and 1000 ppmv H<sub>2</sub>O respectively). The exposure was for only 453 hours. The weight change data for these specimens are given in Table 5-4. Once again considerable scatter is observed in the results. The effect of the higher moisture content appears to be more pronounced at lower temperature. For example, the rates for the compression samples at 650°C are about twice that for the tensile specimens even when normalized for surface area. The sample set A showed an average weight loss about  $\frac{1}{4}$  that for set B. This apparent anomaly can be explained by the location in the log from which the specimens were obtained. Set A was obtained from the end of the log nearest the mold surface. Chemical analysis of samples from the log showed that the Fe concentration was lower at the surface.

Several metallographic specimens were oxidized in the HIL for subsequent examination by Aerospace Corp. See section 5-2 of this report for the results of that examination. The specimens were exposed at 800°C (maximum) and 1000 ppmv H<sub>2</sub>O for 299 hours. The results of weight change measurements are given in Table 5-5. The results are in agreement with previously reported data for both the tensile specimens and compression specimens. Once again, however, there is a less than linear relationship to water concentration when comparing these data (at 1000 ppmv H<sub>2</sub>O vs. the data from the tensile specimens (at 100 ppmv H<sub>2</sub>O)).

Table 5-4

## Weight Loss Data for PGX Compression Samples

<u>Temp, °C</u>	<u>Rate of Weight Loss, mg/g-h</u>	
	<u>Set A</u>	<u>Set B</u>
650	$7.12 \times 10^{-3}$	$2.37 \times 10^{-2}$
670	$5.67 \times 10^{-3}$	$6.52 \times 10^{-2}$
705	$1.32 \times 10^{-2}$	$4.09 \times 10^{-2}$
725	$6.12 \times 10^{-3}$	$9.12 \times 10^{-2}$
755	$1.01 \times 10^{-2}$	$3.02 \times 10^{-2}$
765	$3.93 \times 10^{-3}$	$4.89 \times 10^{-2}$
775	$5.32 \times 10^{-3}$	$1.88 \times 10^{-2}$
750	<u><math>2.64 \times 10^{-3}</math></u>	<u><math>1.75 \times 10^{-2}</math></u>
Average	= $6.76 \times 10^{-3}$	$4.21 \times 10^{-2}$

Table 5.5

## Aerospace Corporation Specimens\* Weight Change Measurements

<u>No.</u>	<u>Type</u>	<u>Weight Loss, mg/g-h</u>	<u>Temp, °C</u>
A1	PGX	$3.01 \times 10^{-2}$	800
A2	PGX	$5.51 \times 10^{-3}$	760
A3	PGX	$1.72 \times 10^{-2}$	800
A4	PGX	$6.74 \times 10^{-3}$	725
A5	ATJ	$3.60 \times 10^{-3}$	800
A6	ATJ	$3.20 \times 10^{-3}$	750
A7	2020	$2.97 \times 10^{-3}$	800
A8	2020	$2.85 \times 10^{-3}$	735

\*Samples exposed in Helium Impurities Loop for 299 hours and 1000 ppmv H<sub>2</sub>O.



### 5.3.2 Mechanical Property Measurements (A. Romano, J. Chow)

Since the highest weight losses were measured on the PGX samples, it was anticipated that the largest changes in tensile strength would also be observed on those samples. Therefore several PGX samples having high burnoffs were tested and only a small number of ATJ samples were tested.

The results of the tensile strength measurements of the PGX samples are given in Table 5-6. Several trends are observed:

1. Controls taken with the grain averaged  $1000 \pm 43$  psi whereas controls taken against the grain averaged  $1159 \pm 86$  psi in strength.
2. Similarly at the same burnoff, oxidized samples taken with the grain showed lower strengths than those taken against the grain.
3. As expected, the higher burnoff samples showed lower strengths. Specimens with the grain decreased in strength by a factor of one half after only 5-6% burnoff.

A review of the literature<sup>5</sup> regarding the loss in strength of graphite with loss in weight due to oxidation has indicated that most of the data fits a relationship of the type:

$$\frac{S}{S_0} = \left( \frac{\rho}{\rho_0} \right)^\alpha$$

where  $S$  and  $\rho$  are rupture stress (compression, tensile, etc) and density respectively and  $\alpha$  an empirically determined constant. It can be shown that the equation can be reduced to:

$$S = S_0 (1 - W_L)^\alpha$$

Table 5-6

## Results of Tensile Strength Measurements of PGX Graphite

<u>Standards Unexposed</u>			
<u>Sample No.</u>	<u>Grain Orientation</u>		<u>Stress, psi</u>
G-5	With Grain		960
G-6	"		1010
G-7	"		1070
G-8	"		960
G-10	"		975
G-11	"		1025
Average			1000 $\pm$ 43
G-13	Against Grain		1070
G-14	"		1230
G-15	"		(540)*
G-16	"		1100
G-17	"		1235
Average			1159 $\pm$ 86
<u>Samples Exposed in HLL</u>			
<u>Sample No.</u>	<u>Grain Orientation</u>	<u>Burnoff, %</u>	<u>Stress, psi</u>
1-3A	With Grain	0.13	970
1-4A	"	0.17	810
2-4B	"	0.73	852
1-4B	"	0.97	906
1-3B	"	1.02	925
1-1D	"	1.03	760
2-3E	"	1.62	865
1-1E	"	2.60	805
2-3F	"	2.73	765
3-3E	"	2.88	815
1-3G	"	4.28	685
1-3F	"	5.21	500
1-3E	"	6.47	565
2-3D	Against Grain	0.58	1005
1-3C	"	2.08	995
2-4G	"	2.10	1150
1-4F	"	4.91	745
3-4F	"	6.57	840
1-4G	"	10.21	656
1-3D	"	12.79	645

\*Not included in average.

where  $W_L$  is the fractional burnoff of the graphite. However, most of the data available in the literature is for pile grade graphite (low Fe content) although some data exists for Type CS graphite (commercial grade similar to ATJ). In addition, much of the data is for air and  $CO_2$  oxidation and at temperatures ranging from 200 to  $950^\circ C$ . A review of the literature indicates that values of  $\alpha$  for tensile strength data range from 8.0 to 13.5 with most of the data close to 8.0.

The results for PGX shown in Table 5-6 are plotted in Figure 5-23 in the form, log tensile strength vs. % burnoff. The results for samples taken with the grain and those taken against the grain are clearly separable into two curves. The slopes of these curves ( $\alpha$ ) are 5.1 and 9.2 for with grain and against grain, respectively. This indicates that for PGX the relationship of loss of strength with loss of weight is similar to pile grade graphites.

The results of the compression test measurements made on the PGX graphite specimens are given in Table 5-7. Unfortunately the exposure for these samples was not long enough to give high burnoffs. The data was reduced into three groups as shown. A slight reduction in strength is evident with the slight burnoff observed.

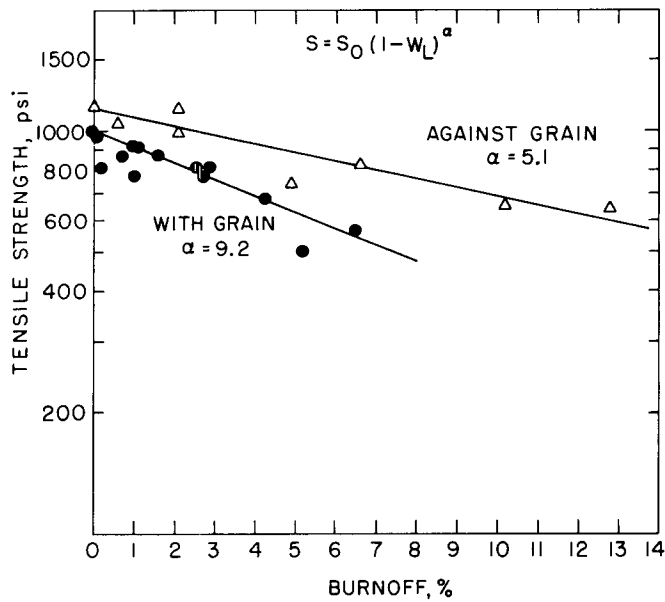


Figure 5-23. Tensile strength of PGX graphite as a function of extent of oxidation.

Table 5-7  
Results of PGX Compression Test Measurements

Unexposed

<u>Sample No.</u>	<u>Stress, psi</u>
GT50-8A	3670
GT53-8B	3710
GT51-11A	3860
GT53-11B	3840
Average	$3770 \pm 94$

Oxidized

<u>Sample No.</u>	<u>Burnoff, %</u>	<u>Stress, psi</u>
9A	0.12	3740
6A	0.18	3530
2A	0.26	3800
Average	0.19	$3690 \pm 142$
4A	0.28	(1520)*
7B	0.85	3540
1B	1.07	3650
5B	1.37	3530
3B	1.85	3490
Average	1.29	$3553 \pm 69$

\*Not included in averages.

### 5.3.3 Density Profile Measurements

Density profile measurements were made on some of the samples exposed to He and compared with unexposed standards. The results are summarized in Table 5-8. In general, the results are inconclusive. Several samples showed complex density profiles but the majority of those examined showed either flat profiles or only slight changes near the surface. There does not appear to be a correlation with exposure time, temperature, position or grain orientation. The more complex profiles are shown in Figure 5-24. Of interest to note is that samples 1-3D and 1-4G, which had high burnoffs, had very low densities (1.55 g/cc) as compared to samples having low burnoffs (1.7 g/cc).

The density profiles measured on two compression samples are shown in Figure 5-25. These samples had a near-linear change in profile from their outer edge to depths of about 0.2". The apparently greater depth of penetration of these samples, as compared to the tensile specimens, is probably due to the higher water concentration at the time of exposure.

Table 5-8  
Summary of Density Profile Measurements (PGX Graphite)

Sample No.	Burnoff, %	Grain Orientation	Tensile Strength, psi	Density Profile
Control	0	WG	960	Flat all way at 1.770 g/cc
3-3F	3.30	WG	(1)	Flat all way at 1.758 g/cc
1-3A	0.13	WG	970	Flat all way at 1.761 g/cc
1-1E	2.60	WG	805	Flat all way at 1.706 g/cc
2-4B	0.73	WG	852	1.752 g/cc at .50 in. to 1.756 at .48 in., then flat all way
2-3E	1.62	WG	865	1.740 g/cc at .50 in. to 1.749 at .48 in., then flat all way
1-3F	2.73	WG	765	1.709 g/cc at .50 in. to 1.712 at .48 in., then flat all way
1-3G	4.28	WG	685	1.738 g/cc at .50 in. to 1.742 at .45 in., then flat all way
2-3D	0.58	AG	1005	1.735 g/cc at .50 in. to 1.738 at .48 in., then decreased to 1.734 at .40 in.
3-4F	6.57	AG	840	1.706 g/cc at .50 in. to 1.710 at .48 in., then flat all way

(1) Not tested.

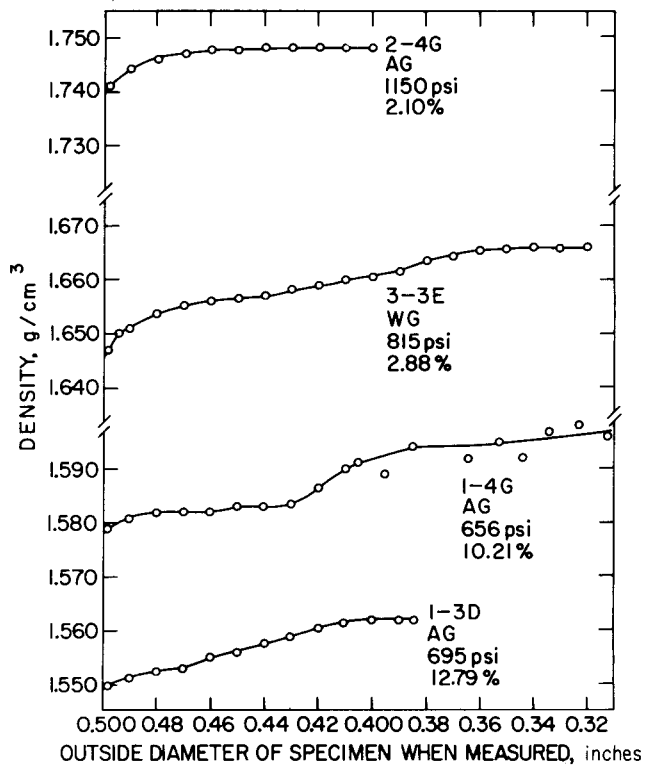


Figure 5-24. PGX graphite density profiles after oxidation.

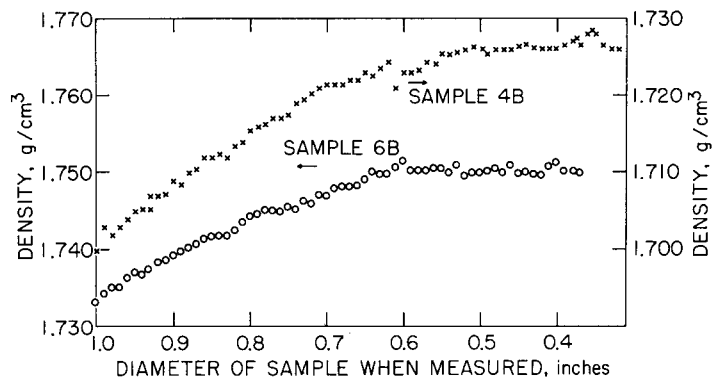


Figure 5-25. Density profiles of compression samples after oxidation.

#### 5.3.4 Discussion

The results from the tensile test measurements of PGX graphite specimens clearly indicate that the relationship between loss of strength and loss of weight due to oxidation is exponential. Although there appears to be an effect due to grain orientation, the data is in agreement with available data from the literature. If one can extrapolate the more design conservative values obtained for PGX (with grain), at 17% burnoff the tensile strength would be 200 psi, 0.2x the original strength. The application of engineering safety factors to this data would further reduce the allowable design stress.

There are obviously three major factors that must be considered before conclusions may be drawn. The first is the effect of size. These data (as well as most data available) are for small diameter specimens, in this case  $\frac{1}{2}$ ". The depth of oxidation in a small specimen may represent a large proportion of the overall diameter, whereas in large support blocks, the depth will have to be considerable to have an effect. The second factor is the effect of impurity level in the He. In HIL the impurity levels were not controlled except for H<sub>2</sub>O. The multiple effects of H<sub>2</sub>, CO<sub>2</sub>, CO and CH<sub>4</sub> on graphite oxidation are uncertain. However, if one considers that the loop operates at ~1 atm whereas an HTGR would operate at 50 atm, 100 ppmV in HIL would be equivalent to ~2 ppmV in an HTGR. The Technical Specification Limits for Ft. St. Vrain are well within the operating range at 2 ppmV. The third, and probably most important,



Table 5-9  
Weight Loss of Graphite Specimens Oxidized in HIL

<u>No.</u>	<u>Graphite</u>	<u>Weight Loss, %</u>	<u>Temp., °C</u>
A1	PGX	0.902	800
A2	PGX	0.165	740
A3	PGX	0.516	800
A4	PGX	0.202	740
A5	ATJ	0.109	800
A6	ATJ	0.096	740
A7	2020	0.089	800
A8	2020	0.085	740

factor to consider is exposure time. The PGX specimens were exposed for only ~2000 hours, whereas an HTGR is expected to operate for ~280,000 hours.

In summary, it has been shown that of all the graphites in an HTGR, the PGX graphite (due to its high metallic impurity concentration) is oxidized at a sufficiently high rate that some further consideration is required. There appears to be a need for further tests on PGX to determine the effect of size and long time exposures.

## References

1. J. B. Conway, "Short-Term Tensile and Low-Cycle Fatigue Studies of Incoloy-800," GEMP-732, December 1969
2. C. E. Jaske, H. Mindlin and J. S. Perrin, "Low-Cycle Fatigue and Creep-Fatigue of Incoloy Alloy 800," BMI-1921, February 1972.
3. C. M. Young, "Fatigue and Creep-Fatigue Studies on HTGR Materials" in "Component and Systems Development Programs, Quarterly Progress Report for the Period Ending March 31, 1976," GA-A13898, April 1976.
4. S. S. Manson, "Fatigue: A complex Subject - Some Simple Approximations," Experimental Mechanics 5, 193 (1965).
5. In-Service Monitoring of the Strength of HTGR Core Support Structure, W. C. Morgan and F. L. Becker, BNWL-B-359, June 1974.

6. Task Area VI - Safety Instrumentation and Control Systems

6.1 Monitoring for the Impurities in the Primary Coolant  
at Fort St. Vrain (S. Nicolosi)

The mass spectrometer which is to be used for the on-line sampling of the Fort St. Vrain primary coolant is still under construction by the Nuclide Corporation in State College, Pennsylvania.

7. Task Area VII - Accident Delineation (C. Sastre)

Work has continued in the review of the Accident Initiation and Progression Analysis effort at General Atomic. The need for consideration of activation products along with the fission products in the estimation of consequences has been identified. The possibility of formation of aerosols has been identified as a conceivable mechanism that could, in the postulated event of a core heatup, have an impact on the realistic estimates of PCRV release fractions which are now made on the basis of vapor condensation consideration.

## 8. Task Area VIII - Phenomena Modeling and Systems Analysis

### 8.1 HTGR Safety Code Library (J. Beerman, J. Colman)

The TAP<sup>1</sup> computer code (1975 version), obtained from General Atomic Corporation (GA), has been converted to run successfully on the CDC 7600. A considerable further amount of work is required to fully understand the code and assess the outputs obtained from it.

The Mossbauer Data Analysis code, MOSBDA<sup>2</sup>, has been added to the HTGR Library. Extensions have been made to the code in order that automatic punched paper tape output could be utilized indirectly to search for the approximate location of peaks and to supply this information to the Least Squares Lorentzian fitting routines.

The ORIGEN<sup>3</sup> computer code was received from the Radiation Shielding Information Center (RSIC) and was made operational on the CDC 7600. Several errors in the version received were eliminated and the overlay structure of the program was redesigned in order to satisfy the more severe central memory constraints of the CDC 7600, and also to make execution of the code more efficient. The Program, as received, had been syntactically converted from IBM-360 Fortran IV to CDC Fortran but the conversion had never been tested.

The INREM<sup>4</sup> and EXREM<sup>5</sup> computer codes have been received from RSIC and are undergoing conversion to the CDC 7600 computer. These codes calculate internal and external radiation doses from beta, positron, electron and gamma radiation.

The BNL-developed code, HAZARD<sup>6</sup>, is operational and has been added to the HTGR Library. This code analyzes layering and

and flammability of gases in an HTGR containment vessel following a depressurization accident. It is described more fully elsewhere in this report.

Table 8-1 summarizes the status of the 45 programs now being maintained in the HTGR Safety Code Library.

8.2 A Simplified Inventory of Radioactive Nuclides for Use In HTGR Calculations (M. Dickey)

Several hundred radioactive nuclides are produced as by-products in a nuclear reactor, obviously not all of these can be considered in detail, so it is useful to construct a small subset of the more important nuclides from which the ones which should be subjected to further study can be selected. For example, when considering an accident which results in the release of fission products from a reactor, we need not consider any short lived isotopes themselves with half-lives less than a few hours, since all of these will have decayed to a negligible fraction of their original potency, during the time taken for the fission products to escape after a reactor scram, excepting any nuclides that are produced by the decay of a long-lived parent. The hazard posed by a particular nuclide will depend on how it has been dispersed as well as the time at which exposure to the nuclide occurs.

Several factors should be taken into consideration when evaluating the relative importance of the various radioactive nuclides. The inventory in the reactor depends on the operating history. The

Table 8-1

HTGR Safety Code Library

<u>Program</u>	<u>Status</u>	<u>Proprietary</u>	<u>Function</u>
CRECT	OP	NP	Corrects data on ENDF/B tape.
LISTFC	OP	NP	Lists data from ENDF/B tape.
RIGEL	OP	NP	Manipulates data on ENDF/B tape.
ENDFB2	OP	NP	Converts data on ENDF/B tape to binary.
FLANGE	OP	NP	Prepares thermal cross section transfer arrays.
GAND2	OP	NP	Prepares fine group fast, resonance, and thermal cross sections from ENDFB2 binary tapes.
GFE2	OP	NP	Prepares fine group fast cross sections from ENDFB2 binary tapes.
MAKE	OP	NP	Prepares fine group fast cross section tape from GFE2 for spectrum codes.
WTFG	OP	NP	Prepares fine group thermal cross section tape from GAND2 or FLANGE for spectrum codes.
PRINT	OP	NP	Reads the fast cross section tape produced by MAKE.
SPRINT	OP	NP	Reads the thermal cross section tape produced by WTFG.
GGC4	OP	NP	Prepares broad group cross sections from MAKE and WTFG tapes.

C = In the process of being converted to the CDC-7600.  
OP = Operational on the BNL CDC-7600 system under Scope 2.  
R = Recently received from General Atomic Co. or Argonne Code Center.  
P = General Atomic Company proprietary code.  
NP = Not considered to be a proprietary code.



Table 8-1 Cont'd.

<u>Program</u>	<u>Status</u>	<u>Proprietary</u>	<u>Function</u>
INTERP	OP	NP	Prepares broad group cross sections from MICROX output data tapes.
1-DX	OP	NP	Performs one-dimensional, diffusion theory, steady-state calculations.
FEVER-7	OP	NP	Performs one-dimensional, diffusion theory, burnup and reload calculations.
TEMCO-7	OP	NP	Computes reactor temperature coefficients from input cross section data.
BLOOST-7	OP	NP	Performs zero-dimensional reactor kinetics calculations.
GAKIT	OP	NP	Performs one-dimensional reactor kinetics calculations.
TWIGL	OP	NP	Performs two-dimensional light-water reactor kinetics calculations.
TAC-2D	OP	NP	Performs two-dimensional, transient conduction analyses.
FLAC	OP	NP	Calculates steady-state flow distributions in arbitrary networks with heat addition.
POKE	OP	P	Calculates steady-state flow distribution and fuel and coolant temperatures in a gas-cooled reactor.
RECA	C	P	Calculates time-dependent flow distribution and fuel and coolant temperatures in the primary system.
CORCON	OP	P	Computes the temperature history and fission product redistribution following a loss of all convective cooling of the core.
SORS	OP	P	Computes the release of volatile fission products from an HTGR core during thermal transients.
GOPTWO	OP	NP	Analyzes the steady-state graphite burnoff and the primary circuit levels of impurities.
OXIDE-3	OP	P	Analyzes the transient response of the HTGR fuel and moderator to an oxidizing environment.

Table 8-1 Cont'd.

<u>Program</u>	<u>Status</u>	<u>Proprietary</u>	<u>Function</u>
SAMPLE	OP	NP	Propagates uncertainties in probability distributions by Monte Carlo technique.
TAP	OP	P	Calculates the transient behavior of the integrated HTGR power plant.
SORSG	OP	P	Computes the release of non-volatile gaseous fission products from an HTGR core during thermal transients.
DIFFTA	OP	NP	Solves the steady-state, two-dimensional diffusion equation by finite element method.
DIFFT1	OP	NP	Solves the time-dependent, 2-D diffusion equation by the finite element method.
PDQ-7	OP	NP	Analyzes reactors in up to three space dimensions via diffusion theory.
SOSNGC	OP	NP	Calculation of steady state natural convection flow rates during long-term loss of power.
HILDA	OP	NP	Analyzes data acquired from the Helium Impurities Loop.
OSCIL	OP	NP	One-dimensional spring-mass system simulator for seismic analysis of HTGR core.
H-CON1	OP	NP	One-dimensional heat conduction code for an HTGR fuel pin by finite difference method.
HYDRA-1	OP	NP	Computes thermal/hydraulic parameters for single phase liquid due to external heat source.
CONTEMPT-G	OP	P	Simulation of temperature-pressure response of an HTGR containment atmosphere to postulated coolant circuit depressurization.
SOSSME	OP	NP	Solves the steady state one-dimensional momentum equation.

amounts of fission and activation products in the core are highest just prior to refueling so, to be conservative, the initial inventory at the time of the accident, is taken to be that at the end of a fuel cycle. After the accident the amount of each nuclide changes in the course of time and because of the differences in half lives the relative order of importance of the isotopes changes. Thus it is necessary to list a different set of important nuclides depending on the time at which the effects of the nuclides are to be considered. The fraction of the total amount of each radioactive nuclide in the reactor which is released to the environment, will depend on the particular accident involved. The subsequent dispersal of the radioactive products may differ because of the different physical and chemical properties of the individual nuclides. If the dispersal mode involves individual properties, such as diffusion constants, then the release fraction may vary widely, but if the dispersal mode involves some inert carrier less differences may be expected. If transport depends on molecular motion then the more volatile elements will be more widely dispersed, however if dispersal results from an explosion or if an aerosol is formed, even non volatile elements will be carried far from the reactor. The pathways leading to exposure become very complex as the time, which has elapsed since the initial release, increases. We cannot consider here all the myriad possibilities of dispersal so we will rank the nuclides in terms of their activity and biological importance for relatively short times only.

The activity in curies does not in itself measure the danger to the public. The effects of radiation will depend on the type of exposure, so to take account of the biological effects we have here used data made available with the INREM<sup>7</sup> code. This code was developed to calculate the internal doses resulting from inhalation or ingestion of radioactive isotopes. The data base includes 259 nuclides but not all of the isotopes generated in an HTGR, so some nuclides had to be omitted from the calculation of the doses. The dose rate factors used by INREM<sup>7</sup> are those recommended by the International Committee on Radiological Protection<sup>8</sup> and partially account for the effects of the descendants of a given nuclide. The dose commitment calculated in INREM<sup>7</sup> represents the total commitment for 50 years resulting from a delta function intake by an individual of age 21 years.

The potential hazards, arising from the nuclides at different times, are shown in Table 8-2 and Figure 8-1. For a particular accident, these figures should be multiplied by an appropriate factor which takes into account the details of the dispersal. Table 8-2 shows the 40 most important nuclides ranked in descending order at times of one day and one week after a reactor scram. The initial inventory in the reactor was taken to be that calculated by General Atomic<sup>9</sup> assuming normal operating conditions and that the accident occurs towards the end of a fuel cycle. Table 8-2a shows the activity in curies. Of the half-life of a daughter nuclide is much shorter than

TABLE 8-2a

ACTIVITY IN CURIES			
	1 DAY		1 WEEK
PA233	1.57E+09	PA233	1.35E+09
XE133	1.75E+08	NB95	1.71E+08
NB95	1.72E+08	ZR95	1.60E+08
ZR95	1.70E+08	Y91	1.42E+08
LA140	1.67E+08	SR89	1.39E+08
BA140	1.60E+08	CE141	1.37E+08
PR143	1.57E+08	LA140	1.32E+08
CE141	1.56E+08	PR143	1.24E+08
Y91	1.52E+08	BA140	1.16E+08
SR89	1.51E+08	PR144	1.05E+08
M099	1.28E+08	CE144	1.05E+08
TC99M	1.22E+08	XE133	8.75E+07
PR144	1.07E+08	RU103	7.36E+07
CE144	1.07E+08	RH103M	7.33E+07
I132	9.82E+07	I131	5.20E+07
CE143	9.69E+07	U237	4.61E+07
TE132	9.53E+07	ND147	3.91E+07
U237	8.54E+07	M099	2.91E+07
I131	8.47E+07	TC99M	2.78E+07
I133	8.40E+07	I132	2.72E+07
RU103	8.17E+07	TE132	2.64E+07
RH103M	8.14E+07	PM147	1.87E+07
NB97	6.44E+07	CS134	1.49E+07
ZR97	5.97E+07	Y90	8.09E+06
NB97M	5.74E+07	SR90	8.09E+06
ND147	5.69E+07	CS137	7.83E+06
NP238	4.21E+07	CS136	7.37E+06
XE135	4.03E+07	RH106	7.20E+06
Y93	3.75E+07	RU106	7.20E+06
SR91	2.75E+07	BA137M	7.20E+06
PM149	2.13E+07	TE129	6.87E+06
NP239	2.13E+07	TE129M	6.86E+06
PM147	1.85E+07	TE127	6.22E+06
Y91M	1.81E+07	NP238	5.92E+06
RH105	1.58E+07	CE143	4.71E+06
CS134	1.50E+07	SB127	4.25E+06
I135	1.41E+07	NP239	3.63E+06
TE127	1.39E+07	PM148	3.35E+06
TE131M	1.36E+07	PM149	3.26E+06
SB127	1.32E+07	NB95M	3.00E+06





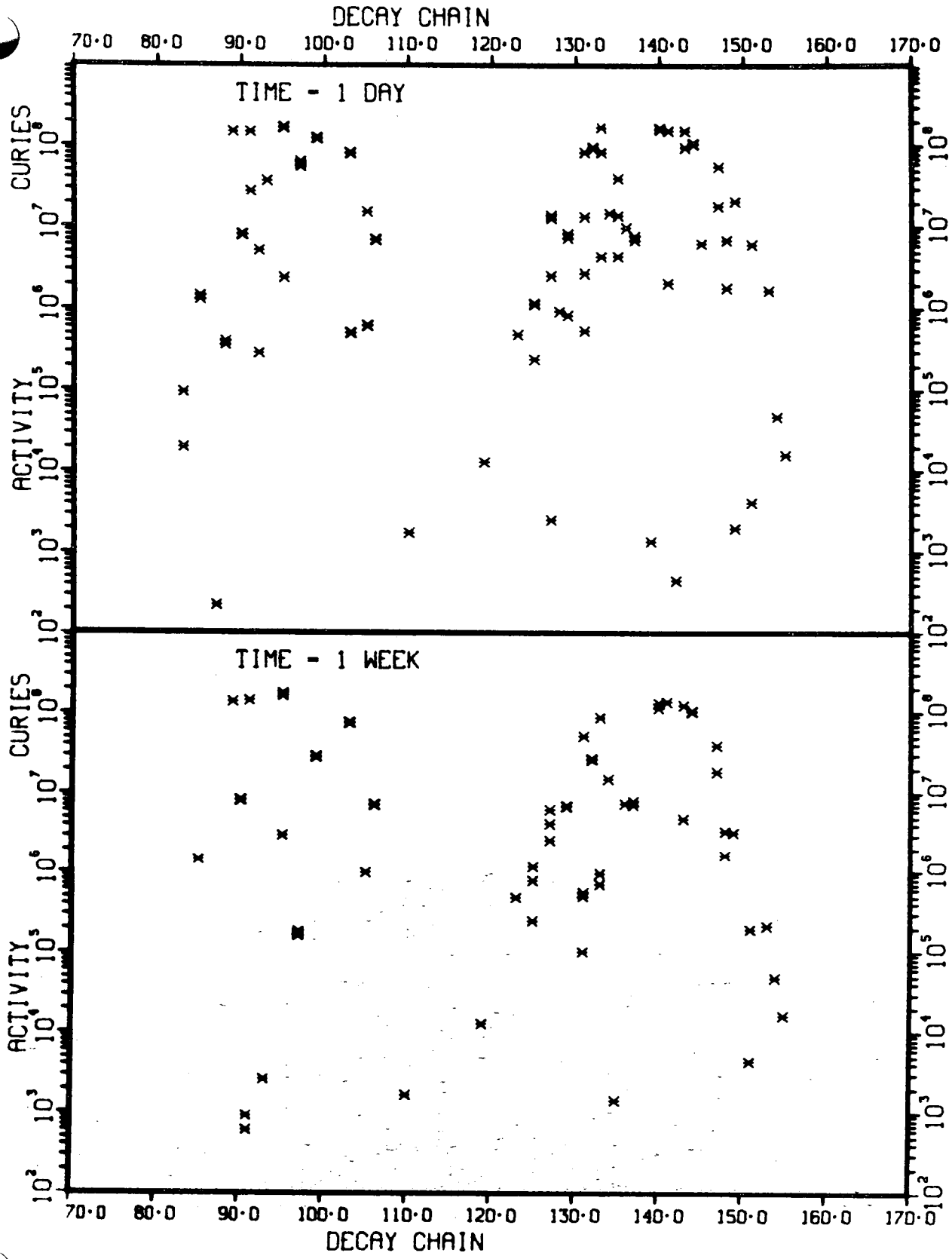


Figure 8-1a.





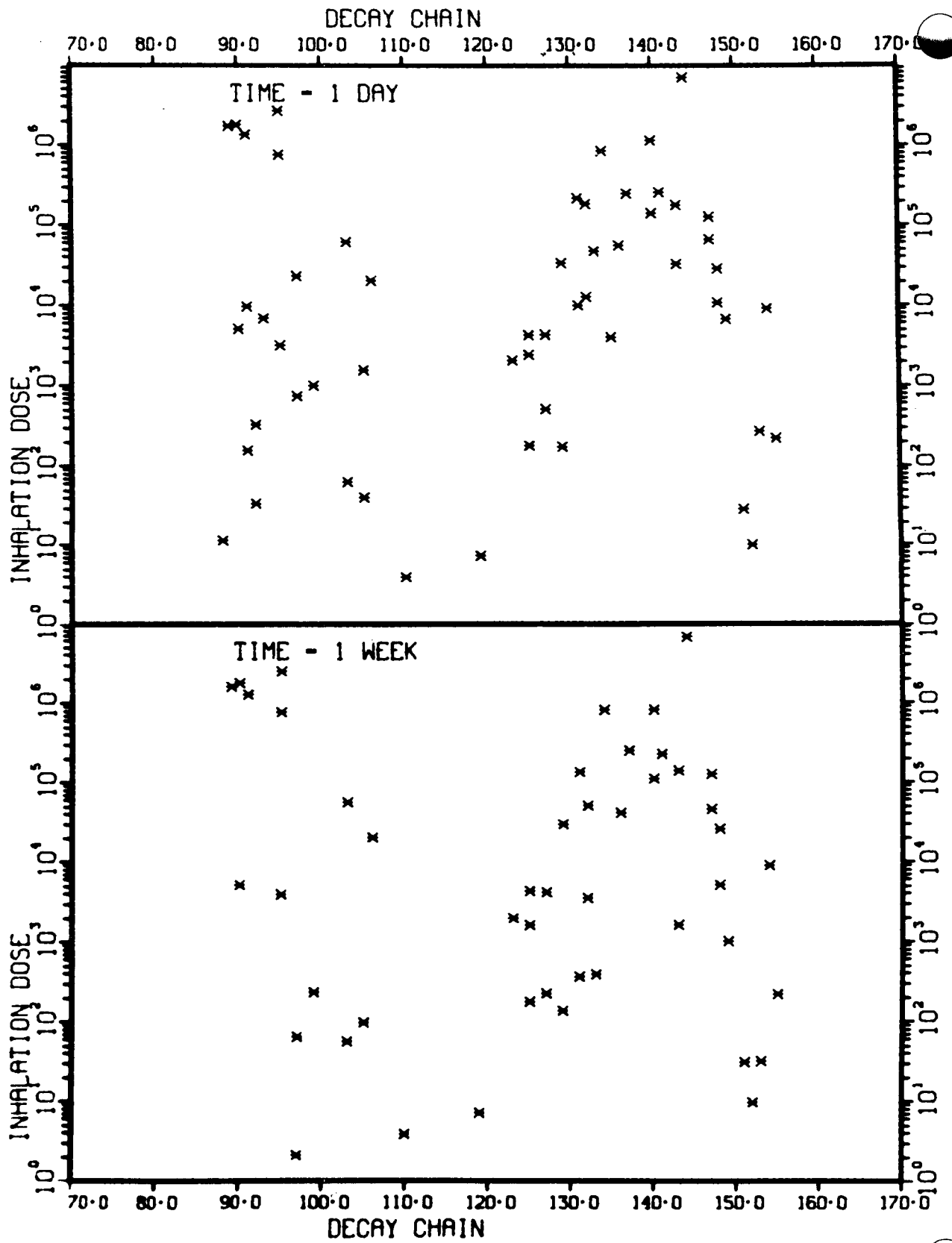


Figure 8-1b.

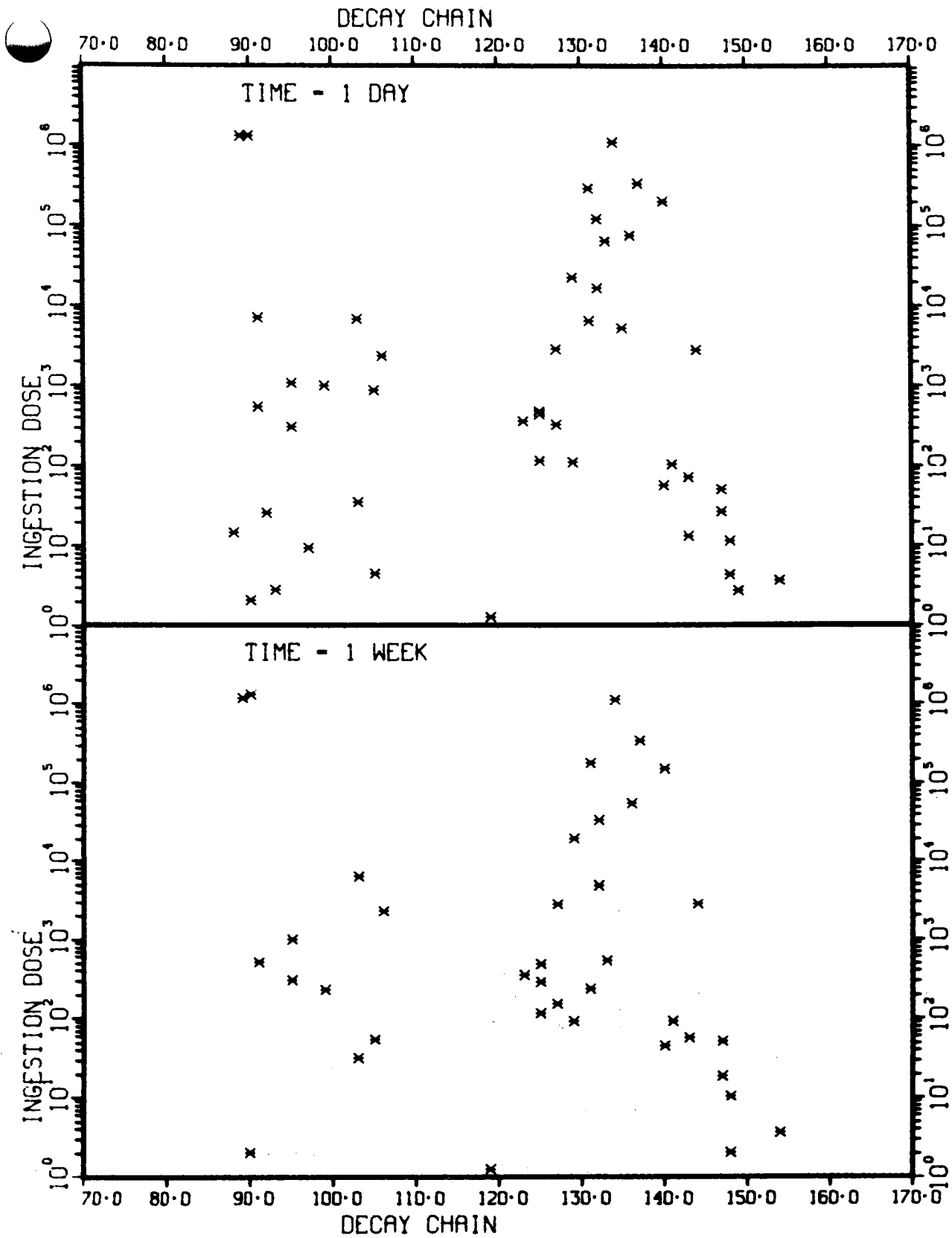


Figure 8-1c.

that of its parent then, after a while, a state of secular equilibrium is reached and the activities of the two are the same. Several such pairs occur in the list; e.g.  $^{90}\text{Y}$ - $^{90}\text{Sr}$ . In Table 8-2b and 8-2c the biological impact of the nuclides is taken into account by multiplying the activity by the whole body does commitment factors given in INREM.<sup>7</sup> Table 8-2b shows the relative hazard in arbitrary units if the exposure results from inhalation and Table 8-2c if the exposure results from ingestion. Figure 8-1 shows the results for all the fission product decay chains, at times of one day and one week, after the reactor scram. In Figure 8-1a the activity is plotted versus the atomic number of the nuclide. The activity of each member of a decay chain is plotted separately, for all nuclides with a significant activity, not the sum of all the activities in each chain. For a long lived parent- short lived daughter pair, the two points coincide. Figures 8-1b and 8-1c are similar plots and show the potential hazard due to inhalation or ingestion.

### 8.3 Combustion Hazard Analysis (I. Omata, H. Takahashi)

The reactor containment building of an HTGR is designed so that it keeps its integrity in the design basis depressurization accident, that is a rapid depressurization of the primary coolant system following the failure of a PCRV penetration closure. The CONTEMPT-G code of General Atomic Company analyzes pressure and temperature transient response with an assumption that the jet gas injected into the containment

building is homogeneously mixed with air. This instant homogenization model is not an appropriate model for the analysis of the flammability of the mixed gas.

It was conjectured by Strehlow,<sup>10</sup> (University of Illinois) that the light helium gas injected into the containment building will be layered in the upper part of the building. He developed the code named HTGRF4 and analyzed the helium gas injection from a ruptured closure with 100 in.<sup>2</sup> area.

In order to discuss the possibility and effects of combustion hazards, an analysis was initiated concerning the flammability of the gas mixture of helium, hydrogen and carbon monoxide injected into the containment building from various sizes of the penetrations. For this analysis, we extended his model and constructed the code named HAZARD<sup>11</sup>.

Figures 8-2 and 8-3 show the schematic models of this calculation and the approximate structure of underexpanded jet. These systematic studies were carried out for the cases of various rupture areas, and various concentrations of hydrogen and carbon monoxide in He gas.

Figure 8-4 indicates the variation of He mole fraction inside of the containment building in the case of a 100 in.<sup>2</sup> rupture area, where  $t$  is the time (in seconds) after the rupture occurs. Figure 8-5 shows the case of a 10 in.<sup>2</sup> rupture area. From these calculational results, we can evaluate whether or not the gas mixture in the containment building is flammable.

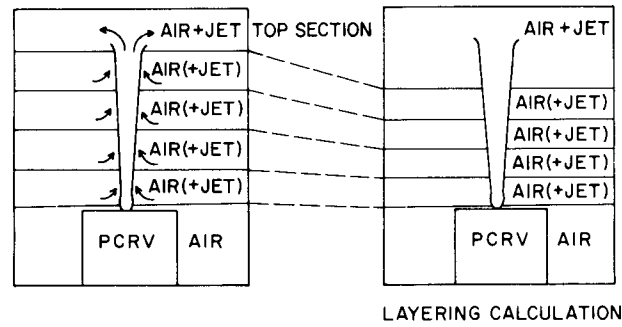
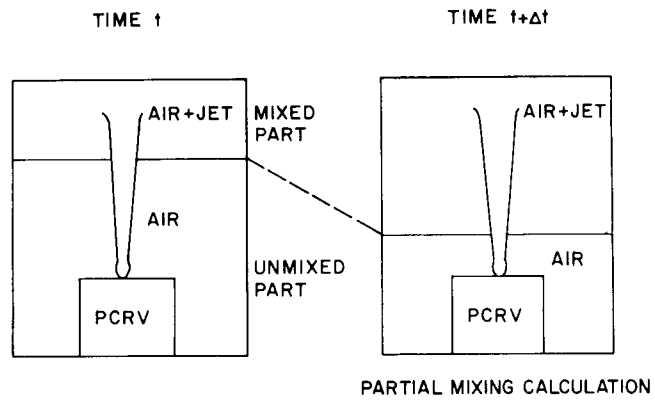


Figure 8-2. Figure 1 schematic model of calculation.

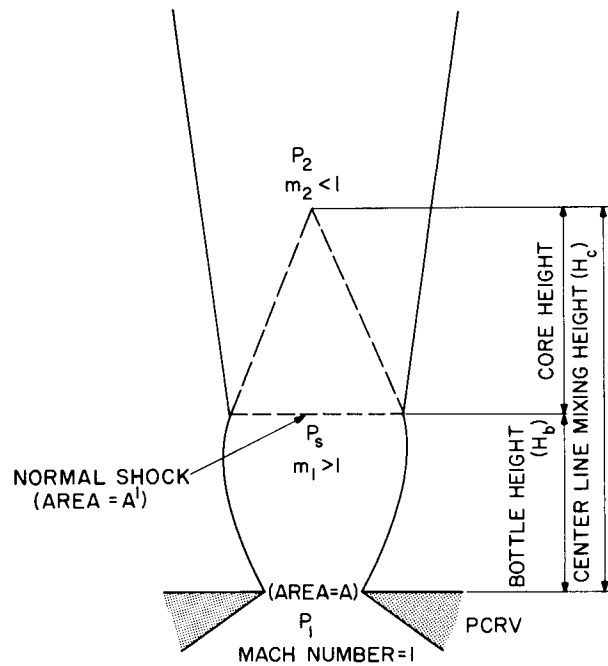


Figure 8-3. Figure 2 approximate structure of underexpanded jet.

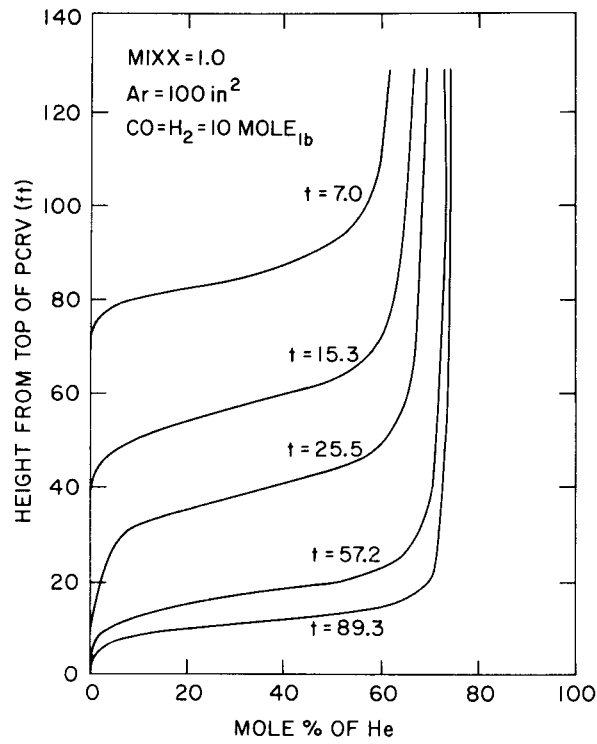


Figure 8-4. Variation of He mole fraction with 100in<sup>2</sup> rupture.

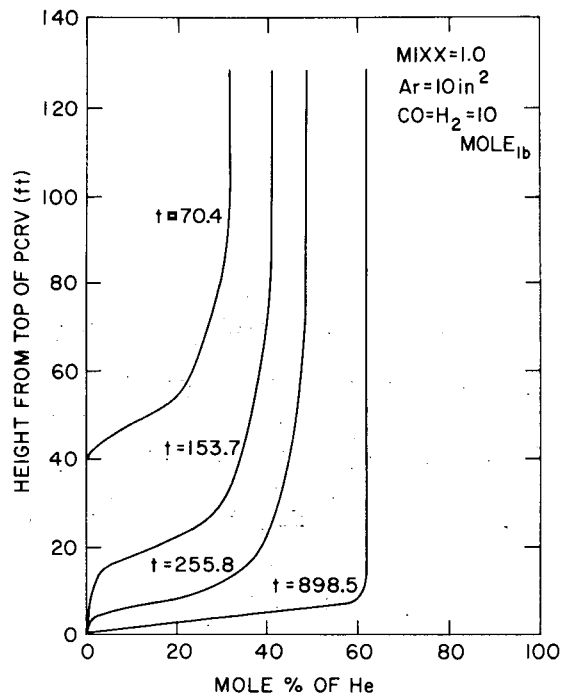


Figure 8-5. Variation of He mole fraction with 10in<sup>2</sup> rupture.

Figure 8-6 shows the potential energy released by combustion of the flammable gas in the building. The abscissa indicates the mole<sub>lb</sub> of H<sub>2</sub> and CO gas, combustion does not occur because the concentration of the combustible gas is outside of the flammable range. Beyond the 210 mole<sub>lb</sub>, a large amount of energy can be released as the result of the combustion of the mixed gas.

The estimate of the pressure rise due to this amount of energy release was carried out by a simple calculation<sup>12</sup>, and an estimated value of the pressure rise shows good agreement with the value obtained from the experimental formula<sup>13</sup>.

8.4     STREC-3: A Digital Computer Model to Predict Fatigue  
Lifetime of Plates Subjected to Acoustic Noise

(H. Fenech, A. Rao - University of California, Santa Barbara)

The thermal liner cover plate in the PCRV (Prestressed Concrete Reactor Vessel) of the HTGR (High Temperature Gas Cooled Reactor) is subjected to various acoustic fields of sound pressure levels (SPL) as high as 150db (ref.  $2 \times 10^{-4}$   $\mu$ bar). The cover plate is excited by the noise source in its resonance modes and the resulting high stresses in the plate may cause fatigue failures. Although this computer code is written for the above specific use, the code can also be used to study the vibratory response and fatigue failure of plates subjected to more general flow noise or any other random forcing function of known power spectrum.

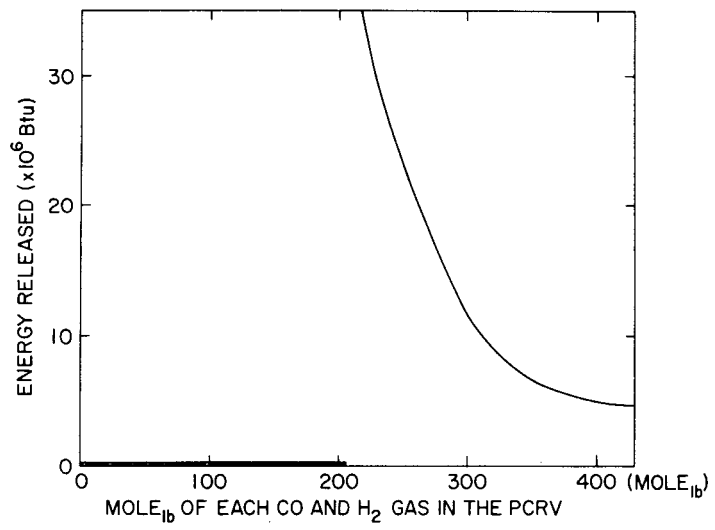


Figure 8-6. Potential release energy by combustion.



The developed computer code STREC-3 has the capability of predicting the plate fatigue lifetime when the user supplies a structural response characteristic subroutine which computes the maximum displacement and maximum stress spectra for an input noise spectrum. When the user is not providing the subroutine, the program STREC-3 calculates the displacement and stress spectra using the theory outlined in Ref. 14. This theory is valid for a simply supported plate subjected to a diffusive noise source. The subroutine PLATE 1 is based on this theory. A separate subroutine, PLATE 2, which calculates the displacement and stress response spectra by solving numerically the plate displacement equation, is under development. The present version of the STREC program does not include in the plate displacement equation the effect of the radiative pressure which can be neglected in most cases. This effect will be incorporated in a later version.

Three different models can be optionally used to predict the fatigue lifetime. These are, the narrow band model (NBM); octave band model (OBM); and quasistationary model (QSM). The QSM is an extension of the method used in Ref. 14. The user may choose any or all of these models. The output of the program includes, in addition to the lifetime, the input pressure spectrum the displacement spectrum and the stress spectrum. The variance of the stress spectrum at 1/50 of each of the octave bands is also printed.

STREC-3 is written in FORTRAN-IV in double precision algorithm and has the following characteristics and capabilities (see Fig. 8-7).

A. Characteristics:

1. The main program reads the input noise spectrum and various octave frequencies. The subroutine PLATE 1 (or PLATE 2) is called to calculate the maximum displacement and stress response spectra. The subroutine OCTMOD will calculate the mean square variance at 1/50 of each octave band's using Aitkin's interpolation formula and Simpson's rule.
2. The subroutine OCTMOD calls the subroutine NBM, which predicts the fatigue lifetime on the basis of narrow band model; or the subroutine OBM which predicts the lifetime on the basis of octave band model; or the subroutine QSM which predicts the lifetime on the basis of the extension of the theory given in Ref. 14. The frequency and the mean square stress in each of the octave bands is printed in the subroutine OBM.

B. Capabilities:

1. The subroutine PLATE 1 (PLATE2) and OCTMOD will be called back if the damping ratios are changed and continues the operations until MN is set to zero.
2. When MN=0, the program goes back and reads the next noise source. If the noise source is not available or a blank is encountered the

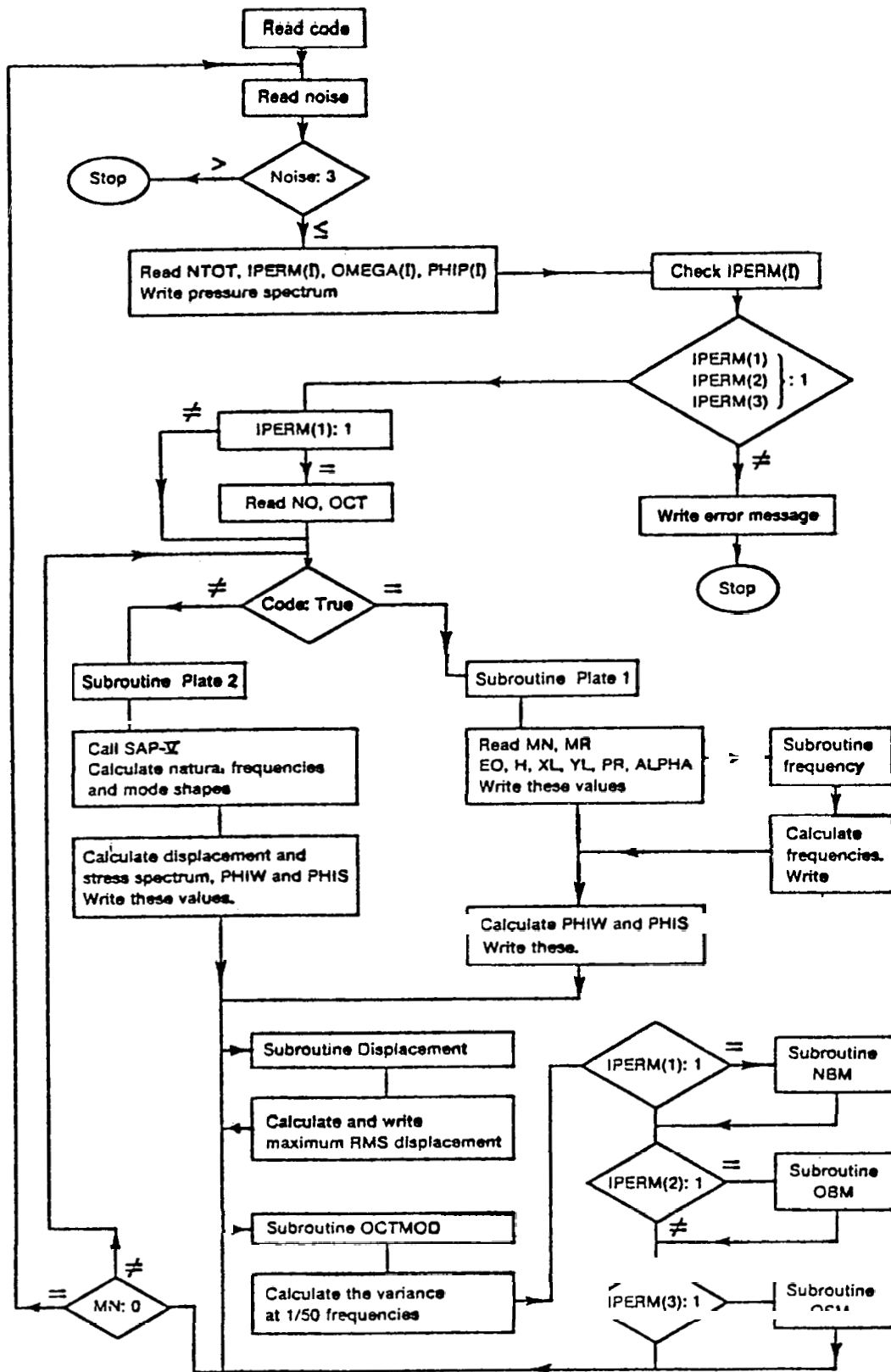


Figure 8-7. Flow diagram for STREC-3 computer code.

program stops. Otherwise, the program will repeat the calculations by calling the subroutines PLATE 1 (or PLATE 2) and OCTMOD.

3. The user may supply the displacement and stress response spectrum of the structure under study in the subroutine PLATE 2.

Irrespective of the geometric nature of the structure or its boundary conditions, the code STREC-3 evaluates the fatigue lifetime of that structure.

## References

1. A. Bardia and R. C. Potter, "TAP: A Program for Analysis of HTGR Nuclear Steam Supply System Performance Transients," General Atomic Report GA-A-12348 (GA-LTR-21), January 30, 1976.
2. J. Colman, "Mossbauer Data Analysis Code," Brookhaven National Laboratory internal memorandum (to be published).
3. M. J. Bell, "ORIGEN, the ORNL Isotope Depletion and Regeneration Code," ORNL-4628, May 1973.
4. G. G. Killough, P. S. Rohwer, and W. D. Turner, "INREM - A FORTRAN Code Which Implements ICRP2 Models of Internal Radiation Dose to Man," ORNL-5003, February 1975.
5. D. K. Trubey and S. V. Kay, "The EXREM III Computer Code for Estimating External Radiation Doses to Populations from Environmental Releases," ORNL-4332, December 1973.
6. I. Omata, "An Analysis of Gas Layering and Flammability in The Containment Vessel Following Depressurization of an HTGR," BNL Internal Report (to be published 1976).
7. G. G. Killough, P. S. Ronhwer and W. D. Tumer, INTEM-A Fostran Code Which Implements ICRP2 Models of Internal Radiation Dose to Man, ORNL-5003 (1975).
8. International Commission on Radiological Protection. Recommendations of the International Commission on Radiological Protection, ICRP Publication 2, Perganion Press, London 1959.

## References

9. Fulton Generating Station, Preliminary Safety Analysis Report (1974), General Atomic Standard Safety Analysis Report-6 (1974); General Atomic.
10. R. A. Strehlow, "HTGR Safety, Combustion Consequences of Rapid Depressurization Due to an Upper Penetration of the PCRV, Private Communication, May 1976.
11. I. Omata, "An Analysis of Gas Layering and Flammability in the Containment Vessel Following Depressurization of an HTGR", Draft, 1976.
12. I. Omata, "Considerations on Pressure Rise by Combustion in a Containment Building", Memorandum to H. Takahashi, October, 1976.
13. P. A. Cabbage and M. R. Marshal, "Pressure Generated in Combustion Chambers by the Ignition of Air-Gas Mixtures", I. Chemical Engineering Symposium Series No. 33 (Instrm, Chem. Engrs., London, 1972.
14. H. Fenech, "An Analysis of Acoustic Flow Noise in Closed Systems and the Fatigue Lifetime of Structure Boundaries", Nuc. Eng. Des., 34, pp. 323-334 (1975).